Constant-Flux Inductor with Enclosed-Winding Geometry for Improved Energy Density

Han Cui

Thesis submitted to the Faculty of the
Virginia Polytechnic Institute and State University
in partial fulfillment of the requirements for the degree of

Master of Science
in
Electrical Engineering

Khai D. T. Ngo, Chair
Guo-Quan Lu
Qiang Li

June 28th, 2013
Blacksburg, Virginia

Keywords: constant-flux; time constant; magnetic field; uniformity factor; high-density inductor; high-density transformer; high-density magnetic; distributed core; distributed winding

Constant-flux Inductor with Enclosed-Winding Geometry for Improved Energy Density

Han Cui

Abstract

The passive components such as inductors and capacitors are bulky parts on circuit boards. Researchers in academia, government, and industry have been searching for ways to improve the magnetic energy density and reduce the package size of magnetic parts. The "constant-flux" concept discussed herein is leveraged to achieve high magnetic-energy density by distributing the magnetic flux uniformly, leading to inductor geometries with a volume significantly lower than that of conventional products. A relatively constant flux distribution is advantageous not only from the density standpoint, but also from the thermal standpoint via the reduction of hot spots, and from the reliability standpoint via the suppression of flux crowding.

For toroidal inductors, adding concentric toroidal cells of magnetic material and distributing the windings properly can successfully make the flux density distribution uniform and thus significantly improve the power density.

Compared with a conventional toroidal inductor, the constant-flux inductor introduced herein has an enclosed-winding geometry. The winding layout inside the core is configured to distribute the magnetic flux relatively uniformly throughout the magnetic volume to obtain a higher energy density and smaller package volume than those of a conventional toroidal inductor.

Techniques to shape the core and to distribute the winding turns to form a desirable field profile is described for one class of magnetic geometries with the winding enclosed by the core. For a given set of input parameters such as the inductor's footprint and thickness, permeability of the magnetic material, maximum permissible magnetic flux density for the allowed core loss, and current rating, the winding geometry can be designed and optimized to achieve the highest time constant, which is the inductance divided by resistance (L/R_{dc}).

The design procedure is delineated for the constant-flux inductor design together with an example with three winding windows, an inductance of 1.6 μH, and a resistance of 7 mΩ. The constant-flux inductor designed has the same inductance, dc resistance, and footprint area as a commercial counterpart, but half the height.

The uniformity factor α is defined to reflect the uniformity level inside the core volume. For each given magnetic material and given volume, an optimal uniformity factor exists, which has the highest time constant. The time constant varies with the footprint area, inductor thickness, relative permeability of the magnetic material, and uniformity factor. Therefore, the objective for the constant-flux inductor design is to seek the highest possible time constant, so that the constant-flux inductor gives a higher inductance or lower resistance than commercial products of the same volume. The calculated time-constant-density of the constant-flux inductor designed is 4008 s/m^3, which is more than two times larger than the 1463 s/m^3 of a commercial product.

To validate the concept of constant-flux inductor, various ways of fabrication for the core and the winding were explored in the lab, including the routing process, lasing process on the core, etching technique on copper, and screen printing with silver paste. The most successful results were obtained from the routing process on both the core and the winding. The core from

Micrometals has a relative permeability of around 22, and the winding is made of copper sheets 0.5 mm thick. The fabricated inductor prototype shows a significant improvement in energy density: at the same inductance and resistance, the volume of the constant-flux inductor is two times smaller than that of the commercial counterpart.

The constant-flux inductor shows great improvement in energy density and the shrinking of the total size of the inductor below that of the commercial products. Reducing the volume of the magnetic component is beneficial to most power. The study of the constant-flux inductor is currently focused on the dc analysis, and the ac analysis is the next step in the research.

To my Parents

Zhenduo Cui

Yajing Han

Acknowledgments

I would like to give my deepest gratitude to my advisor, Dr. Khai Ngo, for his advising, encouragement, and patience. I truly feel lucky to have him as my advisor for my graduate study, or even my life. It is his extensive knowledge, his rigorous attitude towards research, and his scientific thinking to solve problems that enlightens me as to what makes a superior researcher. Without his generous help, it wouldn't be possible for me to learn so much in such a short time, to overcome so many difficulties in my research, and to show presentable results in this thesis. I have documented every inspiring comment from him, which will become my motto for life.

I am also grateful to my co-advisor, Dr. G. Q. Lu, who shares a great amount of knowledge, suggestions, and experience with me. I appreciate his generous help and encouragement, which inspire me a great deal and raise my self-confidence. I would also like to thank Dr. Susan Luo, who gives me generous love and care and always makes me feel at home. I have learned a lot from her and got a much clearer idea on my study and the future. Sincere thanks to my other committee members, Dr. Qiang Li and Dr. Kathleen Meehan, for their valuable suggestions and comments on my work.

Special thanks to Dr. Tung W. Chan, who helped me revise the thesis carefully. He let me understand how important it is to write papers in a scientific way and correct style. I am really appreciated for his help.

I would also like to thank the great staff at CPES: Ms. Teresa Shaw, Ms. Linda Gallagher, Ms. Marianne Hawthorne, Ms. Teresa Rose, Ms Linda Long, Mr. Doug Sterk, Mr. David Gilham, and Dr. Wenli Zhang.

It has been a great pleasure to work with my talented colleages at CPES. Thanks to Dr. Mingkai Mu, Dr. Daocheng Huang, Mr. Yipeng Su, Mr. Dongbin Hou, Mr. Shuilin Tian, Dr. Jesus Calata, Mr. Di Xu, Mr. Yin Wang, Mr. Zhemin Zhang, Ms. Yiying Yao, Mr. Li Jiang, Mr. Kumar Gandharva, Mr. Mudassar Khatib, and Mr. Ming Lu; I learned a lot from their rich experience and knowledge. It is not possible to list all the names here, but thanks to all the other people who helped me during the past two years. I appreciated and enjoyed the working and learning experience.

Also, I would like to thank my best friends, a group named 82620, for bringing me so much happiness in life. I love them and treasure our friendship forever.

Last but not least, I want to give my special thanks to Mr. Lingxiao Xue, who sat there patiently and listened to my presentation rehearsal for hours, and always comes around and comforts me whenever I am down. I am more than I can be with him by my side.

*This work was supported by Texas Instruments, the National Science Foundation under Grant No. ECCS-1231965, and ARPA-E under Cooperative Agreement DE-AR0000105.

Table of Contents

List of Figures

List of Tables

NOMENCLATURE

α	Uniformity factor
AT_j	Ampere-turns in winding window j
B_{max}	Maximum flux density
B_s	Saturation flux density
E	Energy stored in core
B	Flux density
H	Magnetic field
N	Total number of winding turns
H_c	Core height, equals inductor height
H_p	Plate thickness between winding and core
H_w	Winding thickness
I_r	Current rating
L	Inductance of inductor
μ	Permeability of core material
μ_o	Vacuum permeability
n_j	Number of turns in winding window j
N_w	Number of winding windows
ρ_{cu}	Copper resistivity
R_c	Outer radius of core
R_{dc}	Dc resistance of inductor
R_{Oj}, R_{Ij}	Outer and inner radii of winding window j
P_{ohm_loss}	Dc winding loss
V	Effective volume of energy storage
τ	Time constant (L/R_{dc}) of inductor
τ_v	Time-constant-density ($L/R_{dc}V$) of inductor

Chapter 1 Introduction

Power transformers and power inductors are important components of every switching converter. During the turn-on switching period, the passive components store the energy in the form of magnetic flux, and during the turn-off switching period they transfer the stored energy to the load side [1]. Because of the high-frequency ac ripple on the current through the power inductor, some of the power cannot ideally be transferred to the load and is dissipated in the core, resulting in heat and sometimes noise [2]. The core loss consists of hysteresis loss and eddy current loss, and higher operation frequency usually results in higher core loss [3]. Therefore, the core of the magnetic components cannot saturate or heat up and should be capable of providing the required inductance for an efficient performance under a given current rating. Another source of loss on the power inductor is the winding loss. The power loss on the resistance of the conductor would heat up the winding as well as the magnetic core. Furthermore, researchers in academia, government, and industry have been searching for ways to increase the magnetic energy density and reduce the package size of magnetic parts [4]-[14] because the magnetic components usually take up a large volume on the board. Therefore, for a successful design of inductors, it is necessary to obtain the required inductance, avoid saturation, obtain an acceptably low dc winding resistance and copper loss, and keep the inductor in as low a profile as possible to keep the required inductance.

1.1 Conventional Magnetic Structures

When the current flows through an inductor, the energy is stored in the magnetic core in the form of magnetic flux, which is given by

$$E = \int \frac{1}{2} B \cdot H \cdot dv \tag{1.1}$$

$$B = \mu H \tag{1.2}$$

Thus, for a given volume, uniform flux distribution in the core implies uniform energy distribution and improved space utilization. The magnetic core can be used to store the maximum amount of energy while the saturation is avoided.

However, in conventional magnetic cores, the distribution of flux is not uniform [11]. Figure 1.1 shows two common inductors with conventional structures. Based on the positions of the core and the winding, the conventional inductors can be divided into two types: enclosed-core, as shown in Figure 1.1(a), and enclosed-winding, as shown in Figure 1.1(b). Both types have a large space that is not being utilized to store energy; therefore, the energy density in these inductors is relatively low.

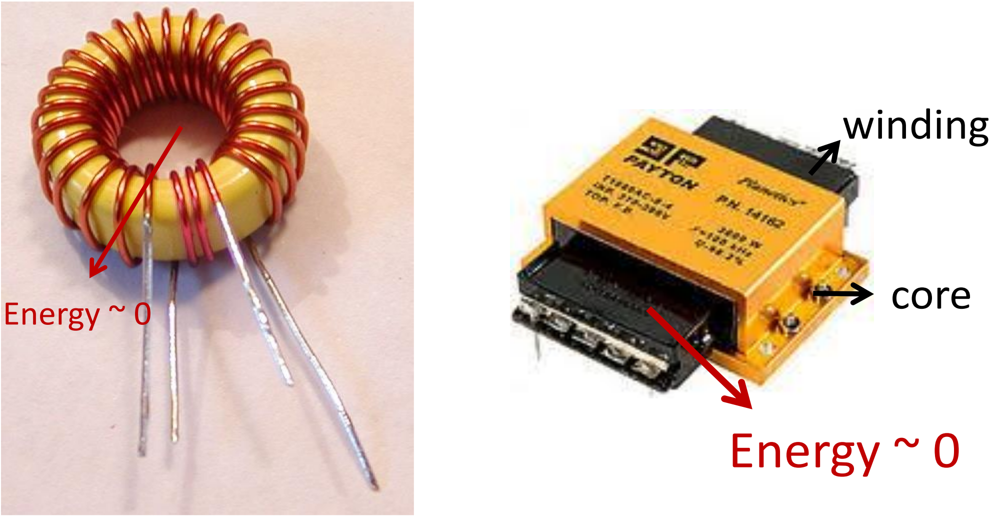

(a) **(b)**

Figure 1.1. Commercial inductors with large volume of zero energy: (a) enclosed-core structure; (b) enclosed–winding structure.

Even though the inductor is encapsulated completely instead of leaving a vacant space as shown in Figure 1.1(b), the magnetic core is not necessarily fully utilized. Figure 1.2(a) shows a commercial inductor from Maglayers [12] with 2.2 μH in a volume of 10 mm × 10 mm × 4 mm. The interior of this inductor was examined by cross-sectioning so that the solid model could be constructed for finite-element analysis of the flux distribution throughout the core volume. After sweeping the permeability of the magnetic core, finite-element simulation suggested that the core material ought to have relative permeability of 35 to achieve the rated inductance. Figure 1.2(b) is an axisymmetric view of the flux distribution on a cross-section of the core and the winding. As can be seen in the figure, the core is filled with large volume of blue color, which suggests that the flux density is very low, and the core is not fully utilized to store energy. Thus, there is a demand for uniform distribution of magnetic field and energy in the core without crowding the flux.

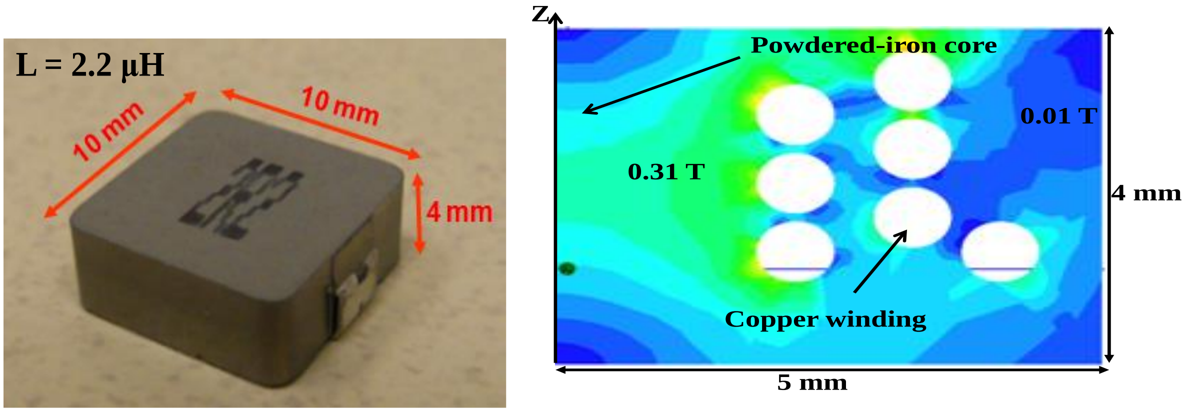

(a) (b)

Figure 1.2. (a) Completely encapsulated inductor with 2.2 μH inductance, 7 mΩ resistance, and 10 A current rating in 10 mm × 10 mm × 4 mm volume [12]; (b) axisymmetric view of the commercial inductor showing unevenly distributed flux density inside the core with 10 A current excitation and $\mu = 35\mu_0$.

1.2 Enclosed-Core Constant-Flux Inductor

In an effort to improve the quality of inductors, several ways have been tried to increase the magnetic energy density and reduce the package size of the magnetic parts. The matrix core, as discussed in [4], consists of multiple cores with winding connected. This structure has low profile and good heat dissipation. However, it sees non-uniform flux density among the elements. With the purpose of fully utilizing magnetic materials and obtaining low-profile inductors, the inductor structure using multiple permeabilities to achieve uniform flux density was proposed in [14]. Coupled inductor with lateral flux structure revealed in [10] proved to have higher density than that with vertical flux structure, so that the inductor size can be further reduced. Adding concentric toroidal cells and threading the windings properly in toroidal inductors increased the uniformity of the distribution of magnetic flux, significantly improving power density [16]. Figure 1.3 shows that a constant-flux inductor with an enclosed-core geometry has improved space utilization and increased energy density.

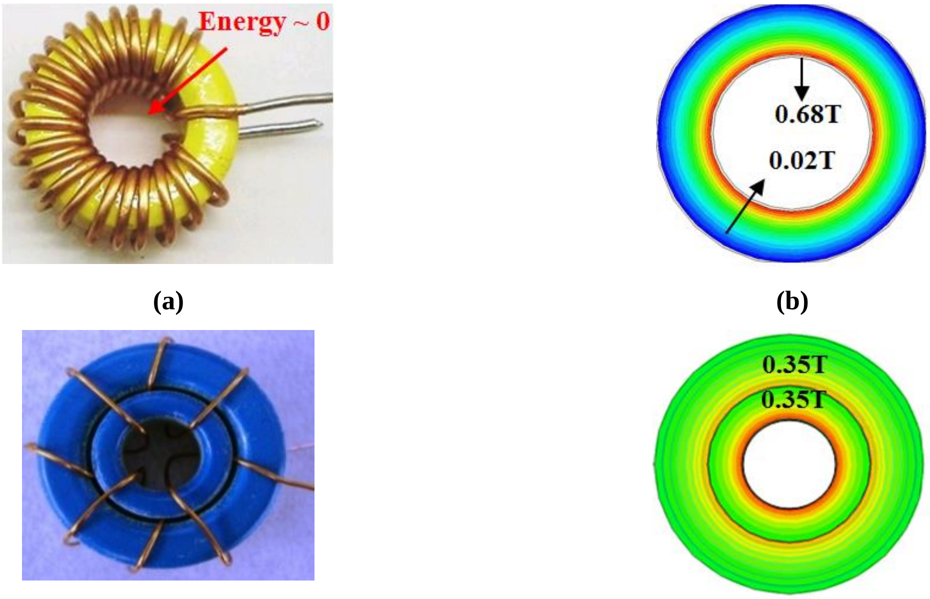

(a) **(b)**

(c) **(d)**

Figure 1.3. (a) Conventional toroidal inductor with region storing no energy; (b) unevenly distributed flux density inside a toroidal core; (c) prototype of constant-flux inductor with enclosed-core geometry; (d) more uniform flux density distribution demonstrating improved space utilization.

Compared with the inductor geometry discussed in [16], the constant-flux inductor introduced herein has an enclosed-winding geometry. The winding inside the core is configured to distribute the magnetic flux relatively uniformly throughout the magnetic volume to obtain higher energy density and smaller package volume than those of the commercial product. Simulated with the same material properties and footprint dimensions as the structure simulated in Figure 1.4(c), the inductor structure shown in Figure 1.4(b) has the same inductance, resistance, and current rating as a commercial inductor of comparable ratings (see Figure 1.4(a)), but the total height is reduced by a factor of two as a result of flux uniformity as shown in Figure 1.4(d).

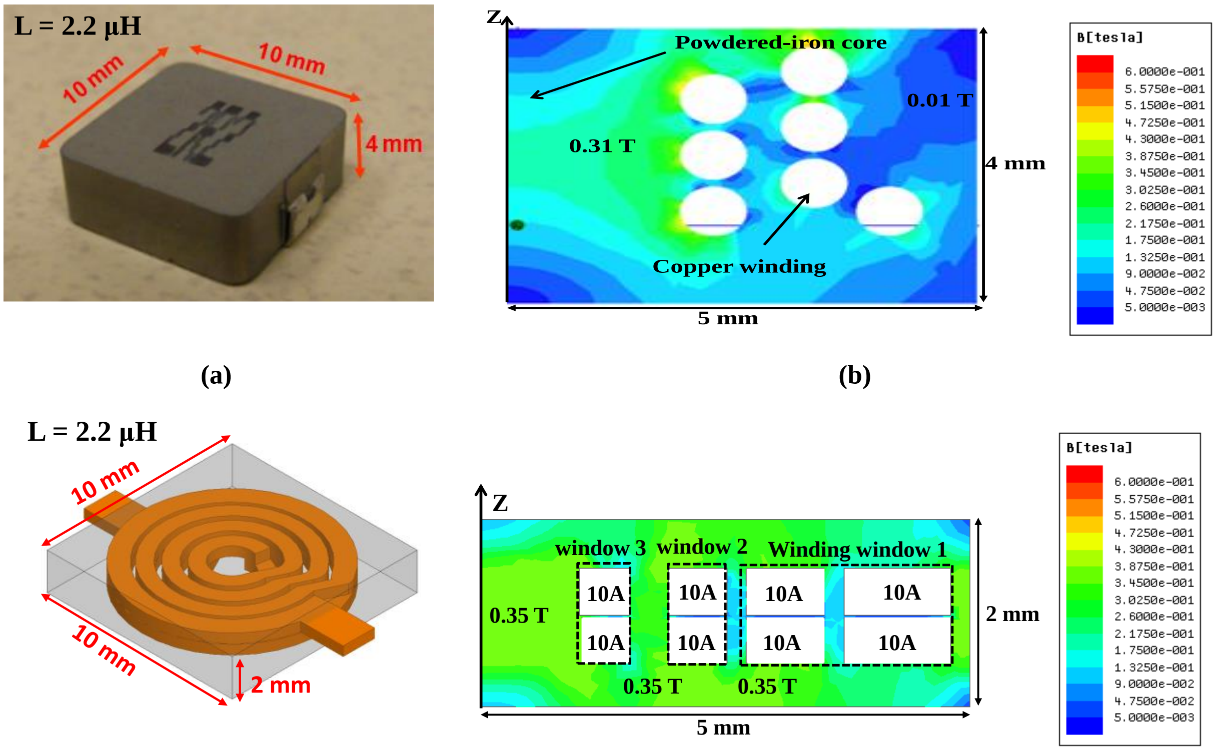

(a) (b)

(c) (d)

Figure 1.4. (a) A commercial enclosed-winding inductor with inductance of 2.2 µH, resistance of 7 mΩ, height of 4 mm, and permeability of 35 μ_0; (b) axisymmetric view of the commercial inductor showing unevenly distributed flux density inside the core; (c) 3D structure of constant-flux inductor with winding enclosed by core; total thickness is reduced by half to 2 mm, whereas inductance and resistance are kept at 2.24 µH and 5.5 mΩ with 35 μ_0 permeability; (d) relatively uniform distribution of flux density in the core of the constant-flux inductor.

1.3 Thesis Outline

The "constant-flux" concept is leveraged to achieve high magnetic-energy density, leading to inductor geometries with either footprint or height significantly smaller than that of conventional products. In the following discussion, the constant-flux inductor with enclosed-core geometry is analyzed, and an elaborate parametric study on the inductor design based on the constant-flux concept is presented.

Chapter 2 delineates the principle of constant-flux inductors with theoretical equations to shape the magnetic field distribution. Design rules are discussed and two design algorithms are introduced to design a constant-flux inductor. The design algorithms are validated by examples.

Chapter 3 gives a parametric study of several design-related parameters of the constant-flux inductor, and evaluates the effects of different parameters on the time constant and internal parameters. Comparisons of the constant-flux inductor with commercial products show great improvements in the time-constant-density.

Chapter 4 introduces different fabrication techniques for the core and the winding for constructing prototypes of the constant-flux inductor. Experimental results are also presented.

Chapter 5 gives the conclusion and proposes future work.

Chapter 2 Design Principle of Constant-Flux Inductor

2.1 Parameter Definitions in Enclosed-Winding Geometry

A constant-flux inductor (CFI) consists of a distributed winding enclosed by a core. The winding structure is configured to distribute the magnetic flux in a shaped pattern. The core is made of magnetic material such as iron powder, and determines the footprint area and the total thickness of the inductor. The winding structure usually follows a spiral pattern, surrounded by the magnetic flux generated by the current excitation. Figure 2.1 shows an axisymmetric view of a cross-section of the constant-flux inductor.

2.1.1 Winding Windows, Ampere-Turns, Footprint, and Height

As seen in Figure 2.1, an ideal constant-flux enclosed-winding inductor consists of a magnetic core with N_w winding windows. The winding windows are numbered from the outer edge ($j = 1$) to the center of the core. Each winding window carries prescribed number of ampere-turns (AT_j) to ensure uniformity of the flux distribution throughout the core volume.

The outer and inner radii of each winding window are denoted by R_{Oj} and R_{Ij}, respectively. For a given footprint diameter ($2R_c$) and total inductor/core height (H_c), the objective of constant-flux design is to optimize the radii of the winding windows, as well as the ampere-turns in each winding window, to distribute the magnetic flux as uniformly as possible.

2.1.2 Uniformity Factor α and Time Constant τ

For a given core loss density and frequency of operation, the maximum magnetic flux density B_{max} can be determined from the magnetic properties of the material [18]. The magnetic field around winding window j is allowed to drop from a maximum value B_{max} to a minimum value

αB_{max}, where $\alpha < 1$ is defined as the uniformity factor. “Constant” flux is achieved when the uniformity factor α approaches unity, implying uniform flux density everywhere throughout the core volume.

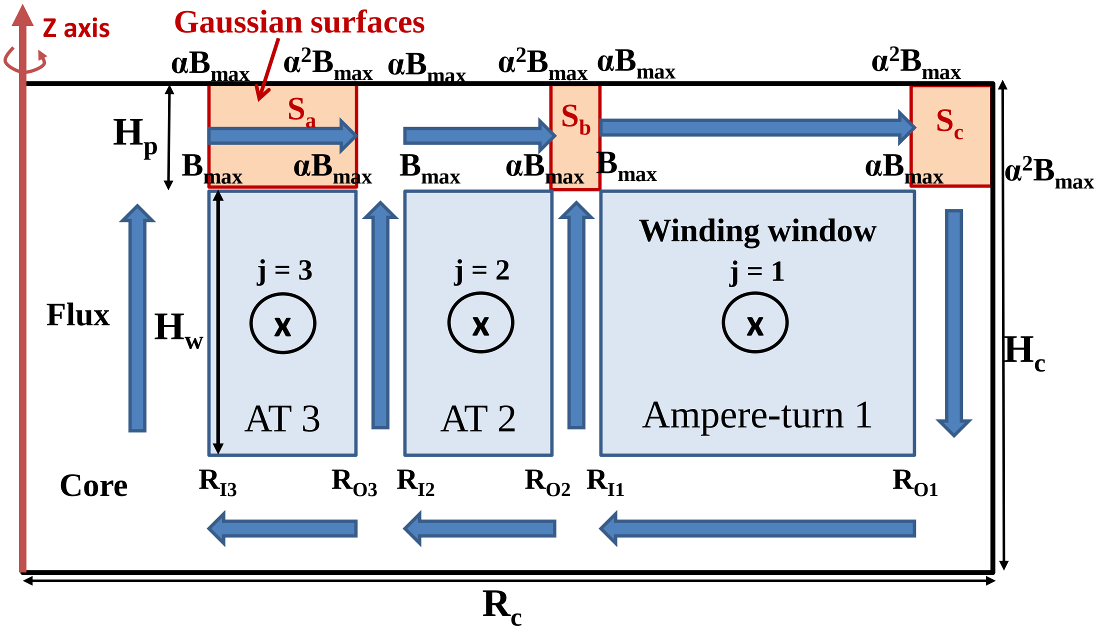

Figure 2.1. Axisymmetric view of a constant-flux enclosed-winding inductor showing three winding windows, ampere-turn direction, and magnetic flux path.

An inductor can be considered as a RL circuit, which has an ideal inductor in series with a wire resistor, as shown in Figure 2.2. The time constant of a series RL circuit is defined as the inductance divided by the resistance:

$$\tau = \frac{L}{R_{dc}} \tag{2.1}$$

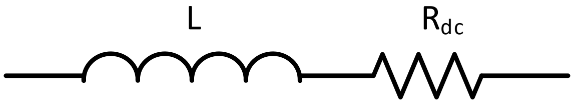

Figure 2.2. Equivalent circuit of an inductor under dc operation.

In the constant-flux inductor design, the time constant is employed to represent the ratio of the inductance to dc resistance and evaluate the performance of the inductor. At a given inductance, the dc winding resistance decreases with the increasing time constant; therefore, the dc loss decreases.

2.2 Magnetic-Field Equations

As shown in Figure 2.1, the flux density is assumed to be the maximal value B_{max} at the inner radius of each winding window, and drops by a factor of α along both the radial and vertical directions. Along the vertical edges of the winding windows, the flux density is assumed to be constant. From Gauss' law, the amount of flux that flows into a surface equals to the amount of flux that flows out of the surface. Therefore, the behavioral model of the constant-flux inductor can be derived based on the Gaussian surfaces defined on different places. In the case of winding window j = 1, the equation for S_c can be written as

$$\begin{aligned} &2\pi R_{o1} H_p \frac{(\alpha+\alpha^2)B_{\max}}{2} = \pi(R_c^2 - R_{o1}^2)\frac{(\alpha+\alpha^2)B_{\max}}{2} \\ \text{or} \qquad &R_{o1}^2 + 2R_{o1}H_p - R_c^2 = 0 \end{aligned} \tag{2.2}$$

where H_p is the plate thickness. Given H_p, the outer radius R_{o1} of winding window j = 1 is thus determined. The plate thickness H_p is related to the winding thickness H_w by

$$H_p = \frac{1}{2}(H_c - H_w) \tag{2.3}$$

For the surfaces as S_a, the flux flows from the inner radius to the outer radius of winding window j. For each winding window, the ratio of outer radius to the inner radius is related to the magnetic flux density by

$$\frac{R_{Oj}}{R_{Ij}} = \frac{B_{\max}}{\alpha B_{\max}} = \frac{1}{\alpha}\ , \ \ 1 \le j \le N_w \tag{2.4}$$

Thus, R_{I1} can be determined once R_{O1} is known, and R_{Ij} can be obtained recursively from R_{Oj} in general.

Based on the Gaussian surface S_b defined in Figure 2.1, the following equation yields recursively the outer radius of winding window $j > 1$:

$$\begin{aligned} &\frac{\alpha+\alpha^2}{2} B_{\max} 2\pi R_{O(j+1)} H_p + \frac{1+\alpha}{2} B_{\max} \pi (R_{Ij}^2 \text{ - } R_{O(j+1)}^2) = \frac{1+\alpha}{2} B_{\max} 2\pi R_{Ij} H_p \\ &\text{or} \qquad R_{O(j+1)}^2 - 2\alpha R_{O(j+1)} H_p + 2R_{Ij} H_p - R_{Ij}^2 = 0,\ \ 1 \le j \le N_w \end{aligned} \tag{2.5}$$

When H_p is not given, it can be calculated based on the Ampere's law. As shown in Figure 2.3, from the winding to the edge of the core, the flux density is regulated to drop by a factor of α vertically. Therefore, based on Ampere's law, the ampere-loop that covers the same winding window should have equal ampere-turns, and another equation can be added to solve the plate thickness between the winding and the core:

$$\begin{gathered} \int_{l_1} H \cdot dl_1 = \int_{l_2} \alpha H \cdot dl_2 \\ H_w \cdot (1+\alpha) + 2 \cdot R_{Ij} \cdot \ln(\frac{R_{Oj}}{R_{Ij}}) = \alpha \cdot (H_w + 2\,\mathrm{H}_p)(1+\alpha) + 2 \cdot \alpha \cdot R_{O2} \cdot \ln(\frac{R_c}{R_{O2}}) \end{gathered} \tag{2.6}$$

By solving (2.6) with (2.2)-(2.5) simultaneously, the plate thickness H_p and the radii of all the winding windows can be derived recursively. Note that once H_p is determined from the outermost winding window, the value remains constant for the rest winding windows for simplification. Ideally, each winding window j has a calculated H_p from (2.6), and the larger the j, the larger the H_p.

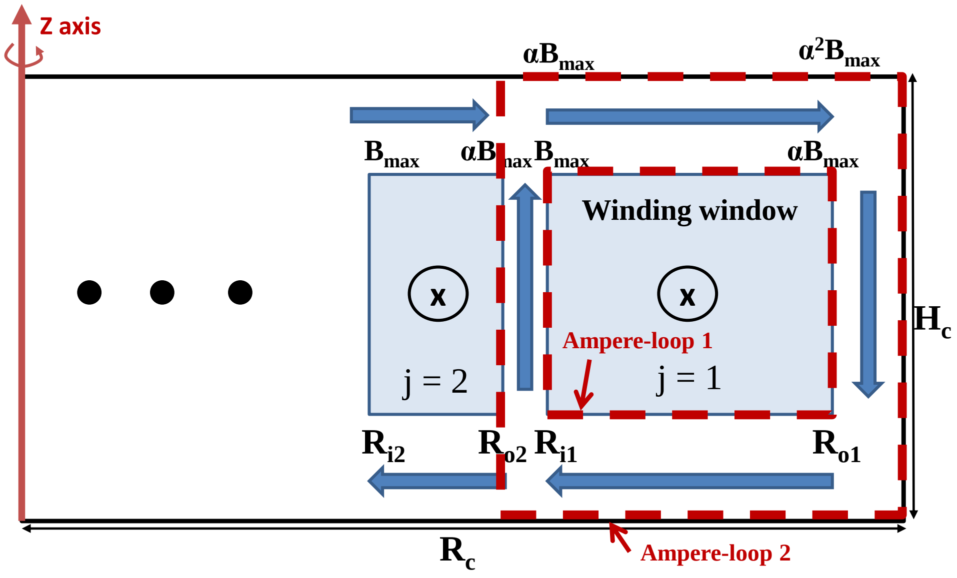

Figure 2.3. Axisymmetric view of a constant-flux inductor showing the flux drop on the vertical direction by a factor of α, ampere loops around winding window 1, and magnetic flux path.

To calculate the Ampere-turns that should be applied to winding window j, the Ampere-loop 1 in Figure 2.3 is drawn on every winding window. Based on Ampere's law, Ampere-turn AT_j is assigned to winding window j by

$$AT_j = H_w \cdot \left(\frac{B_{\max}}{\mu} \pm \frac{\alpha B_{\max}}{\mu}\right) + 2 \cdot \frac{B_{\max}}{\mu} \cdot R_{Ij} \cdot \ln\left(\frac{R_{Oj}}{R_{Ij}}\right) \tag{2.7}$$

The number of turns in winding window *j* is determined by AT_j and the rated current I_r:

$$n_j = \frac{AT_j}{I_r} \tag{2.8}$$

Therefore, the total number of turns is the sum of the number of turns in each winding window:

$$N = \sum_{j=1}^{N_w} n_j = \sum_{j=1}^{N_w} \frac{AT_j}{I_r} \tag{2.9}$$

After all the radii and plate thickness are derived, the structure of the inductor is determined. The energy stored in the constant-flux inductor can be calculated by integrating the flux density throughout the total core volume:

$$E \approx \frac{1}{2\mu}\left(\frac{B_{\max} + \alpha B_{\max}}{2}\right)^2 \pi\left(R_c^2 H_c - H_w \sum_{1}^{N_w} R_{Oj}^2 - R_{Ij}^2\right) \tag{2.10}$$

where H_c is the core height and H_w is the winding thickness.

The small-signal inductance can be derived as

$$I_r^2 = \frac{1}{N^2}\left(\sum_{j=1}^{N_w} AT_j\right)^2 \tag{2.11}$$

$$I_r^2 = \frac{B_{\max}^2}{\mu^2 N^2}\left(\sum_{j=1}^{N_w}\left(\mathrm{H}_w(1 \pm \alpha) + 2\,\mathrm{R}_{ij} \cdot \ln\left(\frac{R_{oj}}{R_{ij}}\right)\right)\right)^2 \tag{2.12}$$

$$L = \frac{2E}{I_r^2} \tag{2.13}$$

$$L = \frac{\mu N^2 \cdot \left(\frac{1+\alpha}{2}\right)^2 \cdot \pi\left(R_c^2 H_c - H_w \sum_{1}^{N_w} R_{Oj}^2 - R_{Ij}^2\right)}{\left[\sum_{j=1}^{N_w}\left(H_w \cdot (1 \pm \alpha) + 2 \cdot R_{Ij} \cdot \ln\left(\frac{R_{Oj}}{R_{Ij}}\right)\right)\right]^2} \tag{2.14}$$

The ideal dc resistance is calculated from

$$R_{dc} = \frac{\rho_{cu} \cdot 2\pi}{H_w \ln(1/\alpha)} \cdot \sum_{j=1}^{N_w} n_j^2 \tag{2.15}$$

where ρ_{cu} and H_w are the resistivity and thickness of the winding, respectively.

Based on the number of turns calculated from (2.8), each winding window can be divided into different number of turns. Figure 2.4 shows an example of dividing the winding window j (with radius R_{ij} and R_{oj}) into eight turns, with spacing of *l* and *d* between the turns horizontally and vertically. The values of *l* and *d* depends on the winding configuration and fabrication clearance, suppose the total clearance is *ml* horizontally and *nd* vertically, then the effective radius becomes

$$R_{ij}' = R_{ij} + \frac{ml}{2} \qquad R_{oj}' = \mathrm{R}_{oj} - \frac{ml}{2} \tag{2.16}$$

The effective factor α is

$$\alpha_j = \frac{R_{ij}'}{R_{oj}'} = \frac{R_{ij} + ml/2}{R_{oj} - ml/2} \tag{2.17}$$

The effective winding thickness of winding window j becomes

$$H_{w\_e} = H_w - nd \tag{2.18}$$

Therefore, (2.15) can be modified to calculate the practical resistance:

$$R_{dc} \approx \frac{\rho_{cu} \cdot 2\pi}{H_{w\_e}} \cdot \sum_{j=1}^{N_w} \left(\frac{n_j^2}{\ln(1/\alpha_j)}\right) \tag{2.19}$$

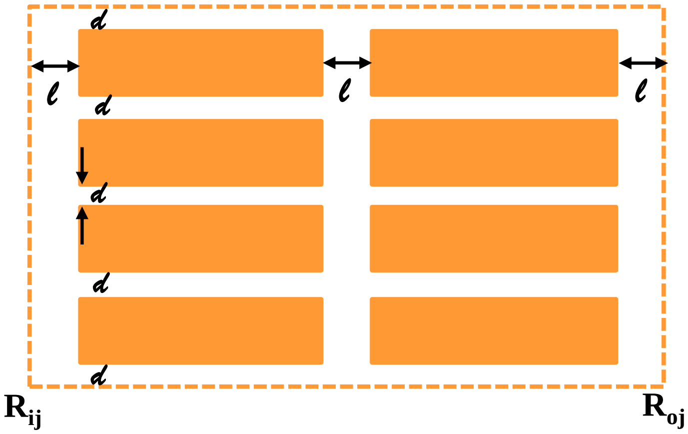

Figure 2.4. An example of modified structure of winding window j after considering the fabrication clearance on the horizontal and vertical direction where m = 3 and n = 5.

The time constant τ, which is the ratio of L to R_{dc}, is then given by

$$\tau = \frac{L}{R_{dc}} \tag{2.20}$$

where L and R_{dc} can be found in (2.14) and (2.15).

2.3 Design Rules

2.3.1 Selection of Uniformity Factor

Since the uniformity factor represents the uniformity level throughout the magnetic field in a constant-flux design, a relatively large uniformity factor is always preferred. Actually, for a given volume, an optimal uniformity factor always exists that gives the highest time constant, as discussed in Section 3.1. The optimal value of uniformity factor varies with different situations and input parameters such as the footprint and height of the inductor. However, the uniformity factor cannot always be ideally selected as the optimal value because it is usually limited by the fabrication constraints. The plate thickness, for example, which is defined as H_p and calculated from equation (2.2)-(2.6), decreases as α increases since thinner plate is need to increase the flux density. Figure 2.5 shows the effect of uniformity factor α on the plate thickness H_p. The plate thickness decreases continuously with increasing uniformity factor all the way to the line of fabrication limitation. Therefore, the uniformity factor cannot be as close to unity as possible after the fabrication limitations are taken into consideration. The limitation line is determined by the manufacturing process employed, and may have different values under different situations. Therefore, the uniformity factor should be selected as closed to the optimal value as possible without violating the fabrication constraints. As an example, the routing method introduced in Chapter 4 can achieve a plate thickness of no less than 0.3 mm, and the α selection should be kept below 0.75. For the parametric studies in Chapter 3, the uniformity factor is kept larger than 0.5 to ensure the constant distribution of the flux. Compared with the commercial product shown in Figure 1.4 (c) which has a uniformity factor around 0.03, a constant-flux inductor with 0.5 uniformity factor is 17 times better.

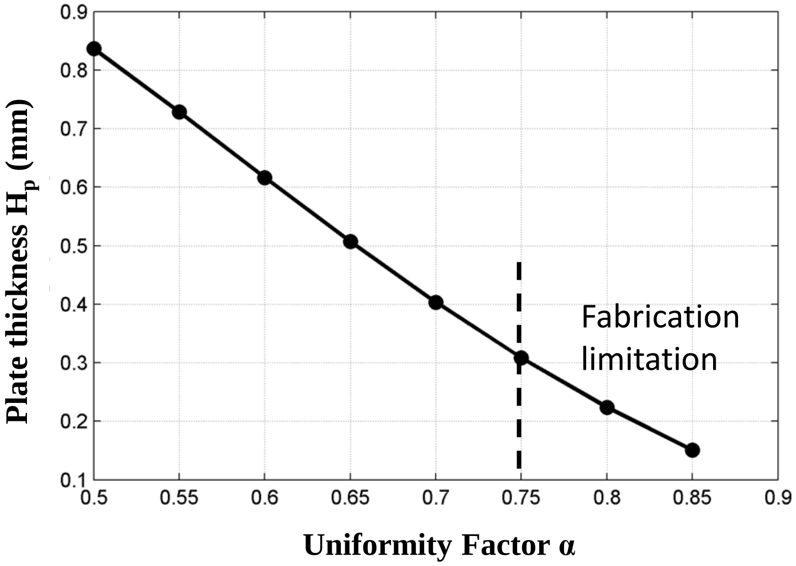

Figure 2.5. Relationship between plate thickness and uniformity factor α for R_c = 5 mm, H_c = 2 mm, B_{max} = 0.35 T, and $\mu = 35\mu_o$.

2.3.2 Number of Winding Windows

The procedure of constant-flux inductor design starts from the outermost area and calculates the radii of each winding window recursively. Therefore, the total number of winding windows inside the magnetic core becomes a user-defined factor.

Small width of winding windows adds difficulties for the fabrication for both the core and the winding (see Chapter 4), and should be avoided in the design. Based on the fabrication considerations, the user terminates the recursive calculation of the winding window when the width of any window violate fabrication limits. If the program is not terminated by the user, the calculation also stops at negative values of the radii calculated.

2.3.3 Current Rating and Maximum Flux Density B_{max}

There are two types of the current rating given by commercial products. One is concerned about heat, while the other is concerned about saturation. As an example, a commercial inductor from Maglayers [12] is studied with electrical ratings listed in Table I. The heat rated current is the dc current that will cause an approximate temperature rise of 40 ^{o}C, and the saturation rated current is the dc current that will cause the inductance to drop approximate 20%.

TABLE I ELECTRICAL RATINGS OF A COMMERCIAL INDUCTOR FROM MAGLAYERS [12]

Part Number	Inductance ±20% (μH)	R_{dc} (mΩ)	Heat rated current (A)	Saturation rated current (A)
MMD-10DZ-2R2M	2.2	7.0	12	27

The drop in inductance is caused by the non-linear B-H curve of the magnetic material. When the dc magnetizing current is high, the permeability of the magnetic material decreases and causes the reduction of inductance. In order to have an estimation of the saturation property of the commercial magnetic materials used to make the inductor, the following experiment was carried out to simulate the saturation flux density B_s of the commercial inductor.

As illustrated in Figure 2.6, an X-ray picture that reveals the inner winding structure of the commercial inductor was taken, based on which the solid model with matching dimensions can be constructed in finite element analysis (FEA) tools to simulate the inductance. A small current was applied to the model so that the inductor is kept away from saturation, and the value of permeability was adjusted until the inductance from simulation matches that of the datasheet. Knowing the simple permeability, non-linear B-H curves can be constructed with various saturation flux density B_s. The non-linear B-H curves with changing B_s were applied to the model until the inductance drop 20% with the saturation current provided by the datasheet. The value of B_s was found to be 0.9 T in this case.

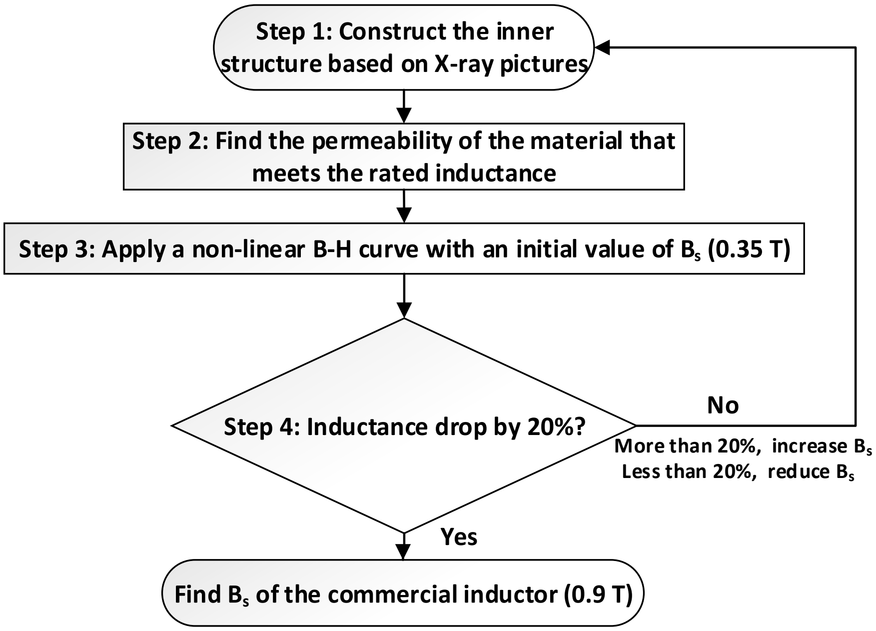

Figure 2.6. Flow chart of the experiment procedure to find the saturation flux density of the material used for the commercial inductor from Maglayers [12].

Different materials has different saturation flux densities. The magnetic composite used by Maglayers has an estimated saturation flux density of 0.9 T, but for ferrite materials, the saturation flux density is mostly around 0.3 T-0.4 T. For the constant inductor design, the nominal value of the maximum flux density is set to 0.35 T for most cases, so that the core is always kept from saturation.

The current rating I_r given by the design results of constant-flux inductor is the rated current that regulates the flux density throughout the core to stay at the level below saturation and the inductance remains constant for any current below that rated current. The saturation current of the inductor designed is based on the B-H curve applied and obtained from simulation.

2.3.4 Circular and Rectangular Structure

The behavioral model and the equations derived above are based on the 2D axisymmetric structure as demonstrated in Figure 2.1. Ideally, the 3D solid model that evolved from the 2D design has circular windings enclosed by a circular core with radius R_c, as illustrated in Figure 2.7(a). The core and the winding can also be designed to square shapes, as shown in Figure 2.7(b), depends on fabrication preference. If the core and winding are modified to be square, the inductance will be approximately 4/π larger than the one calculated by (2.14) since the volume is larger:

$$L_{square} \approx \frac{\mu N^2 \cdot (\frac{1+\alpha}{2})^2 \cdot 4 \cdot (R_c^2 H_c - H_w \sum_{1}^{N_w} R_{Oj}^2 - R_{Ij}^2)}{[\sum_{j=1}^{N_w} (H_w \cdot (1 \pm \alpha) + 2 \cdot R_{Ij} \cdot \ln(\frac{R_{Oj}}{R_{Ij}}))]^2} \tag{2.21}$$

The resistance will also be 4/π larger than the one calculated by (2.15):

$$R_{dc\_square} \approx \frac{\rho_{cu} \cdot 8}{H_w \ln(1/\alpha)} \cdot \sum_{j=1}^{N_w} n_j^2 \tag{2.22}$$

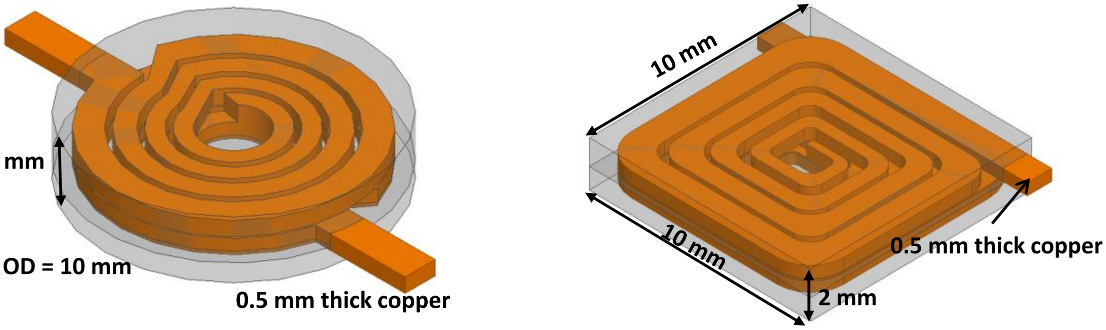

(a) (b)

Figure 2.7. Solid model of constant-flux inductor designed with (a) circular winding and core and (b) rectangular winding, where $\mu = 22\mu_0$, B_{max} = 0.35 T, and α = 0.65. FEA simulation result shows L = 1.31 μH and R = 5.5 mΩ for the structure in (a); L = 1.6 μH and R = 7 mΩ for the structure in (b).

2.4 Design Algorithms

2.4.1 Design for Minimal Volume

Given the required inductance and resistance, a design process is formulated by iterating the dimension of the core and the winding until the required target is achieved.

As shown in Table II, the target of the constant-flux inductor design is to achieve the inductance L_{req}, and dc resistance R_{req} with the minimal volume required. The constant-flux concept is applied by using the equations in Section 2.2 to shape the flux distribution and keeping the uniformity factor no less than 0.5 to ensure the uniformity level. The electrical inputs include the maximum magnetic flux density B_{max}, core permeability μ, uniformity factor α, and rated current I_r. The mechanical parameters include the plate thickness H_p, core radius R_c, and core height H_c, which may be stepped in the iteration process.

TABLE II DESIGN PARAMETERS FOR CONSTANT-FLUX INDUCTOR

Objective:	Meet requirement of inductance L_{req} and resistance R_{req}
Inputs:	B_{max} maximum flux density allowed in the core
	μ permeability of magnetic material
	I_r rated current
Variables:	α uniformity factor (iterated in the process)
	H_p plate thickness (iterated in the process)
	H_c height of the inductor (iterated in the process)
	R_c outer radius of the core (iterated in the process)
Outputs:	R_{Ij}, R_{Oj} inner and outer radius of winding window j
	AT_j ampere-turns current carried by each window
	n_j number of winding turns in each window
	L resulted inductance (to compare with L_{req})
	R_{dc} resulted dc resistance (to compare with R_{req})

With the initial values of H_p, R_c, and H_c, the uniformity factor α is swept from 0.5-0.8 (upper range determined by fabrication limitation) at the first place, to find the resulted inductance L and resistance R_{dc}. If the results do not meet L_{req} and R_{req} whichever α is, the dimensions such as H_p, R_c, and H_c are incremented as a next step to repeat the sweeping again until the required inductance and dc resistance are met. The procedure is described below with the flow chart in Figure 2.8, assuming that H_p is swept and constrained by manufacturing limitations.

Step 1: Initialize or increment H_p. The initial value of H_p to start with can be as small as half the dimension from benchmark commercial products, and slowly increase the value of H_p until the inductance can be met.

Step 2: Determine the radius R_{O1} of the outermost winding window (j = 1) from (2.2).

Step 3: Find all other radii of the winding windows from (2.4) and (2.5). The total number of winding windows N_w is limited by manufacturing constraints.

Step 4: Find the inductance from (2.10) and (2.14). If the inductance requirement has not been met, return to Step 1. Otherwise, proceed to the next step.

Step 5: Find the number of turns from (2.7) and (2.8).

Step 6: Find the dc resistance from (2.15). If the resistance requirement cannot be met, increase the core dimensions and repeat the procedure.

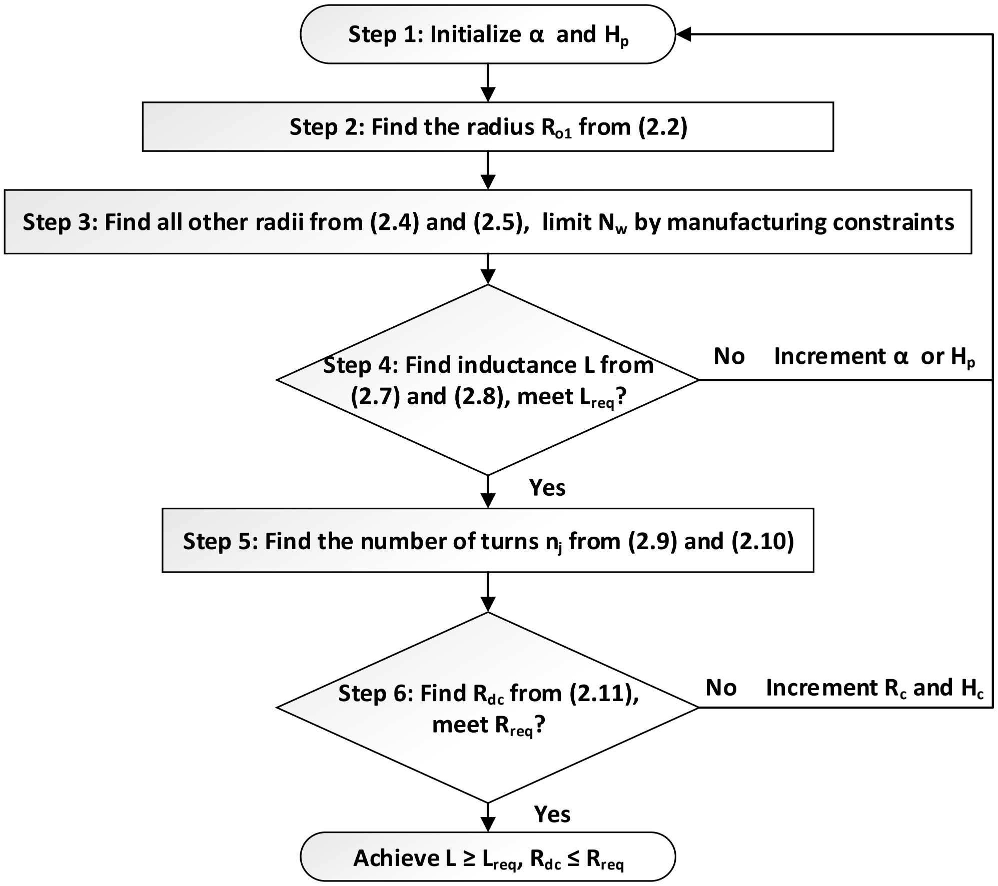

Figure 2.8. Flow chart of the constant-flux design procedure to find the minimal volume satisfying specified inductance and resistance.

This design method gives the minimum volume that is required to meet the target as a result. In practical situations, when there is a requirement on the inductance and the maximum dc winding loss while the volume of the inductor is not pre-determined, the proposed design procedure for minimal volume can be carried out to construct a constant-flux inductor with low profile and high energy density.

2.4.2 Design for Maximal Time Constant

Given the specified footprint area and the total thickness of the core, another design procedure is formulated to look for the configuration that gives the highest time constant value within the given dimensions of the core. The input and output parameters are shown in Table III, for a specific inductance, the dc winding resistance is minimized by this procedure.

As shown in Table III, the target of the design is to obtain the highest time constant τ within the footprint and thickness specified. The constant-flux concept is applied by using the equations in Section 2.2 to shape the flux distribution and keeping the uniformity factor no less than 0.5 to ensure the uniformity level. The electrical inputs include the maximum magnetic flux density $B_{\max}$, core permeability μ, uniformity factor α. The mechanical inputs include the outer radius of core R_c, and core height H_c. Different from the design for minimal volume introduced in 2.4.1, the plate thickness H_p herein is calculated rather than swept according to the selection of uniformity factor α. The iteration process only occurs when α is swept, and the iterations on the dimensions such as H_p, H_c, and R_c are eliminated from the process.

TABLE III DESIGN PARAMETERS FOR CONSTANT-FLUX INDUCTOR

Objective:	Obtain the highest time constant τ	
Inputs:	B_{max}	maximum flux density allowed in the core
	μ	permeability of magnetic material
	I_r	rated current
	R_c	outer radius of the core
	H_c	height of the inductor
Variable:	α	uniformity factor (iterated in the process)
Outputs:	H_p	plate thickness
	R_{Ij}, R_{Oj}	inner and outer radius of winding window j
	AT_j	ampere-turns current carried by each window
	n_j	number of winding turns in each window
	L	resulted inductance

	R_{dc}	resulted dc resistance

The procedure is described below with the flow chart in Figure 2.8, assuming that the uniformity factor α is swept and selected at the optimal value that gives the peak value of time constant neglecting manufacturing constraints.

Step 1: Initialize or increment uniformity factor α with specified R_c and H_c.

Step 2: Find the plate thickness H_p, outer and inner radius R_{O1}, R_{I1} of winding window 1, and outer radius R_{O2} of winding window 2 from (2.2) and (2.4)-(2.6). There are four unknowns in four equations, so the four parameters can be solved at the same time.

Step 3: Find all other radii of the winding windows from (2.4) and (2.5). The total number of winding windows N_w is limited by manufacturing realities.

Step 4: Find the time constant from (2.20) based on the winding structures calculated. Go back to step 1 is the uniformity factor value doesn't give the highest time constant.

Step 5: Winding configuration in forms of winding windows is constructed with the highest time constant. Target achieved.

In step 4, the magnetic flux density B_{max} is used to calculate the energy and the ampere-turns AT_j is used to calculate dc winding loss. Therefore, the actual number of turns in each wining window remains unknown. The number of turns n_j depends on the specified current rating, and affects the values of the inductance and resistance. Therefore, once step 5 is accomplished, the structure is ensured to give the best time constant, but the determination of the actual value of the inductance and resistance needs to be performed as the follow-up steps:

Follow-up Step 1: If the current rating I_r is specified, the number of turns n_j in each winding window can be obtained from (2.8).

Follow-up Step 2: The inductance can be calculated from (2.10) and (2.14), and the resistance can be calculated from (2.8) and (2.15).

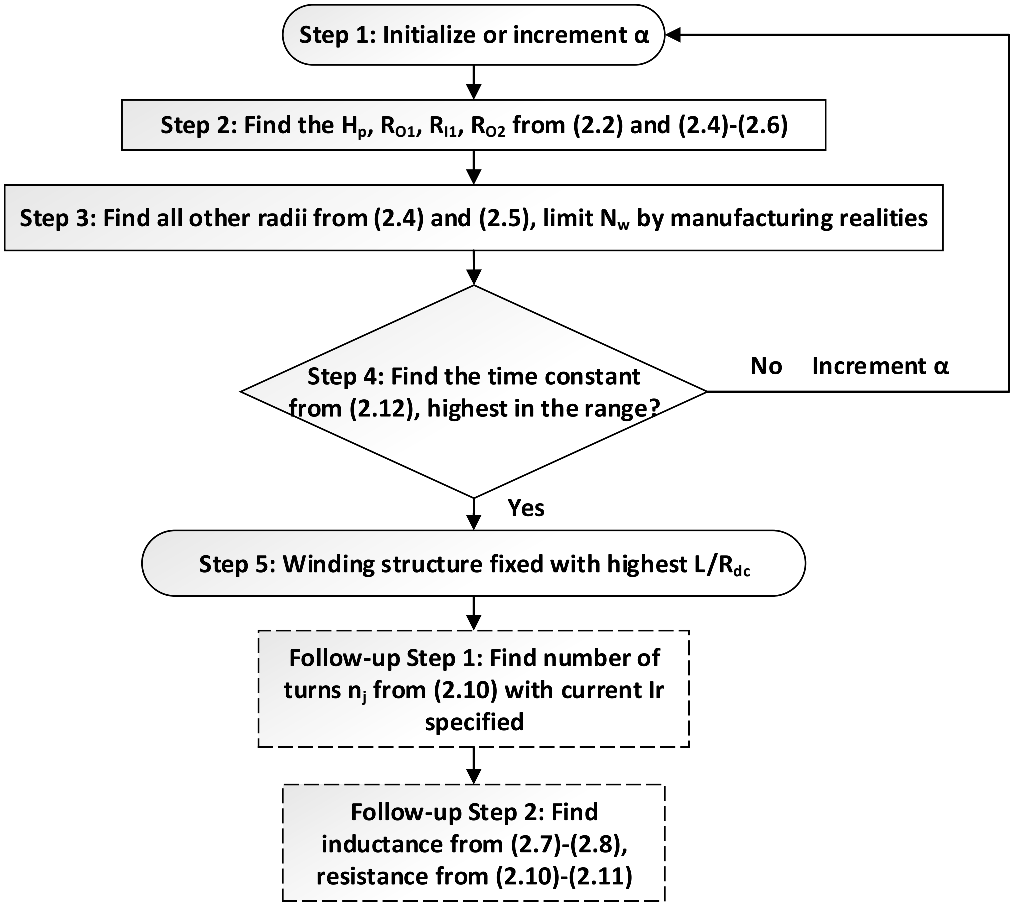

Figure 2.9. Flow chart of the constant-flux design procedure to find the maximal time constant within specified inductor footprint area and height.

This design method discussed above gives the optimized structure that has the highest time constant by sweeping uniformity factor α. In practical situations, when the inductor volume is pre-determined and the inductance is specified, this design procedure can be carried out to give a design that has the dc winding resistance minimized.

2.5 Design Example

The constant-flux inductor can be particularly advantageous in optimizing the space utilization of low-profile inductors. As an example, the design algorithm in section 2.4.1 is employed in this section with an example; and the second design algorithm in section 2.4.2 to be employed for the parametric studies in Chapter 3. The design example herein has a target inductance of 1.5 μH and a target resistance of 7 mΩ, the same as those of the commercial inductor [19]. The objective is to minimize the inductor's volume in a sense of height reduction. The procedure outlined in the design for minimal volume yields a volume of $10 \times 10 \times 2$ mm^3 for L =1.6 μH, I_r = 10 A, and R_{dc} = 7.0 mΩ. The commercial inductor [19] with comparable ratings (L =1.5 μH, I_r = 10 A, and R_{dc} = 8.1 mΩ) would occupy $10.3 \times 10.5 \times 4$ mm^3, two times the volume of the constant-flux inductor.

2.5.1 Design Results

Based on the core material that is used for fabrication, the relative permeability for the design is 22, and the maximum flux density B_{max} is 0.35 T. The plate thickness H_p is restricted to 0.5 mm and the uniformity factor α is set at 0.65 owing to the limitation of prototype equipment. Since the objective for this design example is to obtain as small volume as possible to shrink the total size of a commercial inductor with the same inductance and resistance, the design flow chart shown in Figure 2.8 is applied and outlined here:

Step 1: The plate thickness H_p is set to the value of 0.5 mm, and α is selected to be 0.65. The outer radius of the inductor R_c is initialized to be 5 mm, and the initial value of the inductor height is 2 mm.

Step 2: Based on the Gauss' law, the outer radius of the first winding window (numbered from the outer area to the center of the core) R_{O1} can be solved from (2.2), which is 4.5 mm.

Step 3: The inner radius of the first winding window R_{I1} is then obtained from (2.4) to be 2.9 mm, which is α times the outer radius R_{O1}. Successively, all the other radii can be determined from (2.4) and (2.5), as listed in Table IV. The total number of winding windows is selected to be three since the radius of the innermost winding should be no less than 1 mm considering the fabrication efforts.

Step 4: Then the inductance can be calculated from (2.14), which is 1.6 μH in this example, slightly higher than the required 1.5 μH.

Step 5: The ampere-turns in each window AT_j ($j = 1, 2, 3$) can be calculated as 52.6 A, 23.7 A, and 15.3 A, respectively, from (2.7), and the value of the number of turns n_j in each window AT_j ($j = 1, 2, 3$) are approximated to 4, 2, and 2 from the 10 A current rating I_r by using (2.8), so that the winding turns can be distributed into two layers.

Step 6: The dc resistance calculated from (2.15) is 7 mΩ, which meets the requirement.

The design example presented above does not show the iteration process since the inductance and resistance both meet the requirement at the same time. If the inductance is smaller than the requirement, or the resistance is larger than the requirement, we need to consider increasing the footprint or the height the inductor in the iteration. Theoretically, the calculated inductance of 1.6

μH is still slight higher than the required 1.5 μH, so the volume can be further reduced a little. However, we want to leave some margin for non-ideal factors in the fabrication and errors in the calculation, so the finalized volume of the constant-flux inductor is fixed at 10 × 10 × 2 mm^3. Table IV summarizes all the final design results.

TABLE IV DESIGN RESULTS OF CONSTANT-FLUX INDUCTOR

INPUTS					
B_{max} (T)	**R_c (mm)**	**H_c (mm)**	**α**	**I_r (A)**	**μ**
0.35	5	2	0.65	10	22 μ_0
OUTPUTS					
Winding Window		**R_{Oj} (mm)**	**R_{Ij} (mm)**	**AT_j (A)**	**n_j**
j = 1		4.5	2.9	52.6	4
j = 2		2.7	1.7	23.7	2
j = 3		1.5	1.0	15.3	2
Total thickness of winding (H_w)				1 mm	
Inductance calculated (L)				1.6 μH	
Dc resistance calculated (R_{dc})				7.0 mΩ	
Volume relative to commercial product				1/2	

j is numbered from the outer edge to the center of the core.

2.5.2 3D Finite-Element Verification of Design Example

The parameters listed in Table IV are used to construct the ideal structure of the constant-flux inductor designed, as shown in Figure 2.10. The uniformity of the flux distribution is consistent with α = 0.65.

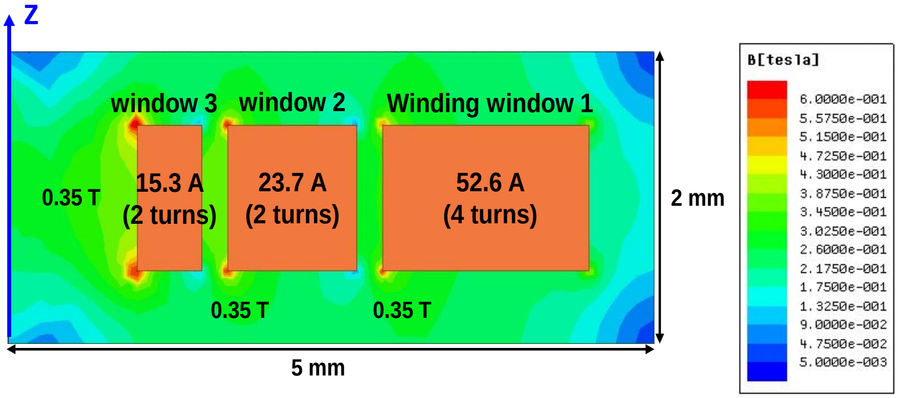

Figure 2.10. Relative uniform flux density distribution (α = 0.65) across an axisymmetric cross-section using the designed parameters in Table IV.

Based on the ideal structure, a solid model was constructed for fabrication with the dimensions listed in Table V and illustrated in Figure 2.11 (a). For fabrication considerations, the winding was configured to have two layers which start from the top terminal, spirals counterclockwise toward the center, connects to the bottom winding layer at the center, and spirals counterclockwise to the bottom terminal. The spacing between adjacent winding turns was kept at no less than 0.2 mm due to limitation of prototyping equipment. The 3D map of the flux-vector density in Figure 2.11 (b) shows no significant flux crowding as the peak magnetic flux density was limited to 0.35 T. The simulated inductance of the solid model of the constant-flux inductor designed is 1.53 μH, and the resistance is 7.3 mΩ. The inductance is 4.4% smaller than the calculated result mainly because of the non-ideal 0.2 mm spacing between the winding turns that caused shrinkage in the effective core volume. The resistance 7.3 mΩ is 4.3% larger than the calculated result because of the reduced widths of the winding turns caused by the 0.2 mm spacing.

TABLE V DIMENSIONS FOR FABRICATION OF AN INDUCTOR HALF

Winding Turn	**R_{Oj} (mm)**	**R_{Ij} (mm)**
j = 1	4.8	3.8
j = 2	3.6	2.9
j = 3	2.7	1.9
j = 4	1.5	1.0
Thickness of winding (mm)		0.5
Thickness of an inductor half (mm)		1.0
Footprint of an inductor half (mm)		10 × 10

j is numbered from the outer edge to the center of the core.

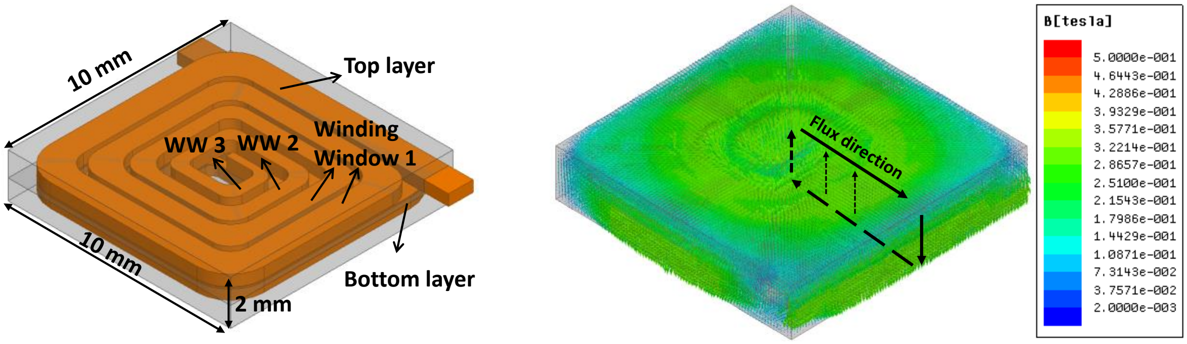

(a) (b)

Figure 2.11. (a) Solid model of the constant-flux inductor in Maxwell with square-shape winding with a inductance of 1.53 μH and a resistance of 7.3 mΩ; 0.2 mm non-ideal gap was inserted between the winding turns in each layer due to fabrication limitations; (c) flux-vector plot of uniform flux density distribution throughout the core volume except near the edges.

To find the saturation current of the inductor designed, 8 A – 38 A current is applied to the solid model shown in Figure 2.11 (a). The sweeping result is shown in Figure 2.12. With an assumed 0.9 T saturation flux density, the inductance drop by 20% when the current is 32 A.

Therefore, the saturation current is found to be 32 A. Compared to the commercial product in section 2.3.3, the saturation current is improved by 18% because of the uniformity of the flux distribution.

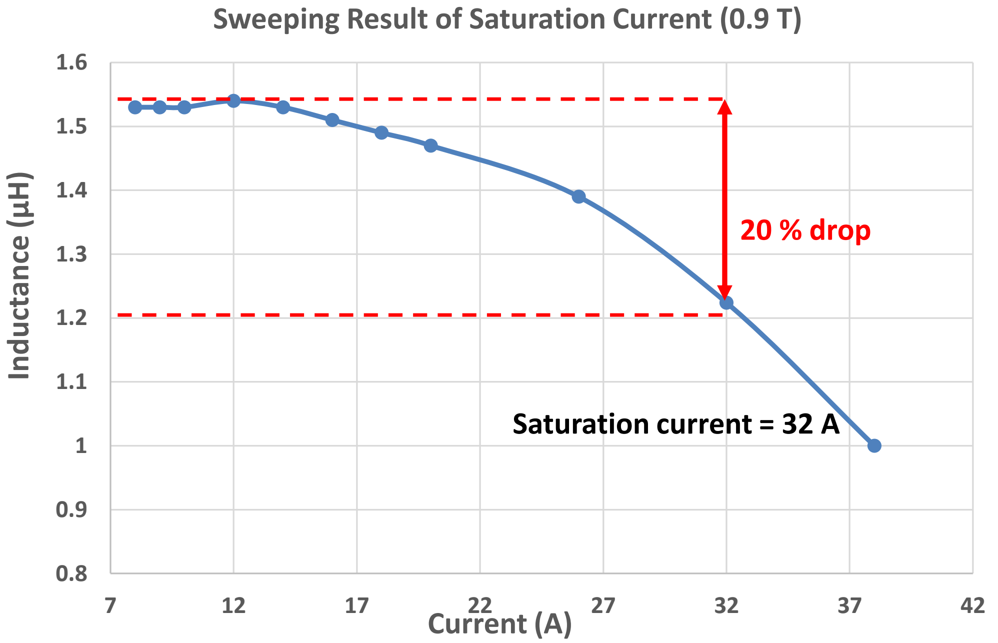

Figure 2.12. Sweeping result of current applied on the constant-flux inductor designed in Figure 2.11 with 0.9 T saturation flux density and 22μ_o permeability.

Chapter 3 Parametric Study of Constant-Flux Inductor

To facilitate the design of the constant-flux inductor, it is necessary to know the influence of the input parameters such as the inductor dimensions and the magnetic material properties on the design parameters of the inductor model. Therefore, the parametric study is carried out based on the model from the design procedure outlined in section 2.4.2. In the analysis discussed in this chapter, the sweeping parameters include the outer radius of the core R_c, height of core H_c, uniformity factor α, permeability of the magnetic material μ, and the maximum flux density B_{max}; the design parameters include the all the radii of the winding windows R_{Oj} and R_{Ij}, the plate thickness H_p, the number of turns N, and the time constant τ. The relationship of inductance and resistance will be discussed separately later. Table VI gives the nominal value and the sweeping range of the parameters studied, and Table VII gives the design parameters and metrics to be plotted for all the cases.

TABLE VI NOMINAL VALUES AND SWEEPING RANGE OF THE INPUT PARAMETERS

Input parameters	**Nominal value**	**Sweeping range**
Footprint radius R_c (mm)	5	3-5
Thickness H_c (mm)	2	1-3
Uniformity factor α	Value with peak time constant	0.5-0.8
Relative permeability (μ_o)	35	25-35
Maximum flux B_{max} (T)	0.35	0.1-0.35

TABLE VII DESIGN PARAMETERS AND METRICS

Design parameters	**Metrics in the plots**
Radii of the winding windows R_{Oj}, R_{Ij} (j = 1, 2, 3…)	mm
Plate thickness H_p ($H_w = H_c - 2H_p$)	mm
Total number of winding turns N ($N = \sum_{j=1}^{N_w} n_j$)	--

Time constant τ	μs

When some of the parameters are being swept, the other parameters are kept at the nominal values. For example, keeping the footprint radius R_c at the nominal value of 5 mm, means that the footprint of the inductor is 10 mm × 10 mm while the other parameters are being studied. The nominal value of the uniformity factor α is the one that has the peak value of time constant for a given volume to ensure that the design is optimized, the effect of different parameters will be discussed in detail in the following section.

3.1 Effect of Uniformity Factor α, Footprint Radius R_c, and Height H_c

Changing the uniformity factor directly affects the number of winding windows as well as the radii of each winding window. As shown in Figure 3.1, increasing the uniformity factor requires more winding windows to achieve the uniformity level.

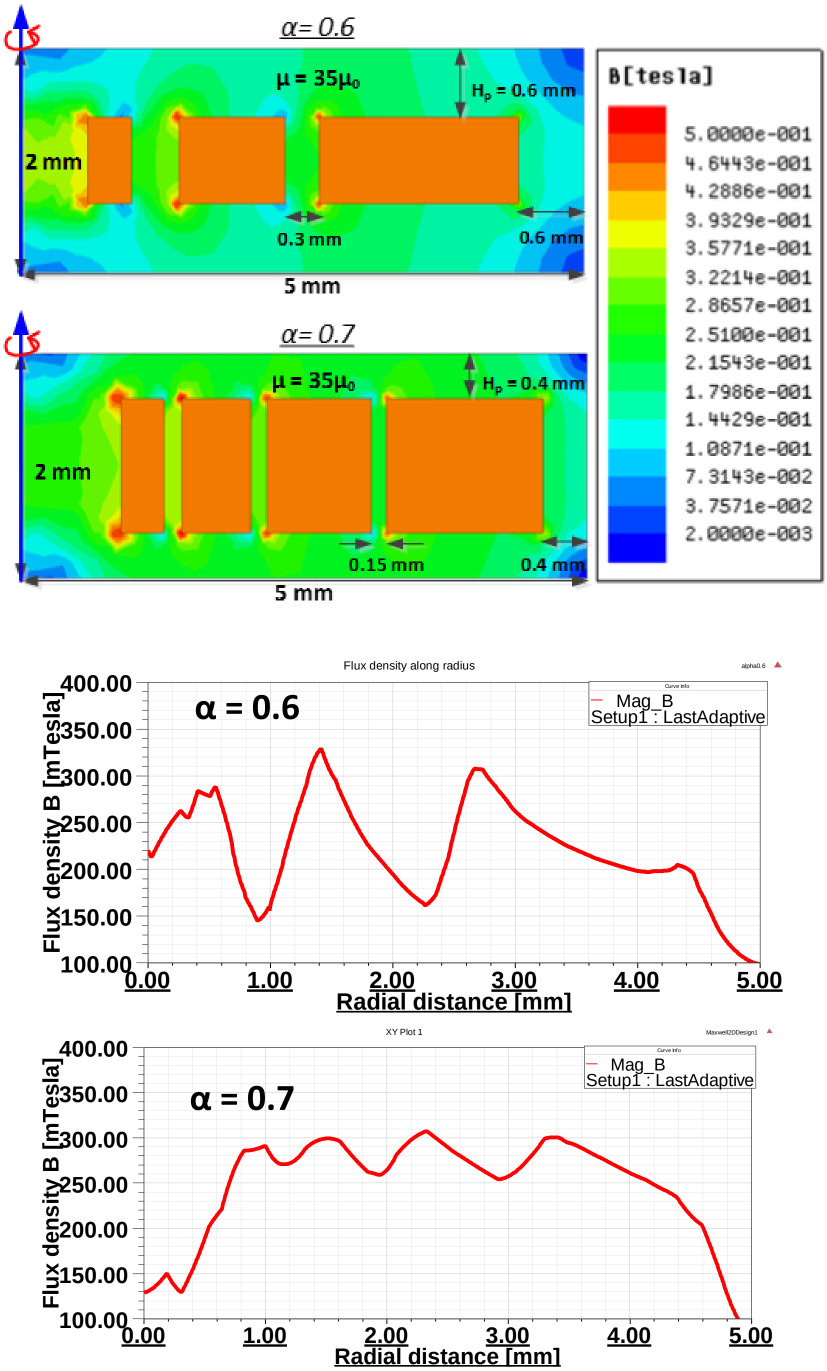

Figure 3.1. Designed dimensions of α = 0.6 and α = 0.7 for R_c = 5 mm, H_c = 2 mm, B_{max} = 0.35 T, and $\mu = 35\mu_o$.

3.1.1 Effect on Time Constant

As for the time constant, varying the uniformity factor gives different configurations of the winding structure. Although high uniformity level is always preferred, it also brings high conductor loss in the winding, since the number of turns increases according to (2.7) and (2.8). The relationship between the uniformity factor α and the time constant τ is shown in Figure 3.2 (the Matlab code is shown in Appendix D) when the number of winding windows is limited at three. The time constant is calculated from (2.20), which equals the ratio of energy to dc winding loss. The energy is related to the magnetic field and volume by (2.10), and the dc winding loss is related to the ampere-turns by (2.15). Therefore, the time constant herein is only concerned about the ampere-turns without specifying the current rating and taking the inductance and resistance into calculation. Once the current rating is specified, the values of the inductance and resistance can be determined.

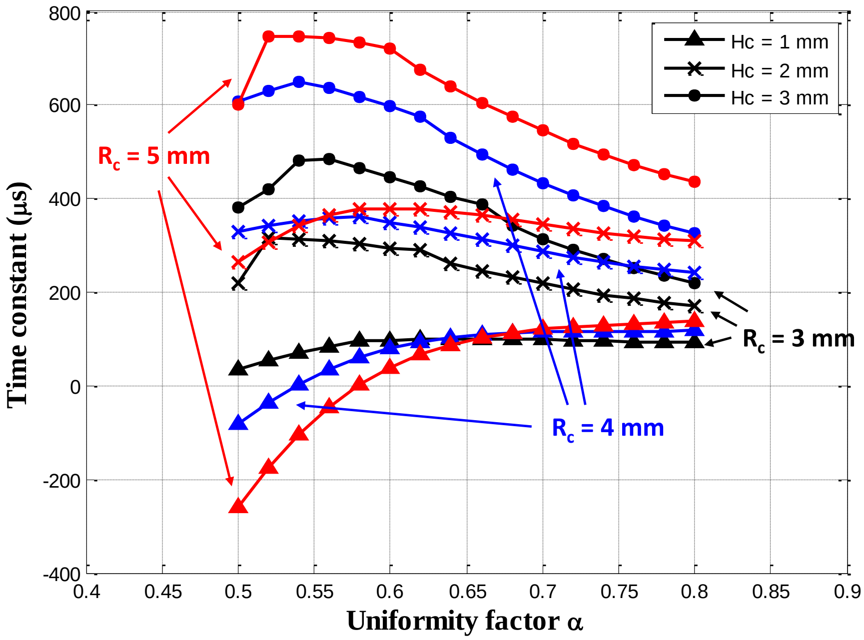

Figure 3.2. Relationship between time constant and uniformity factor for R_c = 3, 4, 5 mm, H_c = 1, 2, 3 mm, B_{max} = 0.35 T, and $\mu = 35\mu_o$.

The red curves in Figure 3.2 show the time constant versus uniformity factor under different inductor heights when the footprint radius R_c is 5 mm, whereas the blue and black curves show the relationship between time constant and uniformity factor when the footprint radius is 4 mm and 3 mm, respectively. A small uniformity factor suggests a low uniformity level in the core volume, therefore, the space is not fully utilized and the average energy density is low. As a consequence, the time constant is low. As the uniformity factor increases, both the energy density and the dc winding loss increase. However, the energy density increases faster than the dc winding loss until the time constant reaches its peak value, where the ratio of inductance to resistance is the highest. After the peak condition, the energy density is restricted by the saturation flux density and winding loss increases faster than the energy density, so the time constant begins to drop. At the peak value of time constant, the dc resistance is minimized for a constant inductance value.

The optimal uniformity factor α depends on dimensions. As shown in the figure, When the inductor height is 2 mm or 3 mm, each curve has a peak value of the time constant ranging from 0.5-0.7. However, at smaller core thicknesses, such as 1 mm, the time constant increases slightly with increasing uniformity factor, which means that the increasing rate of the energy is similar to that of the winding loss. Nevertheless, when the uniformity factor is very low, such as 0.5, the time constant becomes a negative value, which suggests no solution can be found to construct the constant-flux structure. This is because the plate thickness exceeds the total thickness of the inductor and leads to negative value of energy stored in the core volume. The plot of plate thickness versus uniformity factor can be found in Figure 3.4. The internal parameters of each curve in Figure 3.2 are plotted in the following sections in order to validate the structure. In general, the larger the footprint radius or the inductor height, the larger the time constant, because the magnetic material has a larger volume to store energy at a higher core thickness, and the optimal value of α varies under different dimensions of the inductor.

3.1.2 Effect on Radii of the Winding Windows

Figure 3.3 shows the radii of each winding window according to the sweeping range of the uniformity factor under different footprint radius and inductor height. The width of the winding windows is limited at no less than 0.5 mm considering practical feasibility. As can be observed from the figure, the widths between the winding windows R_{Ij}-$R_{O(j-1)}$ decrease as the uniformity factor increase. The winding windows are closer to each other with the increase of uniformity factor in order to achieve the high level of the uniformity in flux distribution. Therefore, more winding windows are needed to maintain the uniform flux distribution under larger uniformity factor.

The number of winding windows increases with the increase of uniformity factor. For example, when the footprint radius is 5 mm and the inductor height is 3 mm, the uniformity factor has to be at least larger than 0.65 to have three winding windows; and in the case where footprint radius is 3 mm and the inductor height is 3 mm, the uniformity factor has to be at least 0.8 for three winding windows. he cutting off value of uniformity factor is not only related to the footprint radius, but also related to the inductor height. Different inductor heights with the same footprint radius lead to different cutting off uniformity factors. Therefore, the number of the winding windows depends on the combination of the footprint radius and the inductor height.

The inner radius R_{Ij} of winding window j, is α times of the outer radius R_{Oj} of winding window *j*, which is given by (2.4) based on Gauss’ law. Therefore, the width of winding window j is related to the outer radius and α by

$$R_{Oj} - R_{Ij} = (1 - \alpha) R_{Oj} \tag{3.1}$$

where R_{Oj} is calculated recursively from the last winding window. Figure 3.3 shows that the width of each winding window first increases and then decreases as the uniformity factor decreases. However, the width between the winding windows, such as R_{I1}-R_{O2}, always increases with the decrease of the α.

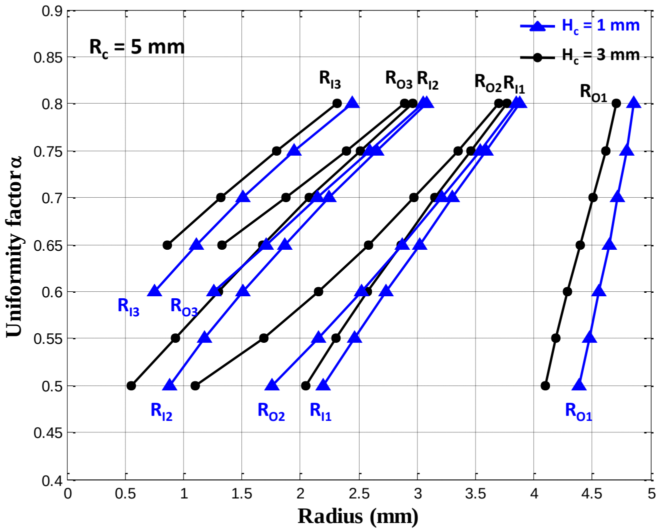

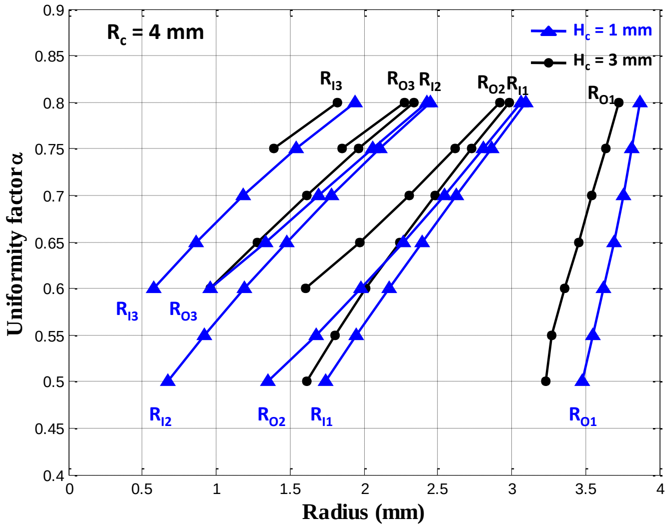

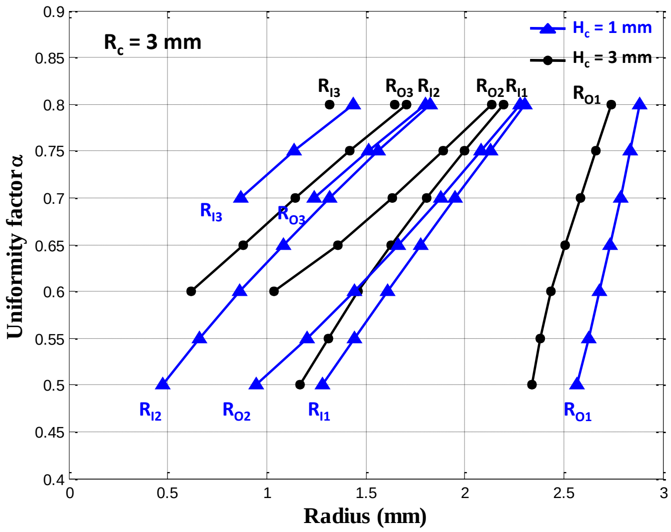

Figure 3.3. Plots of the radii of the winding windows against uniformity factor α for R_c = 3, 4, 5 mm, H_c = 1, 3 mm, B_{max} = 0.35 T, and $\mu = 35\mu_o$.

3.1.3 Effect on Plate Thickness

The plate thickness H_p is related to the winding thickness H_w by (2.3), and it is obtained by solving equations (2.2) and (2.4)-(2.6) together with the other three unknowns as mentioned in section 2.4.2. The relationships between H_p and uniformity factor α under different footprint radii and inductor heights are shown in Figure 3.4. As the uniformity factor increases, the plate thickness reduces in order to improve the flux density in the core volume. Under the same inductor height, larger footprint radius of the inductor leads to larger plate thickness; under the same footprint radius, larger inductor height leads to larger plate thickness.

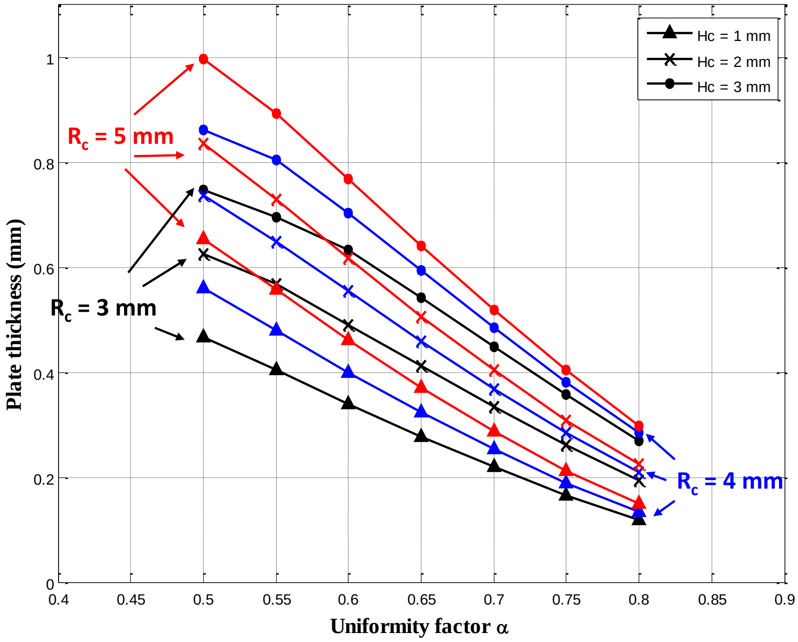

Figure 3.4. Plots of plate thickness H_p against uniformity factor for R_c = 3, 4, 5 mm, H_c = 1, 2, 3 mm, B_{max} = 0.35 T, and $\mu = 35\mu_o$.

3.1.4 Effect on Total Number of Turns

If a specific current rating is given, the number of turns in each winding window can be calculated by (2.8). With the increase of current rating, the number of turns reduces. The number of turns is also related to the uniformity factor since more turns are needed when α is large. Figure 3.5 shows the relationship between the number of turns and the uniformity factor with a specified current rating of 10 A. As can be observed from the figure, when the uniformity factor is smaller, there are less turns in the winding windows, and when the footprint radius or the inductor height is larger, the number of turns increases with the same uniformity factor since larger volume needs more turns to fill in the space to maintain the uniformity of the flux distribution.

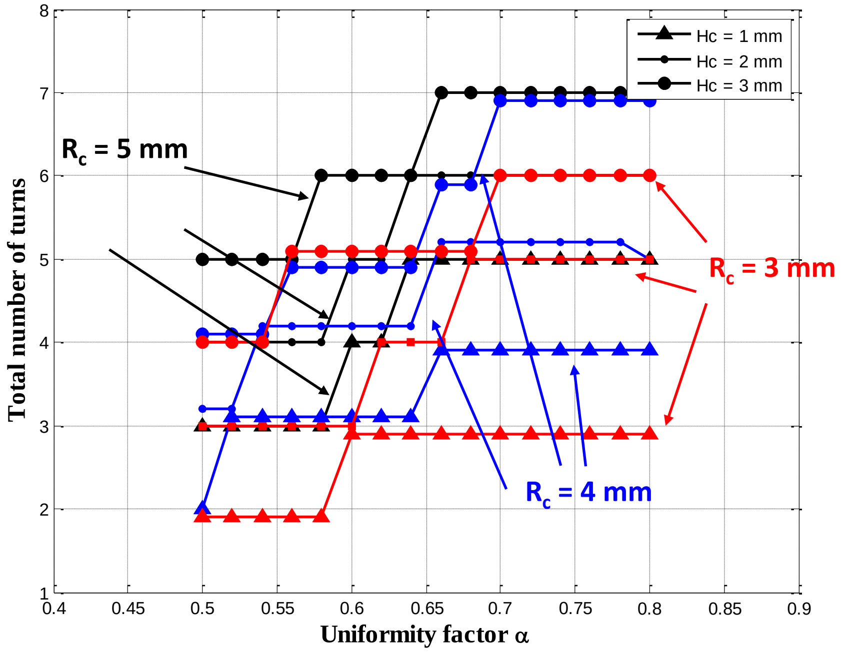

Figure 3.5. Plots of the total number of winding turns against uniformity factor for R_c = 3, 4, 5 mm, H_c = 1, 2, 3 mm, B_{max} = 0.35 T, $\mu = 35\mu_o$, and current rating I_r = 10 A.

3.2 Effect of Magnetic Core Properties

Inductor performance heavily depends on the properties of the magnetic core material [20], [21]. Composite powdered-metal cores, such as powdered iron, Kool Mu®, and Permalloy powder cores are commonly used in inductors and flyback transformer applications. The effective permeabilities are in the range of $15\mu_o$-$200\mu_o$ because of the varying particle size and amount of magnetically inert material in the composite mix. The saturation flux density B_{sat} of this kind of material is much higher than that of a ferrite core (0.8 T vs. 0.3 T), and the material permits a much smaller inductor than a gapped ferrite does for the same application under low operation frequencies.

Most of the commercial surface-mounted inductors with winding packaged inside use a powdered-metal composite as the core material, since the composite can carry high current rating with its high saturation flux density and is suitable for injection molding. The effective permeability varies from $15\mu_o$ to $35\mu_o$, depending on composite used. The saturation flux density usually can reach 0.5 T-0.6 T, beyond which the inductor begins to saturate and the inductance starts to drop. In the following analysis, the sweeping range of the permeability and the maximum flux density allowed (B_{max}) are set to $20\mu_o$-$30\mu_o$ and 0.1 T-0.35 T, respectively, to keep the core far from saturation.

3.2.1 Effect of Permeability

If the relative permeability is kept as a stepping factor while the uniformity factor is swept from 0.5 to 0.8, and the maximum flux density B_{max} is swept from 0.1 T-0.35 T, the relationships between time constant and uniformity factor are shown in Figure 3.6. The three cases have the same peak uniformity factor of 0.6, and the magnitude of the time constant is determined by the permeability of the magnetic core material. The higher the permeability, the higher the magnitude of the time constant. Although B_{max} is swept under each permeability, there is no change on the time constant, and the curve remains identical under different B_{max}. This conclusion suggests that for an inductor design, higher permeability is always preferred since the inductor's performance can be improved by increasing the permeability directly.

Since the permeability of the magnetic material μ is not involved in the equations (2.2)-(2.6) that are used to derive the radii, changing the permeability results in the same radii of each winding window; therefore, the structure under different permeabilities shown in Figure 3.6 remains constant under the same uniformity factor. The plots of the radii and the plate thickness are identical to those shown in Figure 3.3 and Figure 3.4, so the figures and discussions are omitted here.

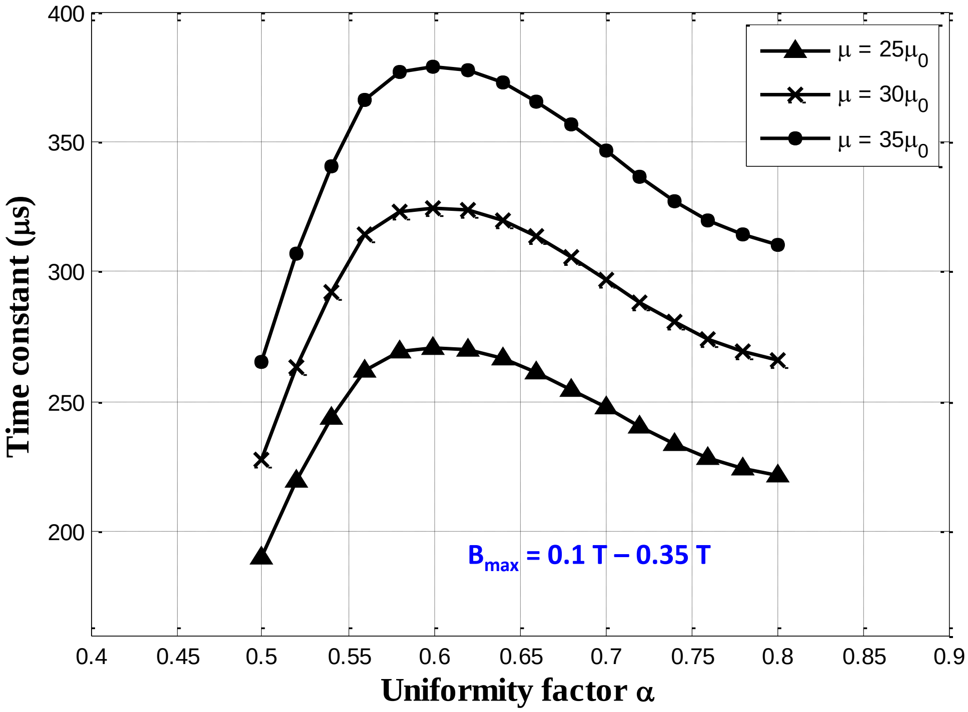

Figure 3.6. Plots of time constant against uniformity factor at different relative permeability for R_c = 5 mm, H_c = 2 mm, and B_{max} = 0.1 T - 0.35 T.

However, the permeability affects the number of turns in each winding window by changing the ampere-turns that the winding window carries. Rewriting equations (2.7) and (2.8), the number of turns in winding window j can be expressed by

$$n_j = \frac{AT_j}{I_r} = \frac{1}{I_r \cdot \mu}\left[H_w \cdot (B_{\max} \pm \alpha B_{\max}) + 2 \cdot B_{\max} \cdot R_{Ij} \cdot \ln(\frac{R_{Oj}}{R_{Ij}}) \right] \tag{3.2}$$

where the items in the brackets are the ones that remains constant, and n_j is inversely proportional to the permeability. Figure 3.7 shows the relationship between the number of turns and the uniformity factor at different permeabilities with a specified current rating of 10 A. As can be observed from the figure, when the permeability is larger, there are less turn in the winding windows. Since the number of turns is rounded, point A and point B coincides with each other.

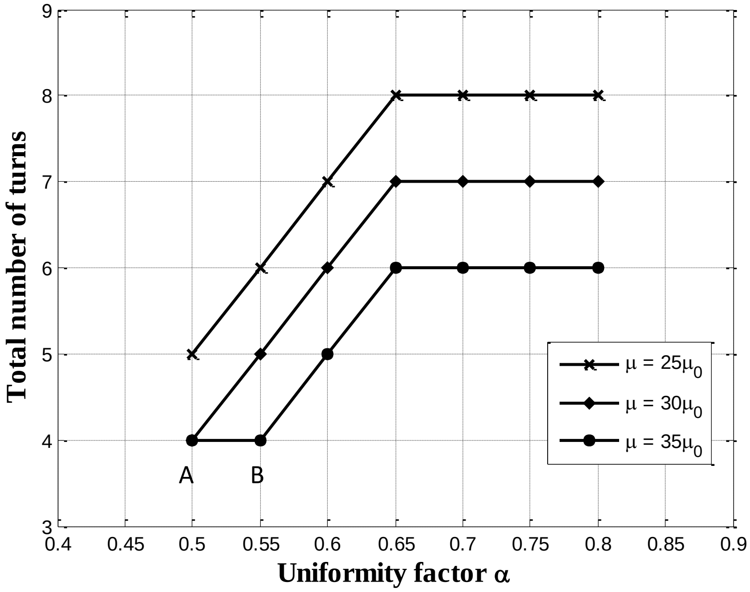

Figure 3.7. Plots of total number of turns against uniformity factor at different relative permeabilities for R_c = 5 mm, H_c = 2 mm, B_{max} = 0.35 T, and specified current rating I_r = 10 A.

3.2.2 Effect of Maximum Flux Density B_{max}

Saturation is another property of the magnetic core material. A magnetic material is saturated the magnetic flux density (B) no longer increases proportionally with increasing magnetic field (H) [22]. The flux density (B) divided by the magnetic field (H) gives the effective permeability:

$$\mu = B / H \tag{3.3}$$

When the magnitude of magnetic field H exceeds the maximum limit, the B-H curve levels off to a slop of the vacuum permeability μ_o.

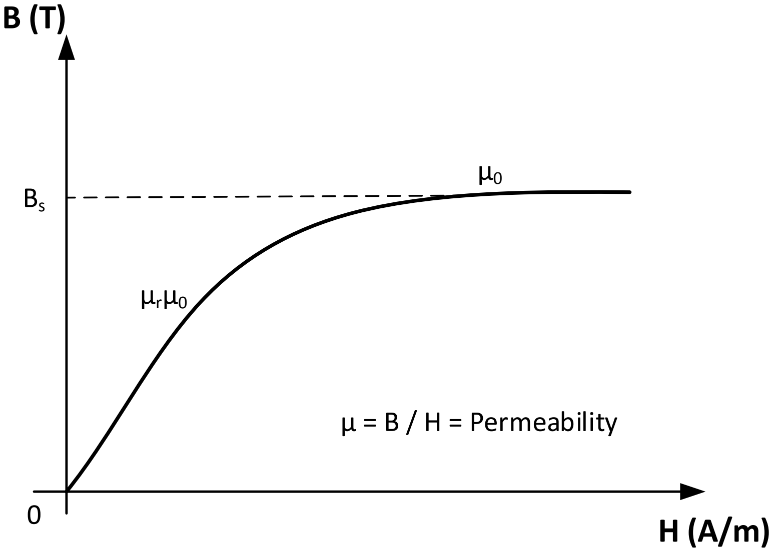

Figure 3.8. B-H curve of magnetic material showing the saturation flux density.

For the design of constant-flux inductor, the maximum magnetic flux density B_{max} can be determined from the material's magnetic property. If the B_{max} is smaller than the saturation flux density, the core is kept away from saturation. The magnetic field is regulated to allow the flux density to drop from the maximum value B_{max} to a minimum value αB_{max}; therefore, the constant-flux distribution is achieved.

As shown in Figure 3.6, B_{max} is swept from 0.1 T-0.35 T under different permeabilities, and it has no effect on the time constant. However, B_{max} affects the number of turns in each winding window by changing the ampere-turns that the winding window carries. Rewriting equation (3.2), the number of turns in winding window j can be expressed by

$$n_j = \frac{AT_j}{I_r} = \frac{B_{\max}}{I_r}\left[H_w \cdot \left(\frac{1}{\mu} \pm \frac{\alpha}{\mu}\right) + 2 \cdot \frac{1}{\mu} \cdot R_{Ij} \cdot \ln\left(\frac{R_{Oj}}{R_{Ij}}\right) \right] \tag{3.4}$$

where the items in the brackets are the ones that remains constant, and n_j is proportional to the maximum flux density B_{max}. Figure 3.9 shows the relationship between the number of turns and the maximum flux density at a relative permeability of 25 with a specified current rating of 10 A. As can be observed from the figure, when the B_{max} is larger, there are more turns in the winding windows.

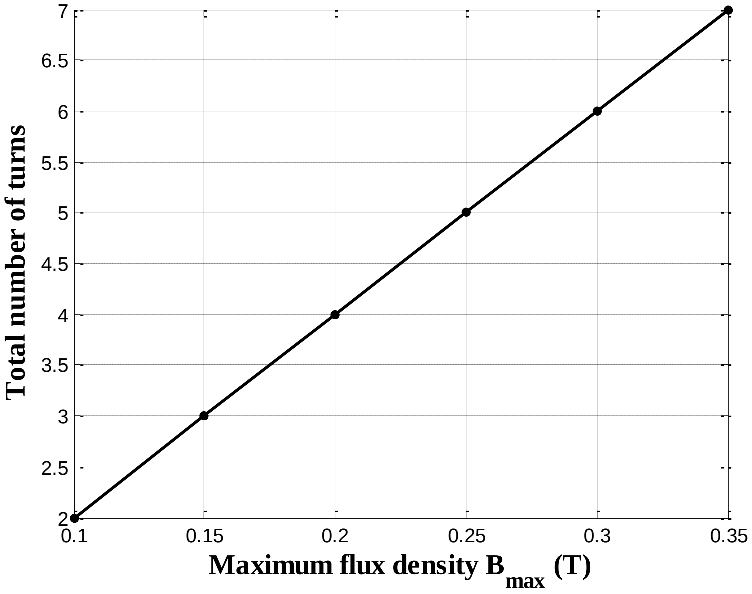

Figure 3.9. Plot of number of turns against maximum flux density B_{max} for R_c = 5 mm, H_c = 2 mm, $\mu = 25\mu_o$, and optimal α = 0.6.

3.3 Current, Inductance, Resistance

Selecting the uniformity factor α that gives the highest time constant is a good choice for the design; therefore, the winding structure is determined to have the best performance of the inductor. The time constant can lead to various combinations of inductance and resistance, depending on the total number of turns inside the inductor. This section shows the general relationship among the permeability, current, inductance, and resistance.

For a given B_{max} and uniformity factor α, the energy stored in the core volume is related to the permeability by

$$E = \frac{1}{2\mu} \cdot (\frac{B_{\max} + \alpha B_{\max}}{2})^2 \cdot V \tag{3.5}$$

The energy is also related to the inductance and current rating by

$$E = \frac{1}{2} L I_r^{\ 2} \tag{3.6}$$

Equation (3.5) suggests that the total energy increases with decreasing permeability, resulting in an increase in inductance L for a given current rating I_r according to (3.6). Figure 3.10 gives an example of the relationship between dc resistance and inductance at different current ratings and relative permeabilities. Along each curve, the current rating is fixed while the relative permeability is swept from 20 to 30. A decrease in either permeability or current rating will increase the number of turns that each winding window represents in order to maintain the maximum flux density B_{max}, as suggested by (3.2). Therefore, the inductance and the resistance increase. Figure 3.11 shows the relationship between dc resistance and inductance at different maximum flux densities B_{max} and relative permeabilities when keeping the current rating at 10 A.

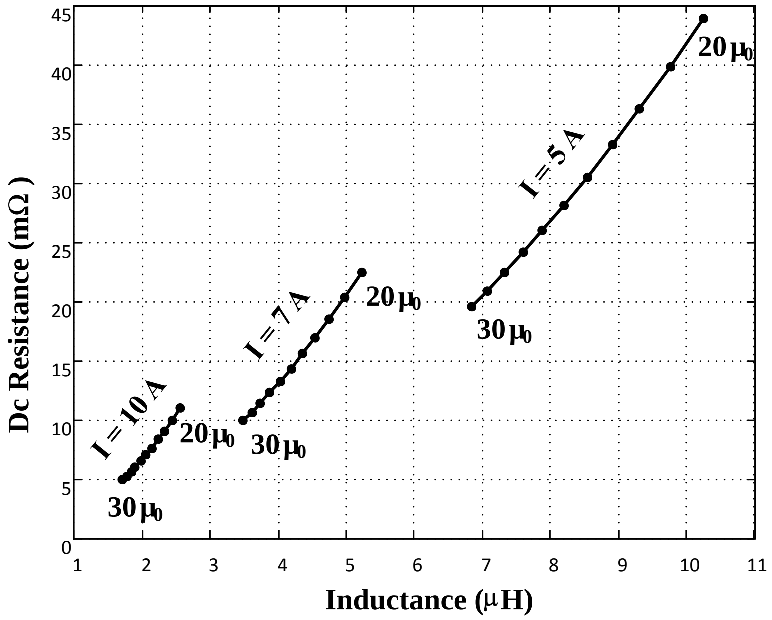

Figure 3.10. Relationships among permeability, dc resistance, and inductance at different current ratings for R_c = 5 mm, H_c = 2 mm, B_{max} = 0.35 T, and uniformity factor α = 0.6.

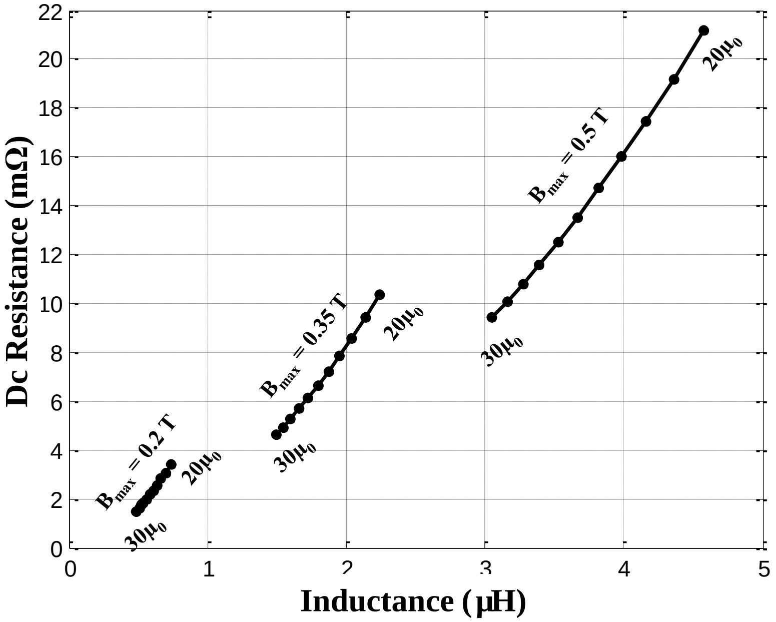

Figure 3.11. Relationships among permeability, dc resistance, and inductance at different maximum flux density for R_c = 5 mm, H_c = 2 mm, I_r = 10 A, and uniformity factor α = 0.6.

3.4 Simulation Verification

First of all, the uniformity level of the resulting design is to be verified. A 2D finite element analysis (FEA) using Maxwell software was performed to simulate the designed structure of constant-flux inductor [49]. In the simulation, the ideal ampere-turns currents, such as the 52.6 A, 23.7 A, and 15.3 A listed in Table IV, for each winding window were applied to each conductor. The simulated results of the total energy in the magnetic material and the total dc winding loss on the conductor were recorded to calculate the time constant by using equation (2.20).

For each specified uniformity factor α, the radii of all the winding windows as well as all the other dimensions can be obtained from the field equations (2.2)-(2.5). Therefore, the structure of each constant-flux inductor under different uniformity factors can be constructed in Maxwell. From the color maps of the flux density distribution shown in Figure 3.12, it can be seen that the simulation results of the uniformity level of the flux density distribution is consistent with the selection of the uniformity factor α. The larger the value α the more uniform the magnetic field.

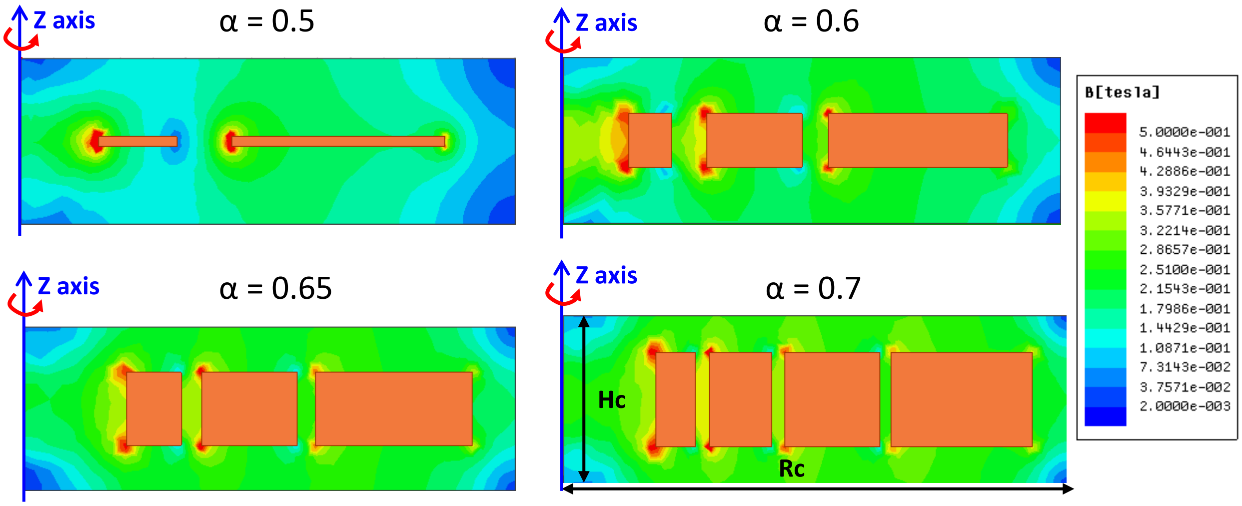

Figure 3.12. 2D FEA simulation results of the designed constant-flux inductors with uniformity factors α = 0.5, 0.6, 0.65, and 0.7 for a design with R_c = 5 mm, H_c = 2 mm, and $\mu = 35\mu_0$.

To verify the accuracy of the analytical model of constant-flux inductor, three cases with different footprints and thicknesses were simulated in Maxwell, and are listed in Table VIII. The dimensions of the inductor designed in Cases 1, 2, 3 are shown in Figure 3.3.

TABLE VIII SIMULATION CONDITIONS FOR CONSTANT-FLUX INDUCTOR DESIGNED

	R_c (mm)	**H_c (mm)**	**μ**	**B_{max} (T)**	**α**
Case 1	5	2	$35\mu_o$	0.35	0.6-0.75
Case 2	3	1	$35\mu_o$	0.35	0.5-0.75
Case 3	3	1	$60\mu_o$	0.35	0.55-0.75

Figure 3.13 shows the calculated results of time constant of Case 1 by using 2D FEA tool and the analytical model. The resistance from the simulation match the calculation result with a maximal error of 8.5%, but the inductance has some discrepancy with the calculation result. The difference is caused by the energy stored at the corner areas of the constant-flux inductor. In the calculation model, the energy stored at the corners are neglected, which is close to the simulation under small uniformity factor. However, as the uniformity factor increases, the energy stored in the corners increases, as shown in Figure 3.12. Therefore, the simulated inductance is higher than that from the calculation.

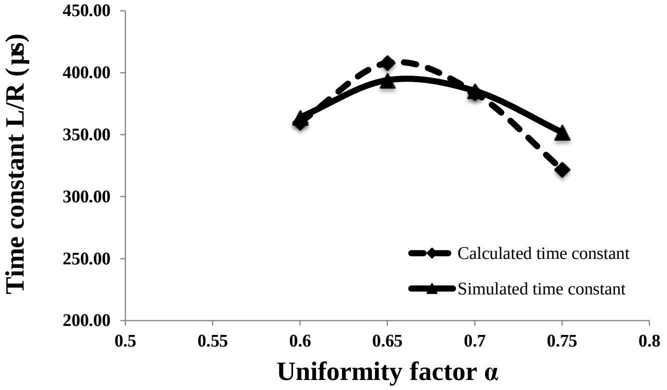

(a)

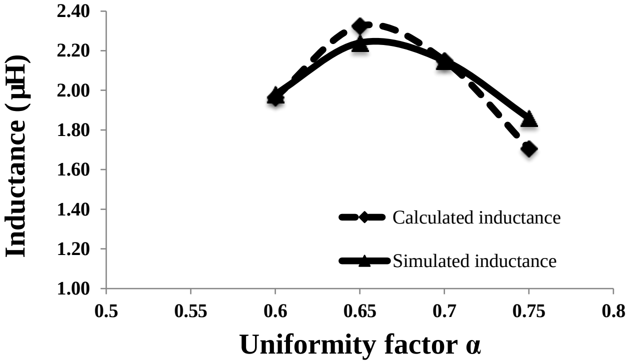

(b)

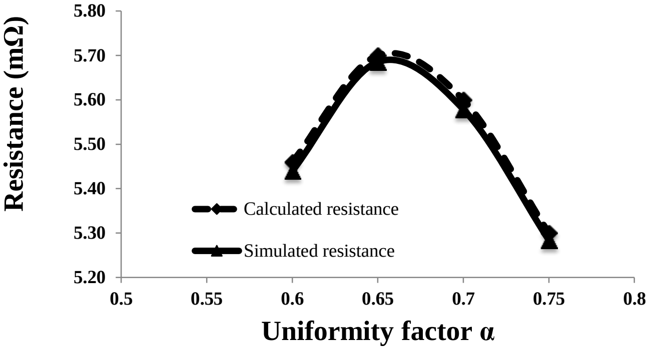

(c)

Figure 3.13. Results of (a) time constant versus uniformity factor α, (b) inductance versus uniformity factor, and (c) resistance versus uniformity factor obtained by using 2D FEA simulation model (solid line) and analytical model (dash line) for a design of constant-flux inductor structure with R_c = 5 mm, H_c = 2 mm, and $\mu = 35\mu_0$.

Figure 3.14 shows the calculated results of time constant of Case 2 by using 2D FEA tool and the analytical model. Figure 3.13 and Figure 3.14 show the inductor designed for different footprints and inductor heights, the results of the analytical model also match those of the 2D FEA model with a maximal error less than 10%.

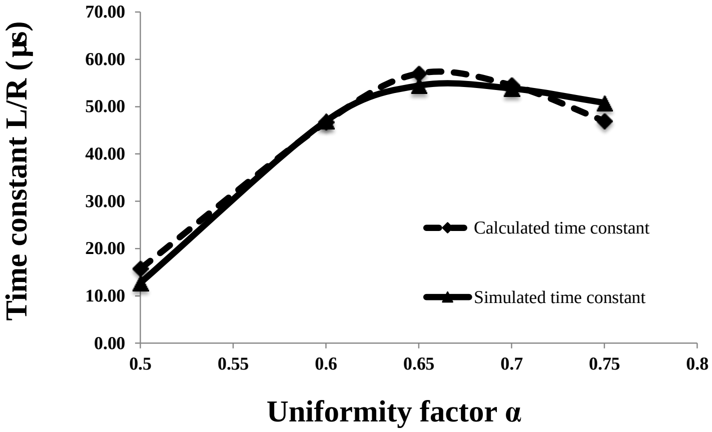

Figure 3.14. Results of time constant versus uniformity factor α obtained by using 2D FEA simulation model (solid line) and analytical model (dash line) for a design of constant-flux inductor structure with R_c = 3 mm, H_c = 1 mm, and $\mu = 35\mu_0$.

Case 3 was performed to validate the time constant calculated from the analytical model under different permeabilities. As mentioned earlier in this chapter, changing the permeability does not affect the distribution of the winding windows. As Figure 3.15 suggests, the radii of each winding window remain the same at $\mu = 60\mu_0$ and $\mu = 35\mu_0$, and the flux distribution remains the same to keep the maximum flux density B_{max} at 0.35 T.

Figure 3.16 gives the calculated results of the time constant of Case 3 inductor with a higher permeability than that of Case 2 inductor. A comparison of Figure 3.14 and Figure 3.16 shows that the time constant increases with increasing permeability.

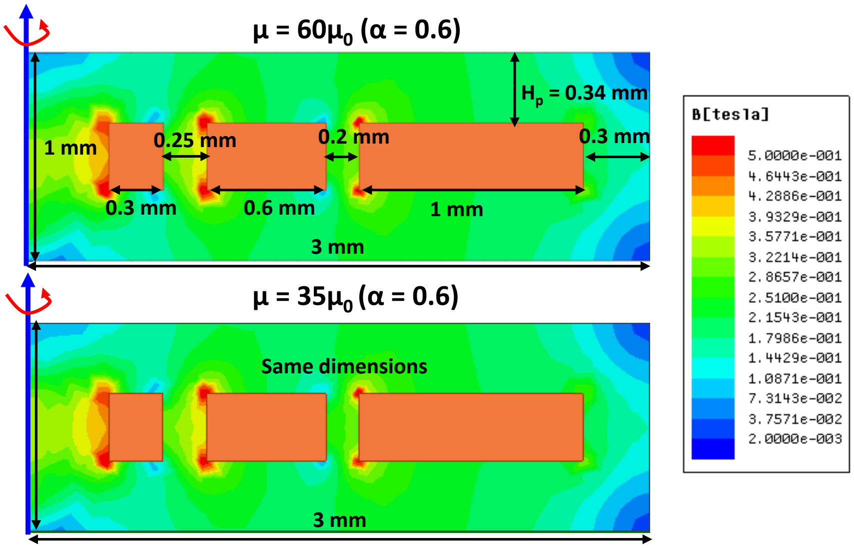

Figure 3.15. 2D FEA simulation result of the designed constant-flux inductors with different permeabilities of 35μ_o and 60μ_o and uniformity factor of 0.6 for a design with R_c = 3 mm and H_c = 1 mm.

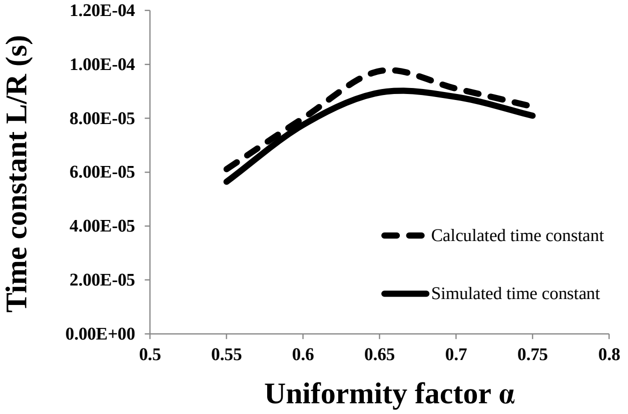

Figure 3.16. Results of time constant versus uniformity factor α obtained by using 2D FEA simulation model (solid line) and analytical model (dash line) for a design of constant-flux inductor structure with R_c = 3 mm, H_c = 1 mm, and $\mu = 60\mu_o$.

The maximum error between the time constants calculated from the 2D FEA simulation and the parametric study for each case is listed in Table IX. The maximum error of less than 10% for all cases validates the parametric study results of the constant-flux inductors.

TABLE IX MAXIMUM ERRORS OF TIME CONSTANTS BETWEEN CALCULATION AND ANALYTICAL MODEL

	Case 1	**Case 2**	**Case 3**
Maximum error (%)	8.5	7.5	8.9

3.5 Comparison with Commercial Products

The objective of the constant-flux inductor design is to obtain the optimal value of the time constant for a given volume. Therefore, the factor time-constant-density is defined to include the factor of volume. The higher the time-constant-density is, the higher the ratio of inductance to resistance is for a given volume. In the following sub-sections, the time-constant-density obtained for a constant-flux inductor is compared with that for a commercial product. For the same volume of constant-flux inductor and commercial inductor, the inductance and resistance are calculated for both inductors to show the benefit of the higher time-constant-density of the constant-flux inductor than that of the commercial product. On the other hand, at the same inductance and resistance, the volume is smaller for the constant-flux inductor than for the commercial product.

3.5.1 Comparison of Time-Constant-Density

For most commercial surface-mount inductors, the datasheet always provides a wide range of choices with different values of inductance, resistance and package size [23]. Table X compares the electrical and mechanical parameters from the commercial products of manufactures like SSM [13], Maglayers [12], Vishay [24], and Bourns [25] with those from constant-flux inductors. The package volume was selected to be as close to $5 \times 5 \times 3$ mm^3 as possible, which equals the volume of the constant-flux inductor designed. For each commercial inductor, the corresponding inductance and resistance with the highest time constant are selected from each series. The time-constant-density can be calculated as

$$\tau_v = \frac{L}{R_{dc} \cdot V} \tag{3.7}$$

where L is the inductance read from the datasheet, R_{dc} is the typical value of dc resistance from the datasheet, and V is the total package volume of the commercial product.

TABLE X COMPARISON OF ELECTRICAL AND MECHANICAL PARAMETERS OF CFI AND COMMERCIAL PRODUCTS

Manufacturer	Volume (mm^3)	L (μH)	R_{dc} (mΩ)	τ/V (s/m^3)
SSM [13]	5.2 × 4.7 × 3	1.2	15	1091
Maglayers [12]	5 × 4.7 × 3	3.3	32	1463
Vishay [24]	5.18 × 5.49 × 2	1.0	18.9	930
Bourns [25]	4.8 × 4.8 × 2	1.0	21.6	1005
CFI α = 0.6	5 × 5 × 3	1.0	3.3	4077
CFI α = 0.65	5 × 5 × 3	1.0	3.4	4008
CFI α = 0.75	5 × 5 × 3	1.0	4.1	3319

The bar chart in Figure 3.17 shows part of the data listed in Table X in comparing the time constant densities of the CFI with variable uniformity factor and the commercial products. The constant-flux inductor with a uniformity factor of 0.6 has the highest time-constant-density of all the inductors. All the constant-flux inductors designed have significantly higher time-constant-density than the commercial products at the same package volume. Owing to the uniform magnetic flux distribution, the utilization of the magnetic material is improved greatly, leading to an increase in time constant.

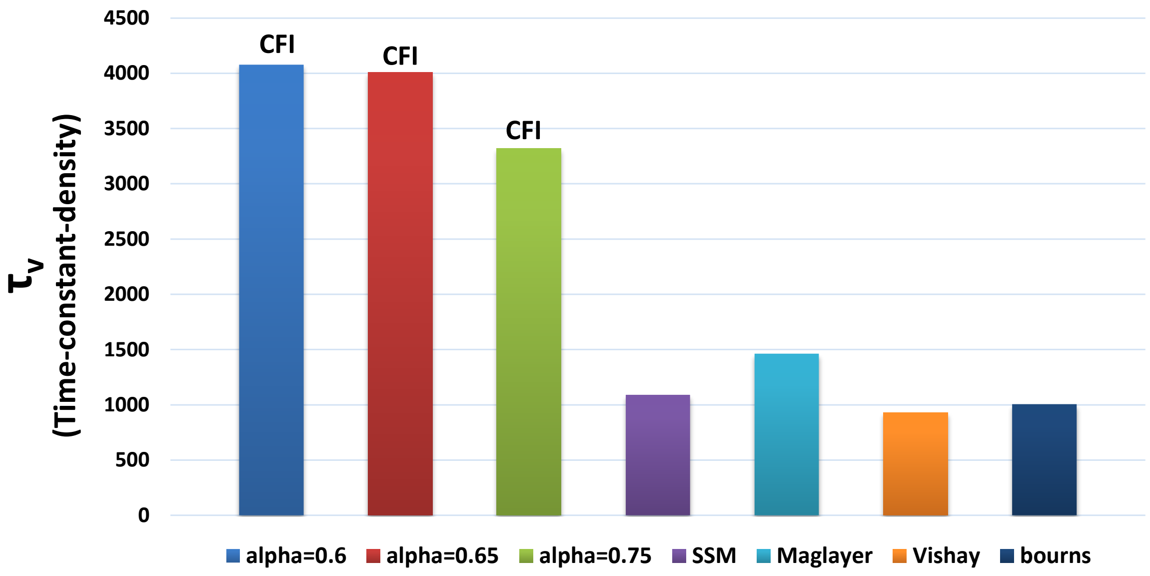

Figure 3.17. Calculated results of time-constant-density of constant-flux inductors and commercial products with R_c = 2.5 mm, H_c = 3 mm, and $\mu = 35\mu_0$.

3.5.2 Comparison of Inductance and Resistance at Constant Volume

To compare the performance of the constant-flux inductors with the commercial products in a more intuitive way, the inductance and resistance values are calculated based on different current ratings. Once the uniformity factor and the magnetic material's properties are specified, the structure is determined, and the current rating would not change the time constant. As Figure 3.10 suggests, when the current rating is higher, both the inductance and the resistance have to be smaller to make fewer turns in each winding window. For a given current rating, the actual inductance and resistance can be calculated through equation (2.10)-(2.15) in a sweeping process. Figure 3.18 shows the results of sweeping the current from 0.5 A to 4 A for the constant-flux inductor designed with a footprint of 2 × 2 mm^2 and a thickness of 1 mm. The inductance of the constant-flux inductor is about the same as that of the commercial inductors from Vishay [24] for the specified current rating. However, the resistance of the constant-flux inductor is much lower than that of the Vishay inductors. Compared with the inductor with comparable footprint and thickness from TDK [26], the constant-flux inductor has a higher inductance, but about the same resistance.

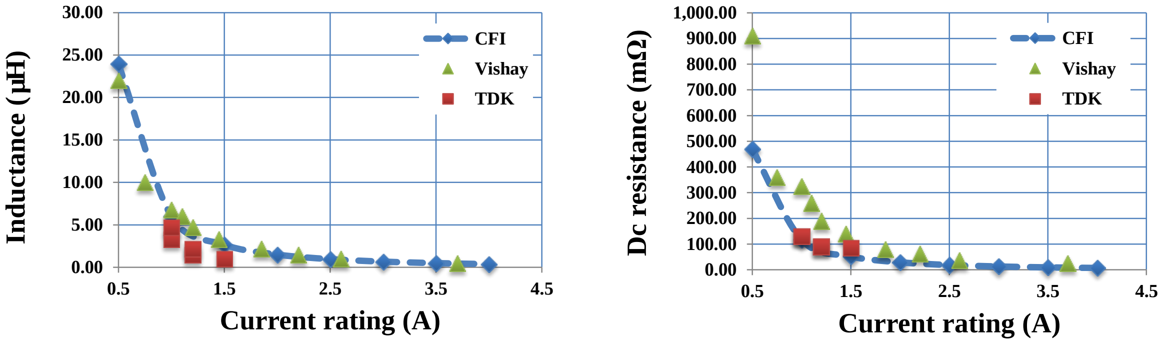

(a) (b)

Figure 3.18. Comparison of (a) inductance and (b) resistance between constant flux inductor and commercial products from Vishay [24] and TDK [26] with $R_c = 1$ mm, $H_c = 1$ mm, $\mu = 35\mu_o$, $B_{max} = 0.5$ T, and $\alpha = 0.65$.

3.5.3 Comparison of Volume at Constant Inductance and Resistance

The effect of an increase in time-constant-density can be interpreted in another way: for the same inductance and resistance value, the volume of the constant-flux inductor can be greatly reduced. An example design of constant-flux inductor shows that the total thickness can be reduced from 4 mm to 2 mm with the same footprint area 10 mm × 10 mm as a commercial inductor [19]. Figure 3.19 compares the results of inductance and resistance of the constant-flux inductor with those of the commercial inductor. For the constant-flux inductor, the uniformity factor is selected at the peak value, the permeability is 35 μ_o, and the maximum flux density is 0.6 T. The inductance and the resistance of the constant-flux inductor are almost the same as those of the Maglayers inductors; however, the total volume of the constant-flux inductor is only half of that of the commercial inductor.

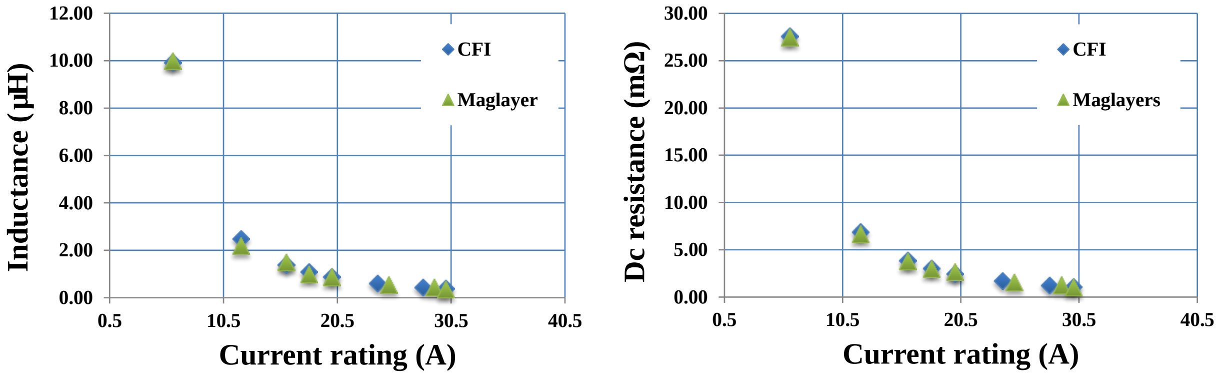

(a) (b)

Figure 3.19. Comparison of (a) inductance and (b) resistance between constant flux inductor ($\mu = 35\mu_o$, $B_{max} = 0.6$ T, and $\alpha = 0.6$ within a volume of $10 \times 10 \times 2$ mm^3) and commercial products from Maglayers [19] with twice the volume ($10 \times 10 \times 4$ mm^3).

Chapter 4 Fabrication Methods for Constant-Flux Inductor

This chapter gives a discussion on the fabrication methods and measurement results of the constant-flux inductor designed. To fabricate the structure from the design procedure introduced in previous chapters, various fabrication methods for the core and the winding are proposed in Table XI and Table XIII. Among the methods proposed for the core fabrication, laser ablation for the LTCC tape and routing for the powder iron plain core were implemented in the experiments. Table XI gives a detailed description of the advantages and drawbacks of these two methods, as well as the mechanical limitations of the experiments. Table XIII includes the possible ways to fabricate the winding part, using either copper or silver paste as the winding material. The routing method currently turns out to be the best choice for winding prototyping owing to the high controllability in dimensions. Table XVI shows the result obtained by different combined methods for the core and winding.

Section 4.1 discusses the routing method for powder iron material and the laser ablation technique for LTCC tape in detail, with the use of the design of experiments (DOE) method to control the laser ablation depth (see Appendix A). Section 4.2 gives a detailed description of the two winding fabrication methods that have been evaluated in the experiments. Section 4.3 gives the measurement results of the assembled inductor prototypes made from different combinations of fabrication methods for the core and winding.

4.1 Core Fabrication

There are various selections of the material and various fabrication methods to make the core. Table XI lists several possible methods to fabricate the core by using low temperature co-fired ceramic (LTCC), powder iron core, or ferrite. These methods listed in Table XI are for prototyping purpose, and the methods listed in Table XII are the ones that are employed in mass manufacturing. Three of the prototyping methods were experimented in the lab, based on the availability of manufacturing equipment: (1) Routing method with the powder iron core, (2) routing method with the laminated LTCC ferrite tape, and (3) laser ablation with the laminated LTCC ferrite tape. Section 4.1.1 to 4.1.3 discuss them in detail.

TABLE XI AVAILABLE METHODS FOR CORE PROTOTYING IN LAB

Materials	**Laser ablation**	**Routing**	**Water jet cutting**
LTCC tape	• Minimum width: 0.2 mm • Inductance validated: 2.6 μH • Robust structure • Shrinkage problem	• Minimum width: 0.2 mm • Inductance validated: 1.8 μH • Flat surface • Shrinkage problem	Viable, but not tried yet
Powder iron core	Viable, but not tried yet	• No shrinkage • Cracks on wall • Inductance validated: 1.5 μH • Minimum width: 0.2 mm	Viable, but not tried yet

TABLE XII AVAILABLE METHODS FOR CORE FABRICATION IN MASS MANUFACTURING

Materials	**Injection molding**
LTCC powder	[29], [30]
Powder iron core	[19], [23], [24], [26]

4.1.1 Routing of Micrometals No. -8 Plain Core

Iron powder is a common magnetic material for making inductors. The plain core from Micrometals [27] is selected as a candidate to fabricate a prototype of the constant-flux inductor. Among the various selections of the material with different mix numbers, No. -8 plain core was used for the fabrication. The B-H curve shown in Figure 4.1 suggests that the maximum flux density of the material No. -8 is 1.25 T.

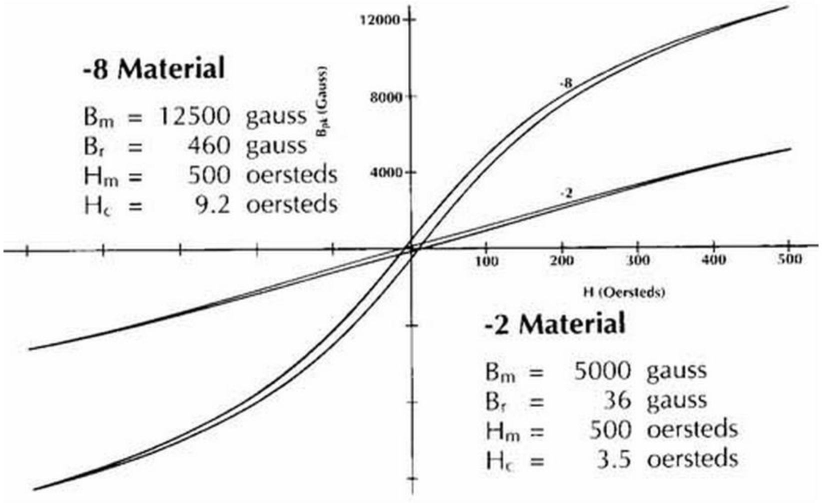

Figure 4.1. B-H curves provided by Micrometals of material mix No. -8 [27].

To determine the permeability of the iron powder, a toroid routed from Micrometals No. -8 plain core was made for inductance testing, as shown in Figure 4.2. The number of turns on the toroid was 19 and the inductance measured was 780 nH. The relative permeability of this material was calculated from

$$L = \frac{\mu N^2 h}{2\pi}\ln(\frac{OD}{ID}) \tag{3.8}$$

where OD and ID are the outer and inner radii of the toroid, h is the height of the toroid, and N is the number of turns. The permeability μ is found to be $22\mu_o$.

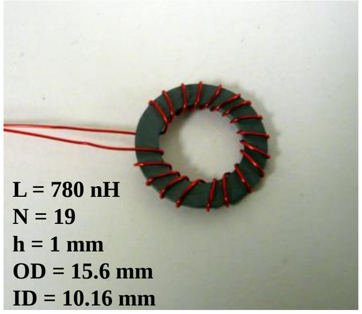

Figure 4.2. Toroid core made from Micrometal No. -8 plain core to measure the relative permeability.

As shown in Figure 4.3(a), a cylinder plain core was sliced into 1-mm-thick disks in order to fabricate a core half. The core disk (see Figure 4.3(b)) was bonded to a printed-circuit board by using cyanoacrylate to stabilize the core during the routing process. The winding groove in each core half was routed by a T-Tech QC-5000 prototyping machine using a 15-mil square end-mill bit. The empirical settings of the prototyping machine for 1-mm-thick core disk are a spindle speed of 15000 rounds-per-minute and a routing velocity of two inches per minute. After routing, the core was released by soaking in acetone for half an hour.

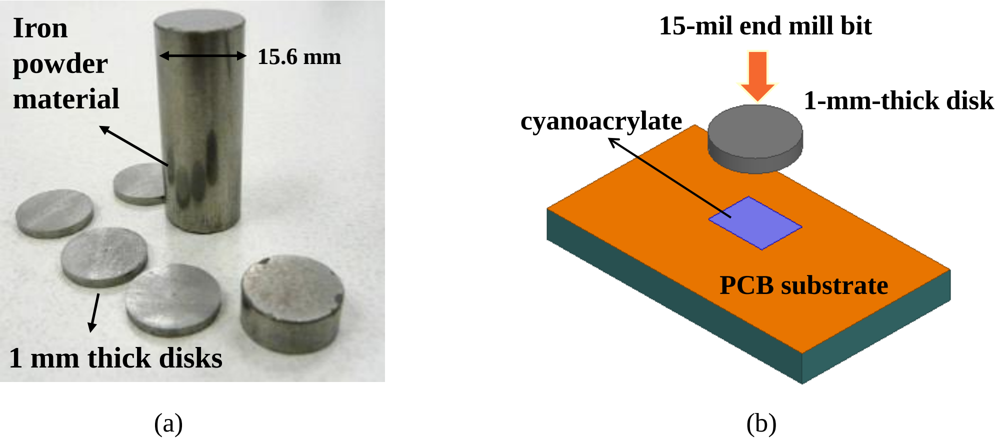

Figure 4.3. (a) Plain core and core disks; (b) preparation for the routing process.

The constant-flux inductor designed in section 2.5.1 and 2.5.2 is used for fabrication. The drawing of a core half is shown in Figure 4.4 (a) with the dimensions listed in Table V. Since the iron powder does not require sintering, the dimensions can be controlled precisely throughout the process. The prototyping machine gives a pattern with exactly the same dimensions as the design structure, and the minimum width of the grooves can be as small as 0.2 mm. Figure 4.4 shows the prototype of the core made by the routing method. No error in dimension is introduced from the fabrication.

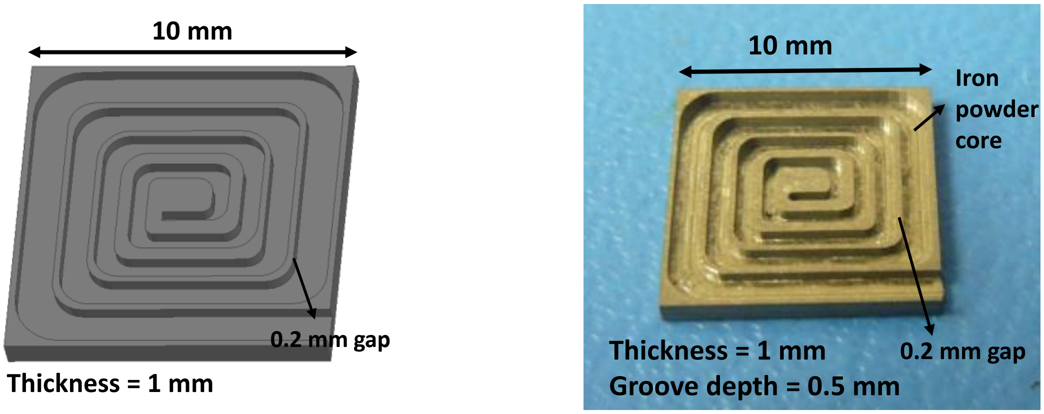

(a) (b)

Figure 4.4. (a) Drawing of designed core structure obtained by FEA simulation software with dimensions listed in Table V; (b) core prototype made by routing process using Micrometals No. -8 plain core with 10 mm × 10 mm footprint and 1 mm thickness.

4.1.2 Routing of LTCC Green Tape

The low-temperature co-fired ceramic (LTCC) is another suitable material for high current applications [28]. In the LTCC fabrication process, the green tape of LTCC ferrite was laminated by the model 2112 laminating press from Carver under 1500 psi and 80 ℃ for 15 minutes. After the lamination, the LTCC stack shown in Figure 4.5(a) was connected to the substrate shown in

Figure 4.3(b) and routed by the T-Tech QC-5000 prototyping machine using a 15-mil square end mill bit according to the same procedure introduced in the last section, with the same target dimensions listed in Table V of the constant-flux inductor designed. The unsintered LTCC core half after routing is shown in Figure 4.5(b). The dimensions for routing were increased by 20% to account for the 20% shrinkage after sintering.

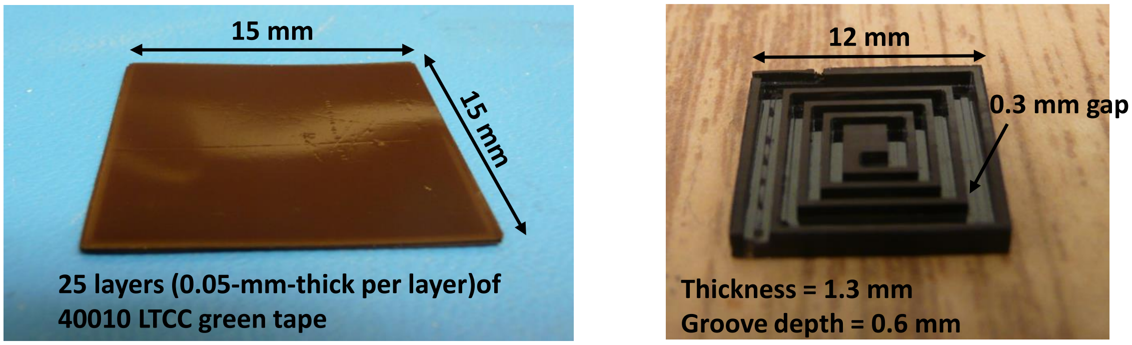

(a)

(b)

Figure 4.5. (a) Laminated LTCC stack before routing; (b) unsintered LTCC stack after routing with dimensions 20% larger than the ones listed in Table V.

Considering the complexity and asymmetric structure of a core half of a constant-flux inductor, the sinter profile should be controlled precisely to prevent cracking on the grooves or the warping on the core half. Since the two core halves are connected face-to-face on the inner side, either the cracking or the warping problem would introduce a significant air gap between the two core halves, and reduce the effective permeability and inductance.

In the case of sintering the LTCC core half routed, the sintering profile suggested in the datasheet from ESL [28] results in severe warping on the core halves, as shown in Figure 4.7(a). The warping of samples after sintering could be due to particle sedimentation during casting and/or drying [32], [34]. Therefore, the sintering profile is modified with a much lower rate of temperature increase and cooling speed to prevent cracking or warping caused by the large change in temperature. Figure 4.6(b) shows the sintering profile after modification. The rate of temperature increase is reduced from 2 ℃ per minute to 0.5 ℃ per minute, and the cooling speed is reduced from -5 ℃ per minute to -0.5 ℃ per minute. Figure 4.7(b) shows two core halves with no warping, the benefit of the modified sintering profile, which minimizes the undesirable spacing between the two core halves.

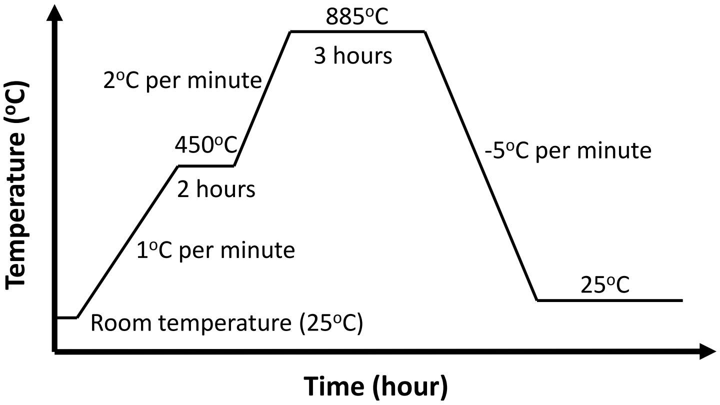

(a)

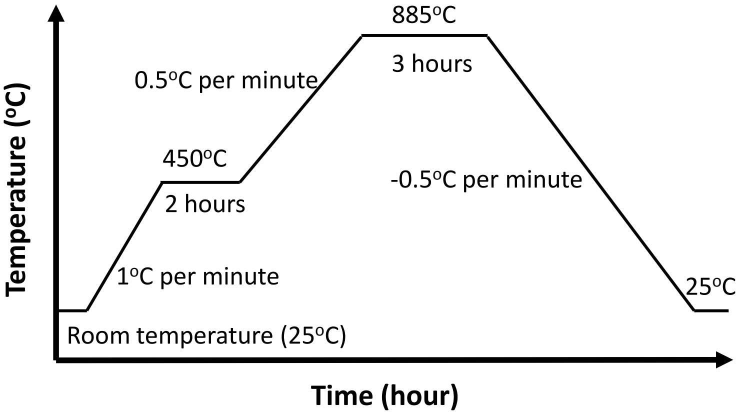

(b)

Figure 4.6. (a) Sintering profile suggested in the datasheet of the LTCC green tape from ESL [28]; (b) modified sintering profile with lower rate of temperature increase and cooling rate.

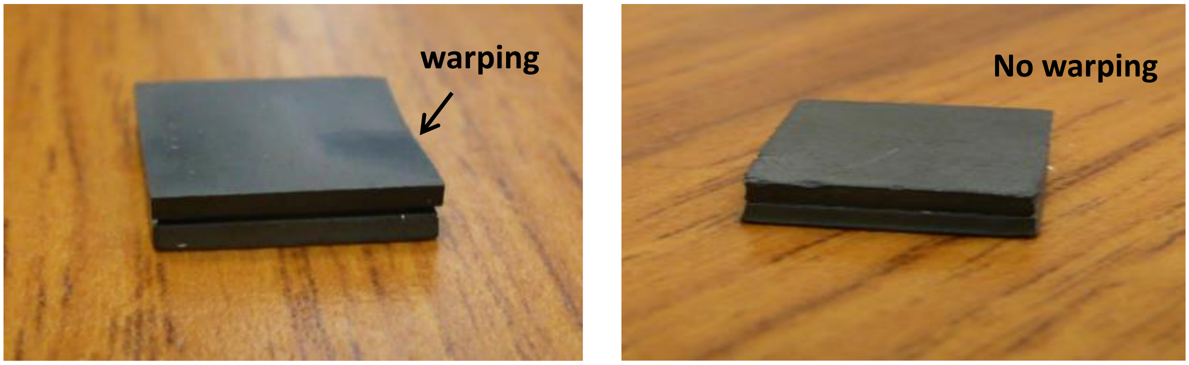

(a) (b)

Figure 4.7. Two core halves in stack with (a) severe warping problem in the center and (b) flat surface and no warping problem.

Considering the 20% shrinkage on the dimensions of all directions, the structure used for routing on the LTCC core is enlarged by 20% than the original dimensions, as shown in Figure 4.8 (a). After sintering, the dimensions of the structure is shown in Figure 4.8 (b). The dimensions after shrinkage can be very close to the design result. However, an error of 15% exists between the measured dimension and the target dimension because of the uncontrollable shrinkage problem.

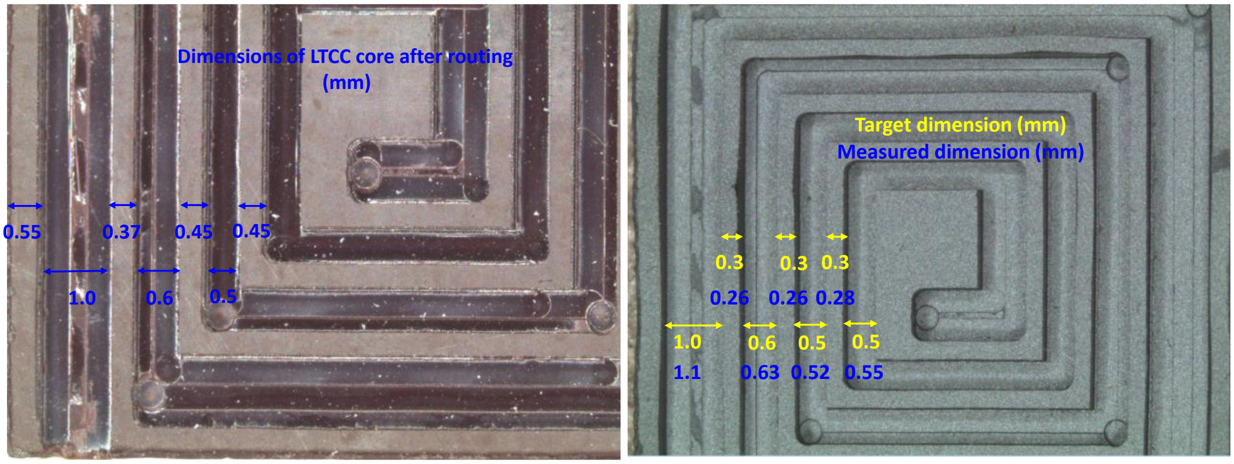

(a) (b)

Figure 4.8. Dimensions of (a) LTCC core after routing and (b) LTCC core after sintering.

4.1.3 Laser Ablation of LTCC Tape

The original laser technique, which requires lamination after the lasing, usually leads to poor pattern alignment, as shown in Figure 4.10(b). Evolved from the original process, the laser ablation method has the advantage of avoiding further lamination after the lasing; therefore, the pattern on the LTCC stack seems more smooth and neat. Instead of cutting all the way through, the laser beam only rubs out a certain depth of the LTCC stack, as shown in Figure 4.9(a). By following a user-defined lasing path, we can ablate off the winding area, or the cavity. Figure 4.9(b) shows the lasing path that was used in the laser machine to fabricate a core half. For each segment, the laser beam goes along a spiral path in order to improve the flatness of the ablated surface by distributing the heat evenly.

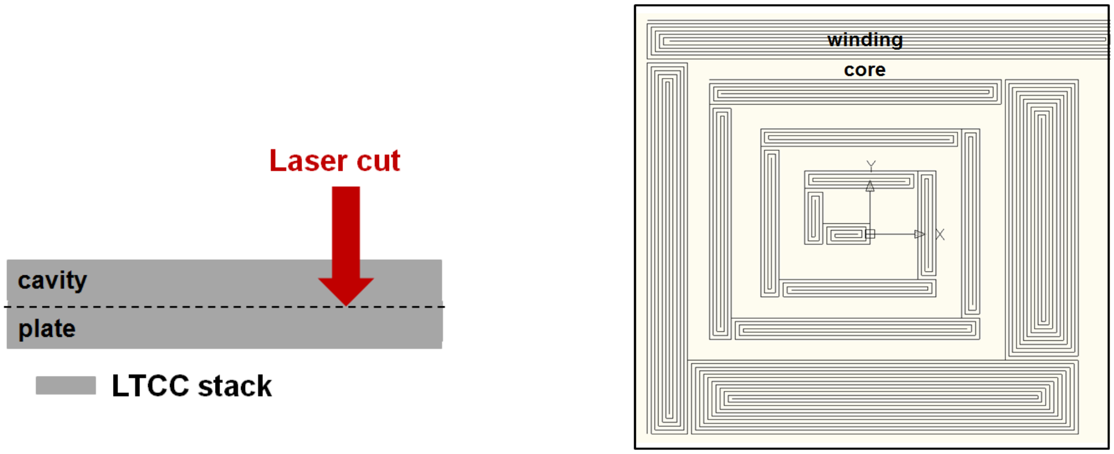

(a) (b)

Figure 4.9. Laser ablation method: (a) the laser power is calibrated to give the depth of the cavity and the thickness of the core half through the LTCC stack (see Appendix A); (b) spiral path of laser ablation to improve the surface flatness after ablation.

Figure 4.10 compares the results of the ablation process and the original laser technique. Since the lamination step is eliminated in the ablation method, the core half has better shape and alignment.

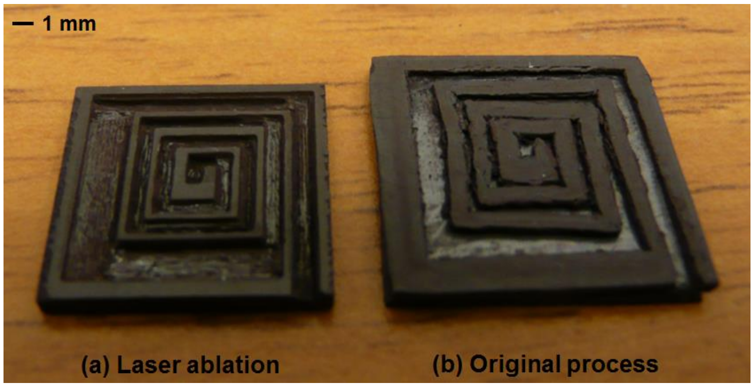

Figure 4.10. Comparison of the results after (a) laser ablation and (b) original process. The laser ablation method provides better control on the width of the edges because lamination after lasing is avoided.

The core half after laser ablation was placed into the box furnace to carry out the sintering process by following the sintering profile shown in Figure 4.6 (b). After sintering, the core half was cross-sectioned for dimension measuring as shown in Figure 4.11.

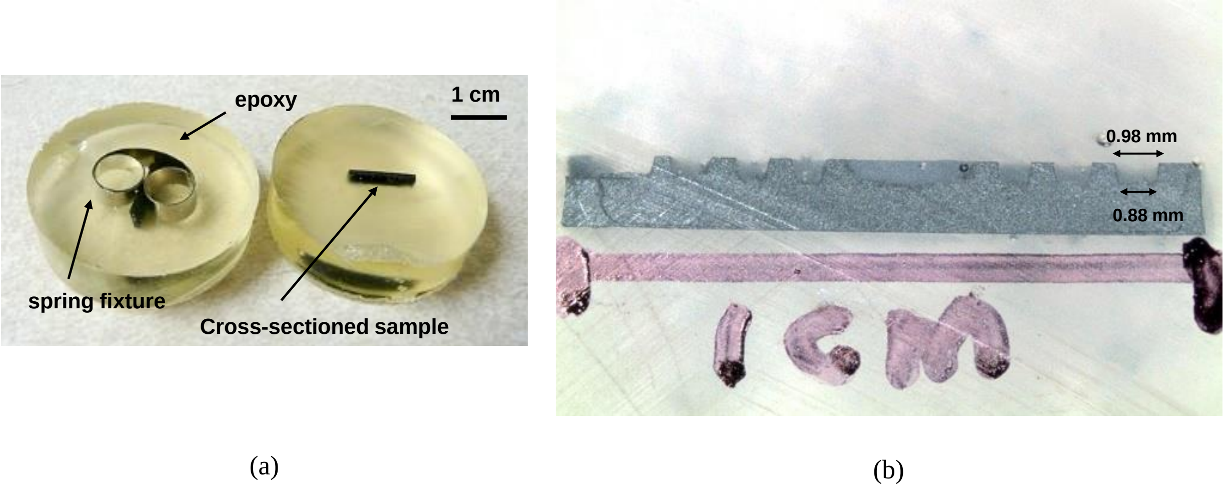

(a) (b)

Figure 4.11. Dimensions at the cross-sectional area of the core-half sample measured under microscope.

From Figure 4.11, the dimension measured at the top surface of the ablated area is 0.1 mm larger than the one at the bottom surface of the ablated area. The ramp at the cutting edge is caused by the focus setting of the lasing beam. When the focus is set to the target depth of 0.5 mm, the top surface is over-ablated and has a wider ablation area than the bottom, which forms the lasing loss.

Figure 4.12 compares the dimensions of the drawing of the target structure in AutoCAD, the ablated LTCC core half before sintering, and the LTCC core half after sintering. From Figure 4.12 (b), the width of each wall is in average 0.06 mm smaller than the one in Figure 4.12 (a), while the width of the cavity labeled in blue color is 0.06 mm larger than Figure 4.12 (a). This result is caused by the lasing loss, and it agrees with the one shown in Figure 4.11 since the dimension measured in Figure 4.12 under microscope is on the top surface. Figure 4.12 (c) shows the dimensions shrink by 20% after sintering, and the sintered result match the target dimensions.

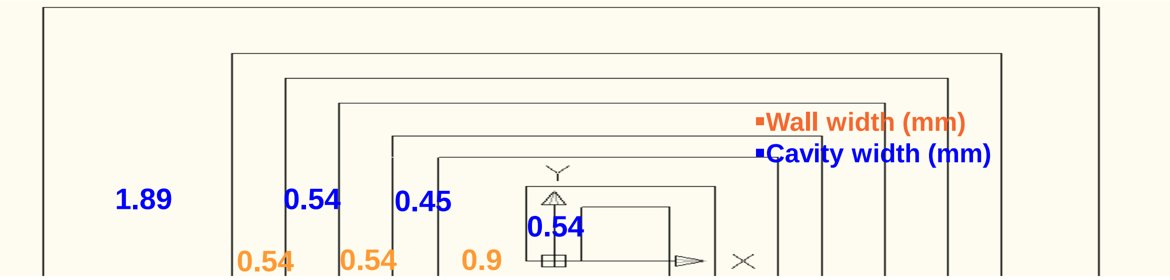

(a)

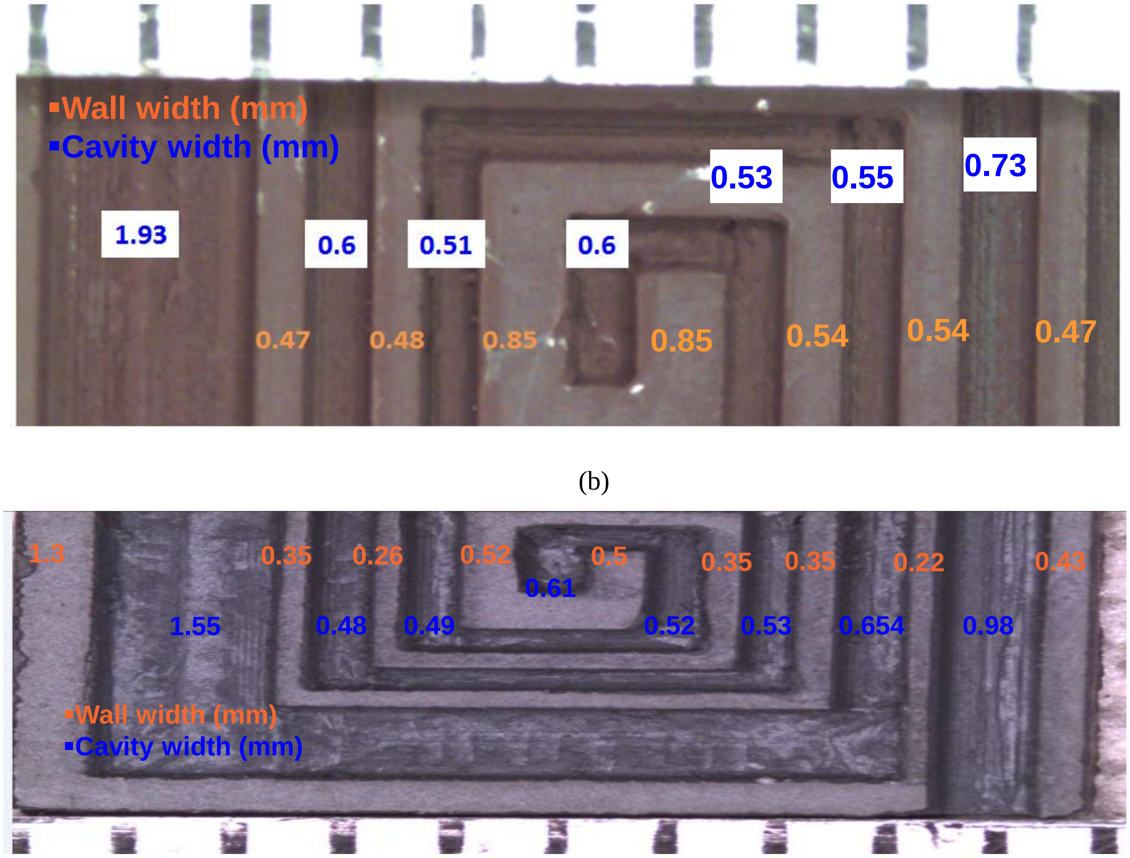

(b)

(c)

Figure 4.12. Dimensions of the width of the cavities and walls of (a) structure drawing in AutoCAD for laser ablation, (b) ablated LTCC core half before sintering showing lasing loss on the walls, and (c) sintered LTCC core half showing 20% shrinkage.

4.2 Winding Fabrication

There are various ways to make the planar winding for the constant-flux inductor [44]. Table XI presents several proposed methods to manufacture the winding by using either copper material or silver paste. Four possible ways to make the winding were experimented in the lab, based on the availability of manufacturing equipment: (1) routing method on copper sheet, (2) screen printing with silver paste, (3) etching with copper sheet, and 4) reverse electroplating with copper sheet. The routing method on copper sheet gives the best results. Etching and reverse electroplating fail to give successful results. Therefore, only the routing method and screen printing with silver paste are discussed in detail in this section.

TABLE XIII AVAILABLE METHODS FOR WINDING PROTOTYPING IN LAB

Materials	**Etching/ Reverse electroplating**	**Routing**	**Screen printing**
Copper (Cu) (or other metals)	• Large errors (50%) in dimensions • Poor repeatability	• Good dimension control • Minimum width: 0.3 mm	NA
Silver paste (Ag)	Viable, but not tried yet	Viable, but not tried yet	• High resistivity • Shrinkage in dimension

TABLE XIV AVAILABLE METHODS FOR WINDING FABRICATION IN MASS MANUFACTURING

Material	**Casting**	**Stamping**
Copper (Cu)	[32]	[31]

4.2.1 Routing of Copper Sheet

The constant-flux inductor designed was configured to have two layers of winding. One layer starts from the top terminal, spirals counterclockwise toward the center, connects to the bottom winding layer at the center, and spirals counterclockwise to the bottom terminal. The thickness of each layer inside the constant-flux inductor is 0.5 mm; therefore, a 0.5 mm thick copper sheet was used to fabricate the winding pattern according to the routing method.

Figure 4.13 shows the preparation procedure for the routing on copper sheet method. The copper sheet with a thickness of 0.5 mm was bonded to a printed-circuit board by using cyanoacrylate to stabilize the winding during the routing process. A hydraulic press was used to provide the pressure of 2000 psi needed to ensure that the attachment is even and flat. The spiral winding pattern in each layer was routed by a T-Tech QC-5000 prototyping machine using a 15-mil square end mill bit. After routing, the winding half was released by soaking in acetone for half an hour.

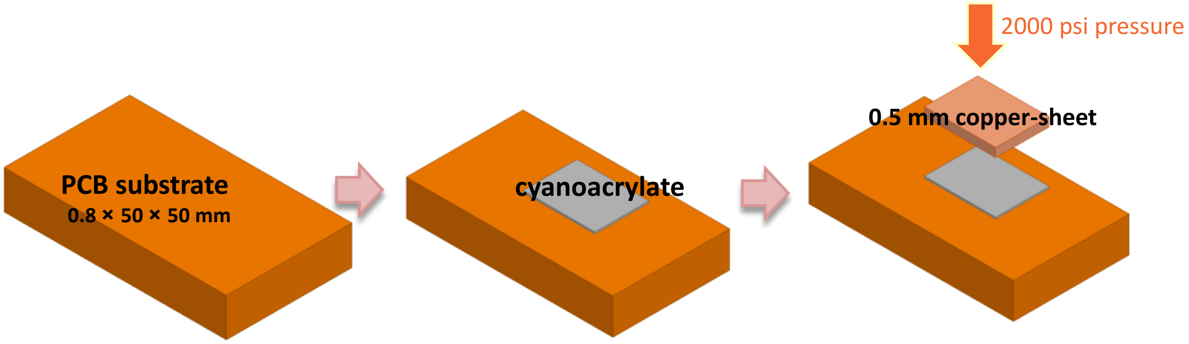

Figure 4.13. Preparation procedure for the routing method to fabricate the copper winding half.

The routing process needs to be repeated several times, since the milling bit is very brittle and can be damaged from improper routing speed or routing depth. The milling bit routes only a thin layer each time, and the whole process was repeated for up to six times until the routing path appears FR4 material to ensure that the copper sheet was cut through. The empirical settings of the prototyping machine for 0.5 mm thick copper sheet are a spindle speed of 17000 rounds-per-minute and a routing velocity of two inches per minute. Figure 4.14 shows the routing process and the routed winding half. The minimum width between the winding turns that can be manufactured depends on the routing material and the routing tool. Since the routing tool used in the lab is 15-mil milling bit, the minimum width between the copper turns that can be achieved is 0.38 mm, as listed in Table XV. The gap width routed between the winding turns is 0.2 mm larger than the design structure (see Table V) because it is limited by the diameter of the routing tool. However, it is necessary to have a larger gap than the design in order to make it easier to fit the copper winding into the core half afterwards. Therefore, the winding structure routed is 0.2 mm thinner on the width than the designed structure, and the resistance is expected to be 20% larger.

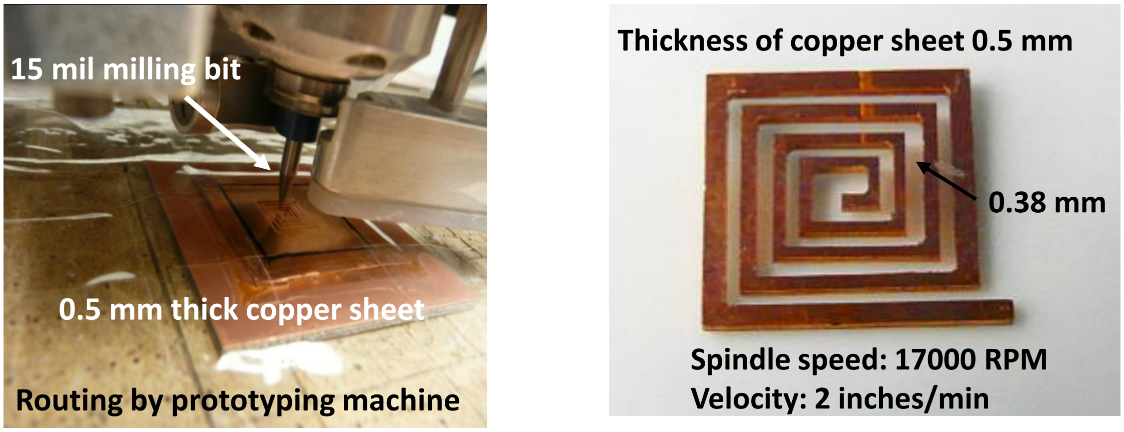

(a) (b)

Figure 4.14. (a) Routing process using T-Tech QC-5000 prototyping machine and 15-mil milling bit and (b) the routed winding half with four turns per layer spirally.

Table XV Parameter Settings for Routing Method with Copper Sheet

Spindle speed (rounds per min)	Velocity (inches/min)	Milling bit diameter (mil)	Minimum cutting width (mm)
15000-17000	2	15	0.38

4.2.2 Silver Paste

The routed copper winding is suitable for the iron powder core, since no sintering is needed for iron powder. For the LTCC core, silver paste is a recommended metallization material that can be co-sintered with the LTCC material purchased from DuPont [43].

The silver paste was screen printed to a sintered LTCC ferrite core half. The flow chart of the screen-printing process in shown in Figure 4.15. DuPont 7740 silver paste was applied to the sintered LTCC core, and was dried for one hour at 70°C. The dried inductor half with silver paste screen printed was sintered in the box furnace according to the modified sintering profile shown in Figure 4.6 to prevent inner cracking on the LTCC ferrite core.

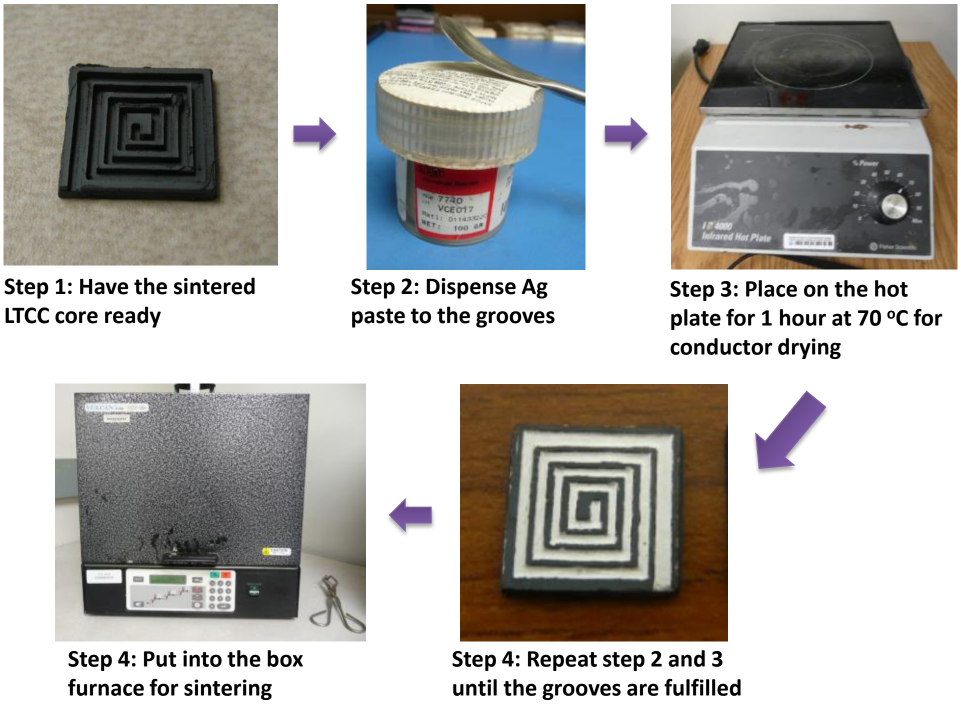

Step 1: Have the sintered LTCC core ready

Step 2: Dispense Ag paste to the grooves

Step 3: Place on the hot plate for 1 hour at 70 °C for conductor drying

Step 4: Repeat step 2 and 3 until the grooves are fulfilled

Step 4: Put into the box furnace for sintering

Figure 4.15. Flow chart of screen-printing process with silver paste DuPont 7740 [43].

Figure 4.16 shows a sintered inductor half with LTCC ferrite as the core and silver as the conductor. Two inductor halves were connected at the center by solder. A small amount of solder paste was deposited at the center of the winding halves. The two inductor halves were placed onto a reflow belt furnace for the solder process.

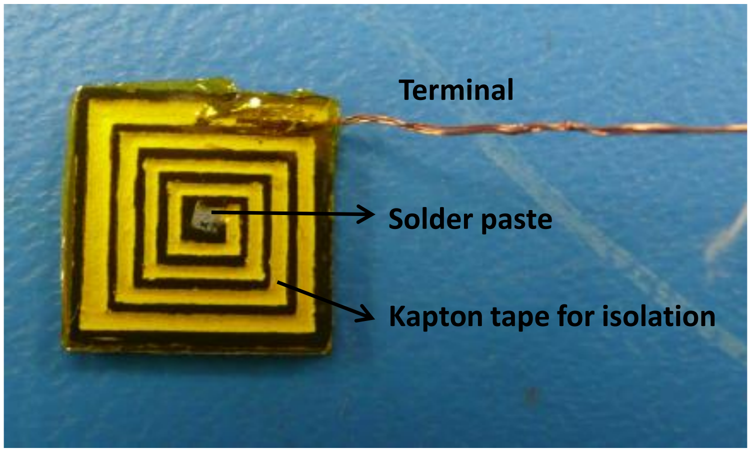

Figure 4.16. Sintered inductor half with silver paste as the winding. A thin layer of Kapton tape was placed on the surface for isolation. Two inductor halves were connected at the center by solder.

The advantage of using silver paste as conductor is that there is no limitation on the shape of the conductor because of the screen printing process. However, the measured resistivity of a silver conductor was more than two times higher than that of a copper conductor, a significant drawback of using silver paste as the conductor. The resistivity measurement is discussed in detail in Appendix C.

4.3 Inductor Prototypes

TABLE XVI RESULTS OF COMBINED METHODS FOR WINDING AND CORE

Core **Winding**	**Laser ablated** LTCC tape	**Routed** Powder iron core
Wrapped Copper round wire #AWG30	▪ L = 2.6 μH (1.9% error against simulation), R = 62 mΩ (8.7% error) ▪ No air gap issue ▪ Winding shape not agreeing with design ▪ Poor dimension control caused by shrinkage	Not tried yet

Core **Winding**	**Laser ablated** LTCC tape	**Routed** Powder iron core
Etched Copper	▪ L = 1.53 μH (30% error against simulation), R = 18 mΩ (22% error) ▪ Poor dimension control caused by shrinkage ▪ Repeatability issue on the winding ▪ Air gap issue	Not tried yet
Routed Copper	▪ L = 1.82 μH (18% error), R = 8.1 mΩ (9% error)	▪ L = 1.42 μH (11% error), R = 8.5 mΩ (21% error)
Printed Silver paste	▪ L = 1.8 μH (18% error), R = 20 mΩ (33% error) ▪ High resistivity results in high R	NA

With different combinations of available fabrication processes for the core and the winding, five prototypes of constant-flux inductor were assembled and the inductance and resistance were measured by an impedance analyzer. Table XVI summarizes all the measurement results for the five inductor prototypes made by different fabrication processes.

4.3.1 Proof of Concept

Among the five inductor prototypes, the one using LTCC ferrite tape and copper wire has the inductance and resistance closest to the simulation results. The inductance has only a 1.9% error and the resistance has an 8.9% error. As Figure 4.17 illustrates, AWG#30 copper wire, which has a diameter of 0.28 mm, was wrapped inside the grooves on the core half. A small amount of silver paste was applied to the center of each inductor half, and the two inductor halves were put on a reflow belt furnace for the solder process. Then the inductor prototype was assembled as shown in Figure 4.17(b). The footprint is 10 mm × 10 mm, the thickness is 2 mm, and the measured inductance is 2.6 μH. A commercial product with comparable inductance would occupy a volume twice as big [23]. Therefore, the prototype with copper wire provides a quick way to verify that the constant-flux design can shrink the total volume while keeping the inductance constant. However, the ideal constant-flux inductor has uneven cross-sectional area of the winding turns in order to keep the resistance in a range comparable with that for a commercial product as well, and the copper wire with a constant width has much higher resistance than the designed structure. The dimensions of the prototype are listed in Table XVII.

.

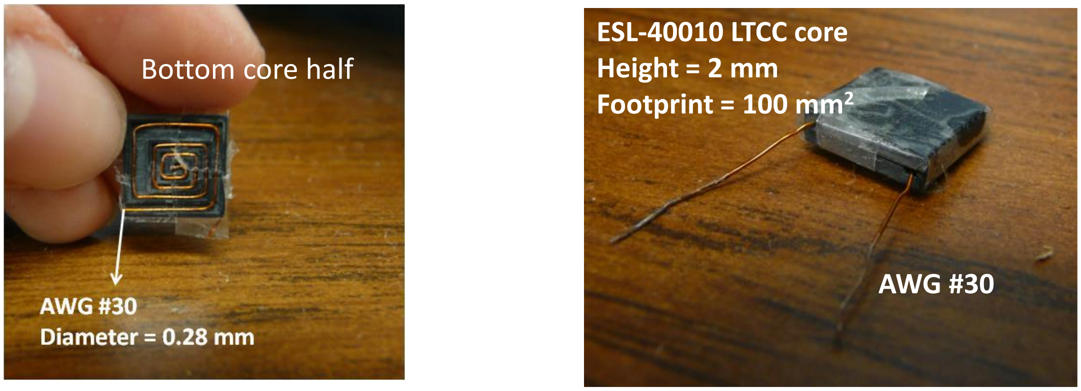

(a)

(b)

Figure 4.17. Fabrication of constant-flux inductor with copper wire as the winding and LTCC ferrite as the core: (a) A bottom core half with AWG#30 copper wire wrapped spirally inside; (b) assembled inductor prototype with two inductor halves connected at the center by solder. The inductance is 2.6 μH (1.9% error against simulation), and the resistance is 62 mΩ (8.9% error against simulation).

TABLE XVII DIMENSIONS OF THE CORE OF LTCC MATERIAL

Winding Turn	**R_{Oj} (mm)**	**R_{Ij} (mm)**
j = 1	4.7	3.7
j = 2	3.4	2.9
j = 3	2.6	1.7
j = 4	1.4	1.0
Thickness of winding (mm)		0.25/0.5
Thickness of an inductor half (mm)		1.0
Footprint of an inductor half (mm)		10 × 10

j is numbered from the outer edge to the center of the core.

Figure 4.18(a) shows the prototype of an inductor half made of LTCC ferrite tape and copper. The LTCC core was sintered after the routing process, and the measured shrinkage in dimensions is around 20%. Based on the measured dimensions after the sintering, the copper sheet was routed by the printed circuit board (PCB) prototyping machine to suitable dimensions that matches that of the core. Two inductor halves were connected in the center by solder. A small amount of solder paste was deposited to the center, and by using the reflow belt furnace, the two inductor halves were assembled as a complete inductor prototype. Figure 4.18(b) shows the complete inductor prototype with LTCC as the core and copper as the winding. The measured inductance is 1.82 μH, and the measured resistance is 8.1 mΩ. Both values match the simulation results within 20%. The dimensions of the prototype are the same as the ones listed in Table XVII except that the winding thickness is 0.5 mm.

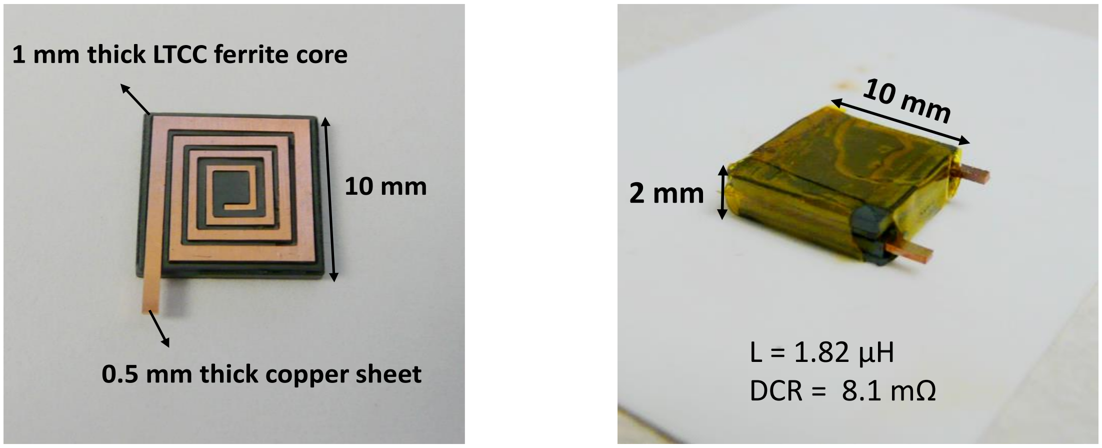

(a) (b)

Figure 4.18. Prototype of (a) an inductor half with LTCC ferrite core and routed copper and (b) assembled constant-flux inductor with inductance of 1.82 µH and resistance of 8.1 mΩ.

4.3.2 Comparison of CFI Prototypes with Commercial Products

The inductor half shown in Figure 4.19(a) was obtained after the winding half was inserted into the corresponding core half. The routed core has a total thickness of 1 mm, and the routed groove is 0.5 mm deep so that the copper winding can be inserted to the core half. Two inductor halves were connected in the center by solder. A small amount of solder paste was deposited to the center of the winding halves. The two inductor halves were placed onto the reflow belt furnace for the solder process.

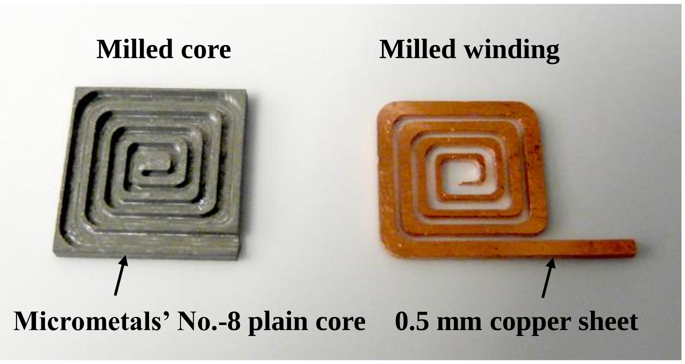

Figure 4.19. Prototypes of routed core (left) and routed copper winding (right).

The prototype of the assembled inductor is shown in Figure 4.20(b). The measured inductance and dc resistance of the fabricated constant-flux inductor are 1.42 μH and 8 mΩ, respectively. Because of the limitation of the fabrication process, an inevitable air gap between the two inductor halves is introduced, since the solder in the center cannot be ideally flat. Therefore, the measured inductance (1.42 μH) is 12% smaller than the simulation result (1.6 μH). The copper winding was trimmed to be slimmer than the simulated structure in order to fit into the core half, and the resistance measured (8 mΩ) is 14% larger than the simulated result. The dimensions of the prototype are listed in Table XVIII.

TABLE XVIII DIMENSIONS OF THE CORE OF POWDER MATERIAL

Winding Turn	**R_{Oj} (mm)**	**R_{Ij} (mm)**
j = 1	4.8	3.7
j = 2	3.5	2.9
j = 3	2.7	1.7
j = 4	1.5	1.0
Thickness of winding (mm)		0.5
Thickness of an inductor half (mm)		1.0
Footprint of an inductor half (mm)		10 × 10

j is numbered from the outer edge to the center of the core.

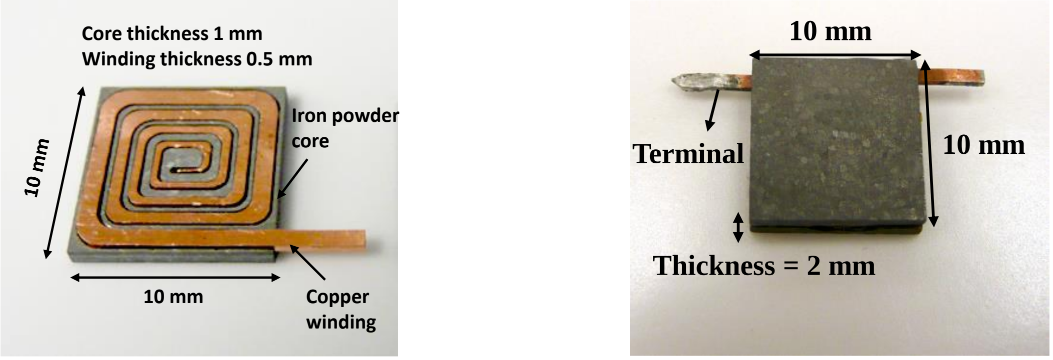

(a) (b)

Figure 4.20. Prototypes of (a) an inductor half with routed iron powder core and routed copper and (b) assembled constant-flux inductor with inductance of 1.42 μH and resistance of 8 mΩ.

A low-profile inductor with inductance and resistance comparable with those of the constant-flux inductor is selected from Signal Transformer as a benchmark [23]. The dimension comparison of the constant-flux inductor prototype with the commercial inductor is shown in Figure 4.21. The commercial inductor has a footprint of 10 mm × 10 mm and a thickness of 4 mm, which is two times larger than that of the constant-flux inductor fabricated with the same inductance and resistance. Therefore, the time-constant-density τ/V of the constant-flux inductor is two times larger than that of the commercial product because of the improved uniformity level of flux density and space utilization.

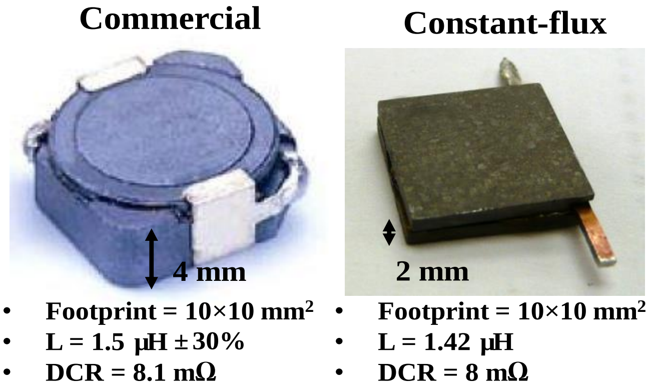

Figure 4.21. Dimension comparison between the commercial product [23] and assembled inductor with comparable electrical ratings but half volume.

Chapter 5 Conclusion and Future Work

5.1 Conclusion

The non-uniformity of magnetic field in conventional structures results in poor space utilization and low energy density in the magnetic material. Making the magnetic flux distribution uniform not only improves the energy density, but also keeps the core from saturation, and leading to a uniform distribution from the thermal standpoint. Therefore, the constant-flux inductor is developed and optimized to fully utilize the magnetic material that is available in the total volume.

The enclosed-winding geometry has the winding structure configured to distribute the magnetic flux into uniform shape. For a given set of input parameters such as the footprint, thickness of the inductor, permeability of the magnetic material, and highest flux density allowed from the core loss limitation, the radii of each winding window can be determined sequentially according to the uniformity factor selected. After the winding structure is determined, the total energy stored in the core volume and the total dc winding loss can be calculated, and yield the inductance and resistance of the inductor. The design procedure is outlined along with a design example that yields a volume of $10 \times 10 \times 2$ mm^3 for L =1.6 μH, I_r = 10 A, and R_{dc} = 7.0 mΩ. A commercial inductor with comparable ratings (L =1.5 μH, I_r = 10 A, and R_{dc} = 8.1 mΩ) would occupy $10.3 \times 10.5 \times 4$ mm^3, two times the volume of the constant-flux inductor.

The time constant, which is defined as the ratio of inductance to resistance, is an important factor to evaluate the performance of an inductor. A higher time constant suggests higher energy, but with minimum loss within a given volume. The objective of the constant-flux inductor is to optimize all the parameters so that the highest time constant can be achieved. Several parameters such as the uniformity factor, the footprint and thickness, the permeability, and the maximum flux density are studied to obtain their relationships with the time constant. For a given volume, an optimized uniformity factor α exists, which has the peak value of the time constant, while different footprints and thicknesses yield different optimal values of α. The time constant increases with increasing volume, since a larger volume provides more space for energy storage. The magnetic properties of the core material is another factor that affects the time constant. At a given volume, the time constant increases proportionally with the permeability, while the maximum flux density has no influence on the time constant at all. The analysis is validated by simulation results, and the maximum error between the model and the simulation is smaller than 10%. The comparisons of the constant-flux inductors (CFI) with the commercial products show that the time constant of the CFI is 2.5 times higher than that of the commercial product at the same volume, or that the volume of the CFI is two times smaller than that of the commercial product at the same value of time constant because of the better utilization of the magnetic material.

Various fabrication procedures for both the core and the winding are proposed to make prototypes of the constant-flux inductor designed. Based on the availability of the prototyping equipment, three methods for the core fabrication and two methods for the winding fabrication are experimented, including routing methods on iron-powder plain core and LTCC material, laser ablation technique on LTCC material, routing method on copper sheet, and screen printing technique with silver paste. The inductor prototype made by the routing method for iron-powder core and 0.5 mm thick copper sheet turns out to give the best result with an inductance of 1.42 μH and a resistance of 8 mΩ. A commercial surface mount inductor with similar electrical ratings (L = 1.5 μH ± 30%, DCR = 8.1 mΩ) would occupy a volume two times as large as the constant-flux inductor prototype.

In conclusion, this thesis describes a method to distribute the magnetic flux uniformly, thus improving the energy density of inductors. A recursive design procedure has been delineated to realize a physical structure meeting specified inductance, dc resistance, and peak magnetic flux density requirements. The analytical model is constructed to study the influence of the input parameters on the time constant of the inductor; therefore, an inductor design can be optimized and evaluated to achieve high performance. The concept was validated by a constant-flux inductor prototype. The results for a 1.4-μH inductor with 10-A current and 8-mΩ dc resistance demonstrates that the constant-flux concept reduced the inductor volume by 50%. This significant improvement saves volume and shrinks the total package volume in most power applications.

5.2 Future work

The constant-flux inductor concept has proved to improve the energy density in inductors with an enclosed-winding geometry. Following this research, there is still some remaining work to be done in the future.

5.2.1 Ac Loss

Only the dc analysis is included in the current study on constant-flux inductor. Ac loss in both the winding and the core is another aspect that needs optimization in the magnetic design. Since the flux distribution is uniform in the constant-flux inductor, the ac flux density is expected to be constant as well. Therefore, it will be useful to study the effect of frequency on the performance of the constant-flux inductor. The core loss of the constant-flux inductor will be measured by using different magnetic materials that have comparable magnetic properties to the commercial products. The constant-flux inductor is expected to be evaluated under commercial applications of power converters such as buck converters and boost converters under different power ratings by comparing the efficiency of the constant-flux inductor with those of the commercial products.

5.2.2 Mass Manufacturing

Another effort that will be focused on is to disseminate the constant-flux structure to inductor manufacturers and to have the constant-flux inductor fabricated by mass production procedures. Nowadays, the fabrication methods employed in the mass production of surface mount inductors include injection molding for the magnetic composite and stamping for the planar winding. The fabrication techniques used in mass manufacturing are more efficient and less costly than the prototyping methods employed in the laboratory, and will make the constant-flux inductor commercial and benefit the industry.

Appendix A. Design of Experiments (DOE) for Laser Ablation Process

Based on the specific structure of the constant-flux inductor introduced herein, the structure of the core can be divided into two parts: a patterned strip and a plate, as shown in Figure A-1. The original laser technique to make low-temperature co-fired ceramic (LTCC) inductors, a flow chart of which is shown in Figure A-2, usually includes 6 steps. The green LTCC ferrite tape from ESL [28] is cut into small pieces and laminated to desired thickness under controlled temperature and pressure. The laminated LTCC stack is then put into the laser machine for laser cutting. After the grooves on the core are patterned, the core strip is removed from the ceramic substrate and laminated to a LTCC stack which serves as the plate substrate. The original process requires lamination after the lasing, so it usually leads to poor pattern alignment, as shown in Figure A-4(b).

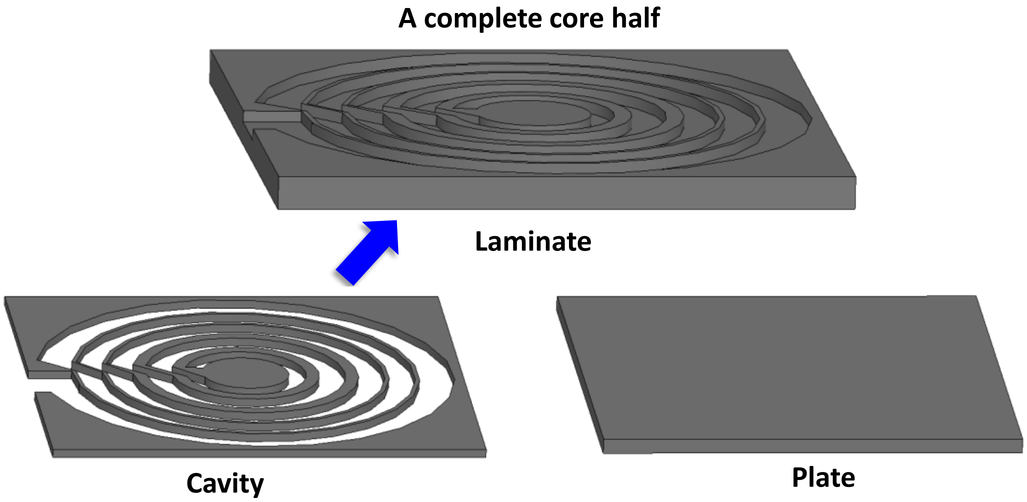

Figure A-1. A complete core half is laminated by a piece with the cavity and a plate as substrate.

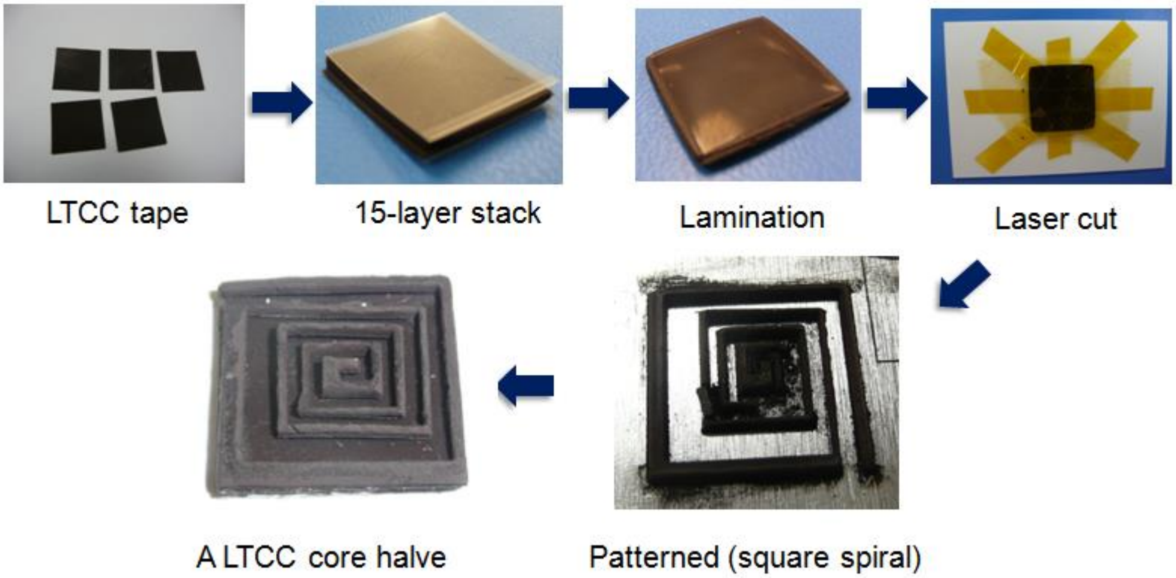

Figure A-2. Fabrication flow chart of original laser technique with lamination of the LTCC ferrite tape, lasing the pattern, and final lamination.

Evolved from the original process, the laser ablation method has the advantage of avoiding further lamination after the lasing; therefore, the pattern on the LTCC stack seems more smooth and neat. Instead of cutting all the way through, the laser beam only rubs out a certain depth of the LTCC stack, as shown in Figure A-3(a). The winding area, or the cavity, can be ablated off by following a user-defined lasing path. Figure A-3(b) shows the lasing path that was used in the laser machine to fabricate a core half. For each segment, the laser beam goes along a spiral path in order to improve the flatness of the ablated surface by distributing the heat evenly.

Figure A-4 compares the core halves made by proposed ablation process and the original lasing process. Since the step of lamination is eliminated in the ablation method, the core half has better shape and alignment.

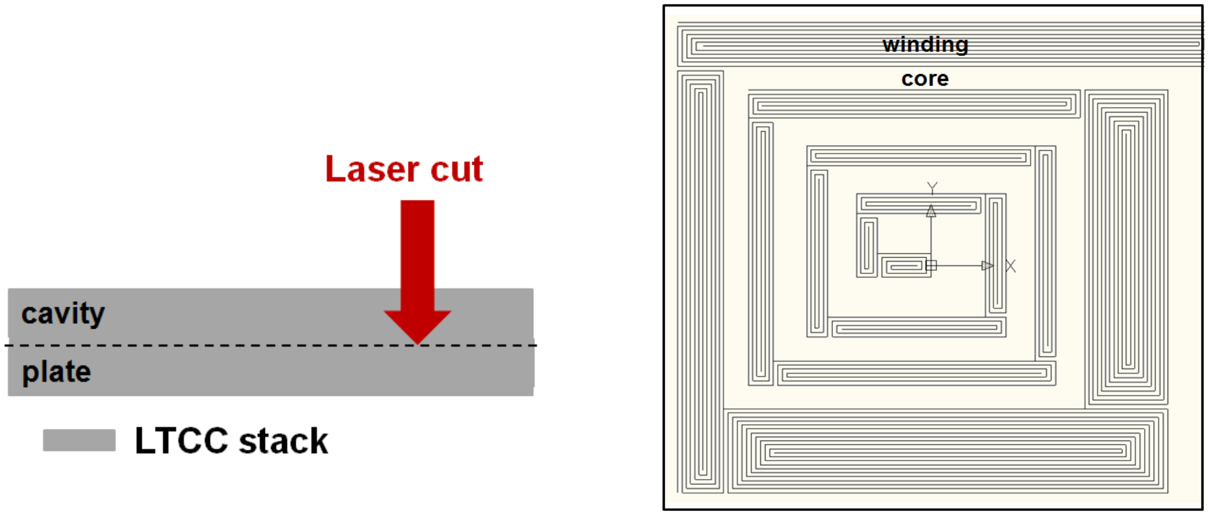

(a) (b)

Figure A-3. Laser ablation method. (a) The laser power is carefully calibrated to give the depth of the cavity and the thickness of the core half through the whole LTCC stack. (b) Spiral path of laser ablation to improve the surface flatness after ablation.

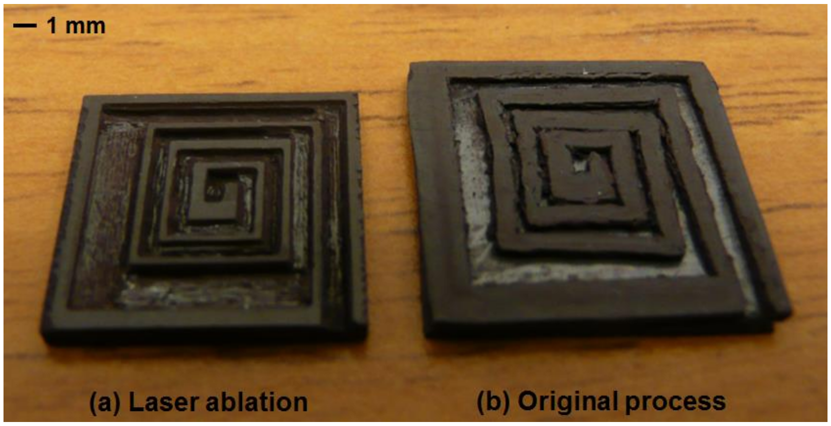

Figure A-4. Comparison of the result obtained by (a) laser ablation and (b) original process. The laser ablation method provides better control on the width of the edges because lamination after lasing is avoided.

One issue that should be strictly controlled in the developed laser ablation method is that the ablation depth is determined by the parameter settings in the laser machine. The lasing velocity and the lasing power affect the ablation result directly. If the parameters of the laser machine are not carefully selected, the lasing path can be very rough and generate a large heat affected area, as Figure A-5(b) shows.

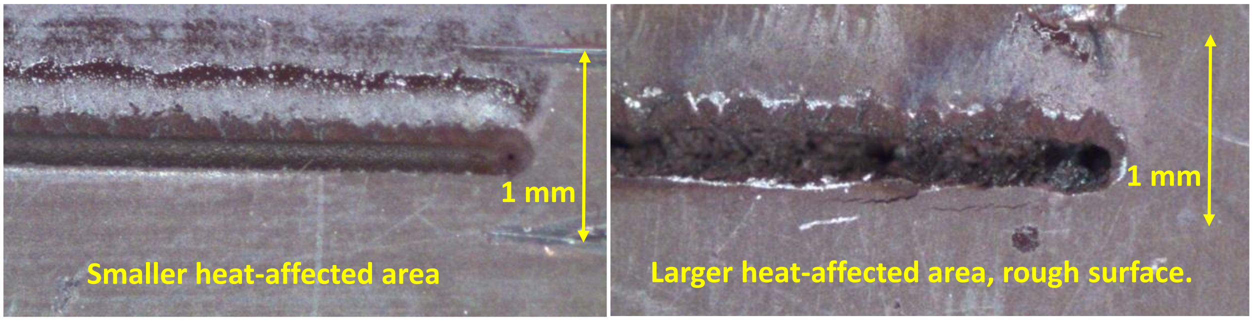

(a) (b)

Figure A-5. Micrographs showing lasing results with different parameter settings in laser machine: (a) a small heat affected area and (b) a larger heat affected area and rough surface.

In order to improve the controllability of the ablation depth, the design of experiments (DOE) method was employed to study the relationship between different laser setting parameters and predict the optimized setting for a given depth.

The response surface method (RSM) is a collection of statistical and mathematical techniques that are useful for developing models and optimizing designs. The performance measured or simulated is called the response. Herein several laser setting parameters, such as the laser power, lasing velocity, and focus distance, are regarded as inputs. A total number of 14 experiments were conducted to provide sufficient data to construct the RSM model. Different experiments use different laser settings to ablate one square segment; therefore, different ablation depths and surface roughness, which are regarded as responses, were obtained from different experiments. All of the data collected were analyzed by using JMP software from SAS. Based on the model built upon the data, the software gives an optimized input set for a target response, which is an ablation depth of 0.5 mm in this case, as shown in Figure A-6.

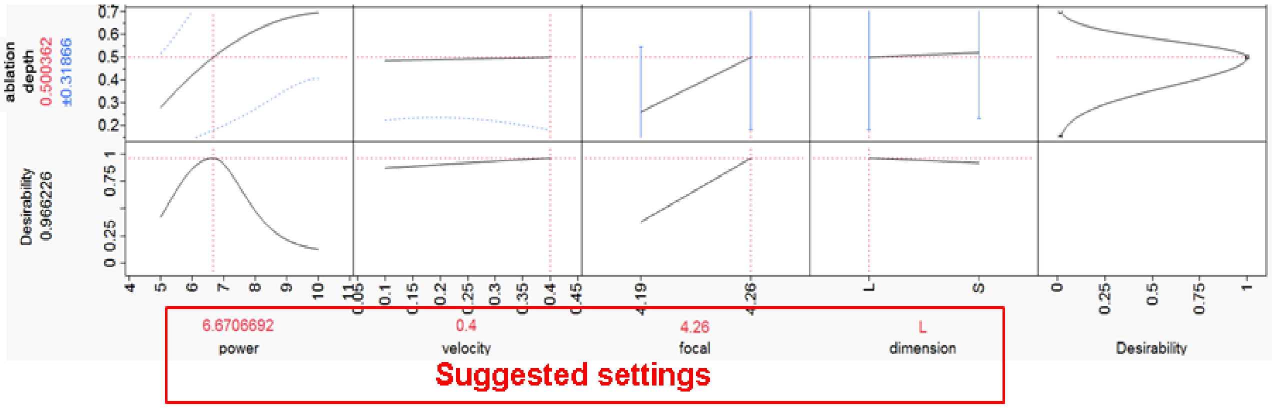

6.6706692 power
0.4 velocity
4.26 focal
L dimension

Figure A-6. Profiler results predicted by statistical analysis software JMP, suggesting an optimized laser setting for each given ablation depth.

Appendix B. Winding Turns Configuration

From equation (2.7), the ampere-turns in each winding window are determined. Therefore, the number of turns that the winding window will be divided into is totally based on the current rating. After the current rating is specified, equation (2.8) gives the number of winding turns in each winding window.

However, from equation (2.8), n_j can be odd, even, or fractional, yielding different ways for distributing the winding turns in each winding window. Therefore, the configuration of the winding turns is not unique, but is based on the fabrication considerations, or the manufacturing limitations.

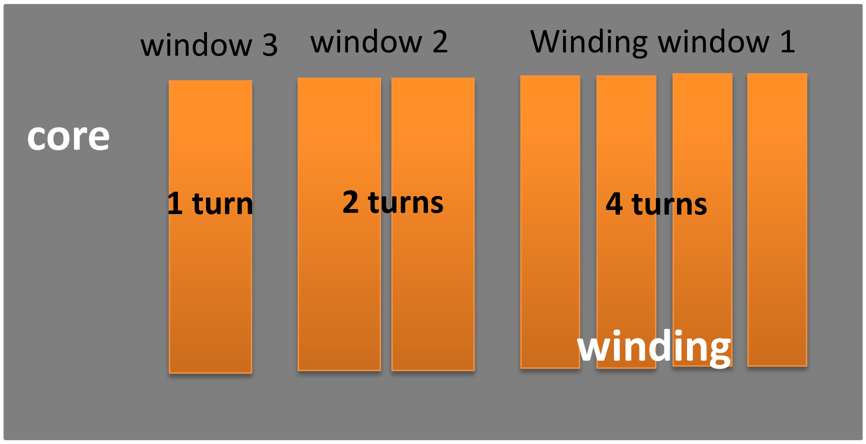

Figure B-1. Axisymmetric view of winding configuration with three winding windows, and seven total turns in one layer.

For instance, Figure B-1 gives a 2D axisymmetric view of a one-layer winding structure with 1, 2, and 3 turns in each winding window. When the number of turns can be approximated to an integer, the easiest way to configure the winding layout is to divide the width of the winding equally and distribute the winding turns all in one layer. In this configuration, the number of winding turns can be kept as close as possible to the designed results whether it is odd or even. However, this configuration always brings difficulty to the fabrication process because of the possibility of some winding turns getting very close to one another. Moreover, when it comes to the 3D structure, the winding has a terminal outside the core, but has to end at the center of the core. This requirement adds extra effort to the manufacture of the inductor.

When the number of turns can be approximated to even numbers for all of the winding windows, the winding configuration turns out to be a two-layer structure, as shown in Figure B-2. The winding starts from the outer edge of the core in one layer, then spirals in and jump to the other layer near the center, and eventually spirals out to the outer edge of the core. Sometimes, the number of turns may not exactly match the design result because of the effort of spreading them over two layers. Therefore, the uniformity level throughout the core may be disturbed somehow. However, unless the approximation is significantly different from the calculated number of turns, the two-layer structure is preferable to the one-layer structure in terms of ease of fabrication.

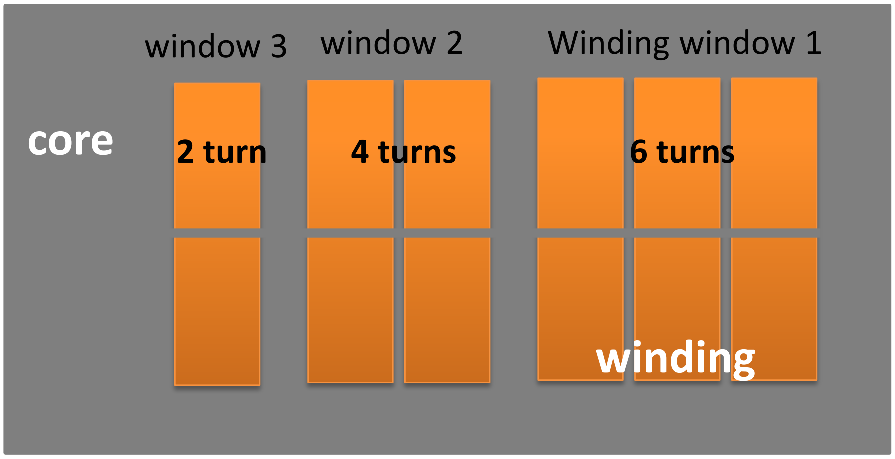

Figure B-2. Axisymmetric view of winding configuration with three winding windows, 12 total turns in two layers.

Another possible condition for the approximation to the number of turns is that the calculated number of turns has a fractional part, such as 0.5 or 3.5, that can hardly be approximated to an integer without significant errors. In this situation, the parallel structure comes into consideration. Figure B-3 gives an example of the parallel structure that has two strands starting from the outermost area and spirals in parallel to the center. For the outermost winding window, 48 ampere-turns lead to 4 turns in terms of a current rating of 12 A. Therefore, a total of 8 strands make up the 4 winding turns. For the second winding window, 18 ampere-turns lead to 1.5 winding turns, so an extra strand connects two regular strands to form the 1.5 turns. Similarly, 12 ampere-turns form one winding turn and 6 ampere-turns yield half a winding turn at the center of the core.

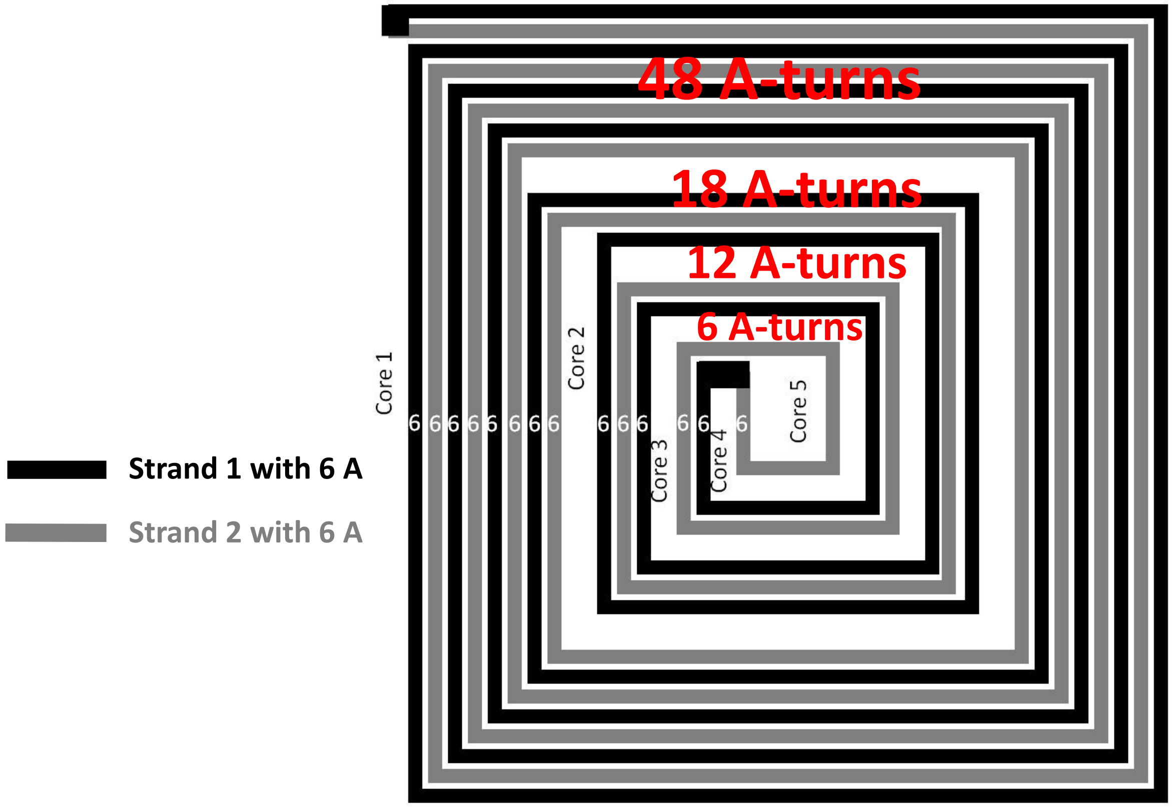

Figure B-3. Top view of the winding configuration with fractional turns illustrating two strands in parallel with each carrying 6 A (one half of 12 A current rating), and 0.5, 1, 1.5, and 4 turns in each winding window from the center to the outermost area of the core.

Appendix C. Resistivity Measurement of Silver Paste

To compare the bulk resistivity of the Dupont 7740 silver paste [43] with that of copper, the following experiment was carried out to measure the bulk resistivity of the silver paste and compare that with the copper.

First of all, a sample with a certain shape was prepared to make the measurement easier and more accurate. As shown in Figure C-1, two samples with the same shape were sintered together according to the sintering profile shown in Figure 4.6(b). One sample uses ceramic tile as the substrate to co-fire with, and the other uses a cirlex fixture as the substrate to co-fire with.

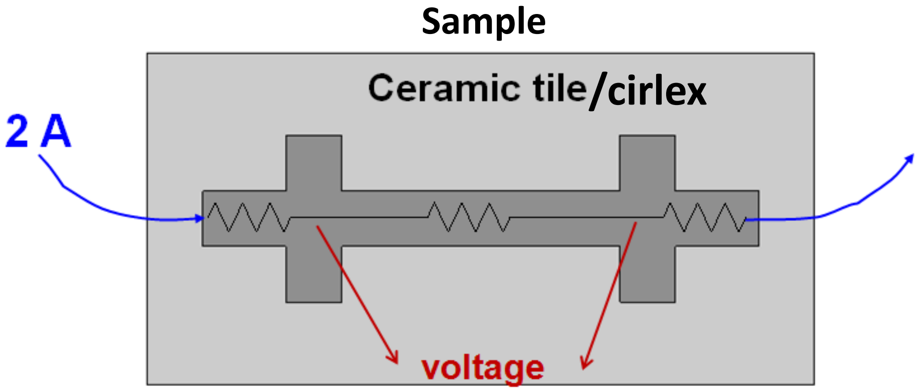

Figure C-1. Drawing of the sample for resistivity measurement.

The objective of preparing two samples is to make sure that the co-firing material does not affect the particle size of the silver paste after sintering, which may affect the bulk resistivity after all. Both the samples were made with four terminals so that four-probe measurements can be performed. In a measurement, a current of 2 A was applied to the outer terminals and the voltage was measured on the two inner terminals. The measurement was repeated with different lengths of the samples that ranges from 3 mm to 9 mm to minimize the measurement error.

Figure C-2 shows the resistivity results for all the samples with different length. The average resistivity was calculated and summarized in the Table below. From the table, it can be seen that the resistivity of silver paste is higher than that of copper, and a higher resistance would be expected of an inductor with a silver paste as the conductor.

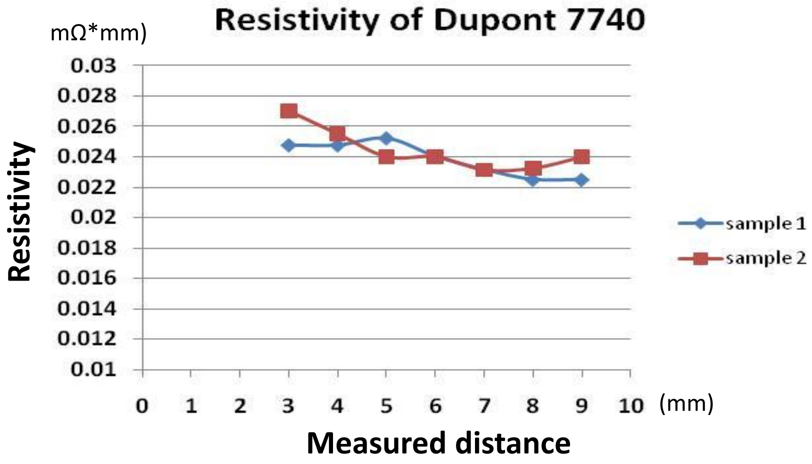

Figure C-2. Resistivity measurement results of the samples with different lengths.

TABLE C-1:
BULK RESISTIVITY COMPARISON BETWEEN SILVER PASTE AND COPPER

Material	Resistivity (mΩ·mm)
DuPont 7740	0.023
Copper	0.017

Appendix D. Matlab Code for Design of Constant-Flux Inductor

```
%----- This file gives the design procedure of a constant-flux inductor and
plots the curve of time constant versus uniformity factor -------%
% alpha: uniformity factor
% miu: permeability
% Tcu: copper thickness
% dz: plate thickness
% Q: time constant (L/R)
clear all
clc
close all
%Given parameters
Bmax=0.35;
miu_0=4*3.1416*10^-7; miu=35*miu_0; rho_cu=17.2*10^-9;pi=3.1416;
I=10;
Rc=5*0.001; Hc=2*0.001; %footprint and height
n=1;
for alpha=0.5:0.02:0.8;
  %----step 1: calculate the radii of outermost turn-----%
syms dz dRo1 dRi1
Tcu=Hc-2*dz; Ro1=Rc-dRo1; Ri1=alpha*Ro1; Ro2=Ri1-dRi1;Hmax=Bmax/miu;
%Ampere's Law
Ni_in=Hmax*Tcu+2*Hmax*Ri1*log(Ro1/Ri1)+alpha*Hmax*Tcu;
Ni_out=alpha*Hmax*Tcu+alpha*Hmax*(1+alpha)*(dz+dRi1)+2*alpha*Hmax*Ri1*log(Ro1
/Ri1)+alpha^2*(1+alpha)*Hmax*(dRo1+dz)+alpha^2*Hmax*Tcu;
Eqn1=Ni_in-Ni_out;
%Gauss' Law
Eqn2=2*pi*(Ri1-dRi1)*dz*alpha*(1+alpha)/2+pi*(Ri1^2-Ro2^2)*(1+alpha)/2-
2*pi*Ri1*dz*(1+alpha)/2;
Eqn3=2*pi*Ro1*dz*alpha*(1+alpha)/2-pi*(Rc^2-Ro1^2)*alpha*(1+alpha)/2;
S = solve(Eqn1==0,Eqn2==0,Eqn3==0);
for i=1:length(S.dz)
    if (0<S.dz(i))&&(S.dz(i)<Hc)&&(0<S.dRi1(i))&&(0<S.dRo1(i))
        dz=S.dz(i);
        dRo1=S.dRo1(i);
        dRi1=S.dRi1(i);
    end
end
%----step 2: calculate the radii of the rest turn-----%
syms dRi2
Ro1=Rc-dRo1; Ri1=alpha*Ro1; Ro2=Ri1-dRi1;Ri2=alpha*Ro2;Ro3=Ri2-dRi2;
Eqn2_1=2*pi*Ro3*dz*alpha*(1+alpha)/2+pi*(Ri2^2-Ro3^2)*(1+alpha)/2-
2*pi*Ri2*dz*(1+alpha)/2;
S2 = solve(Eqn2_1==0);
for i=1:length(S2)
    if (0<S2(i))&&(S2(i)<0.001)
      dRi2=S2(i);
   % break
    end
end
```

```
syms dRi3
Ro3=Ri2-dRi2;Ri3=alpha*Ro3;Ro4=Ri3-dRi3;Tcu=Hc-2*dz;
Eqn3_1=2*pi*Ro4*dz*alpha*(1+alpha)/2+pi*(Ri3^2-Ro4^2)*(1+alpha)/2-
2*pi*Ri3*dz*(1+alpha)/2;
S3 = solve(Eqn3_1==0);
for i=1:length(S3)
    if (0<S3(i))&&(S3(i)<0.001)
      dRi3=S3(i);
    end
end
%----step 3: calculate the Ampere-turns of the CFI inductor-----%
AT1=Hmax*Tcu+2*Hmax*Ri1*log(Ro1/Ri1)+alpha*Hmax*Tcu;
AT2=Hmax*Tcu+2*Hmax*Ri2*log(Ro2/Ri2)-alpha*Hmax*Tcu;
AT3=Hmax*Tcu+2*Hmax*Ri3*log(Ro3/Ri3)-alpha*Hmax*Tcu;
%----step 4: calculate the Q value of the CFI inductor-----%
Hp=dz; Hw=Hc-2*Hp;
Pohmloss=rho_cu*2*pi/Hw*(AT1^2+AT2^2+AT3^2)/log(1/alpha);
Havg2=Hmax;Havg1=(1+alpha)^2/4*Hmax;%average flux density
syms r
Eng_itg=2*Hmax^2*(1+alpha)/2*Hp*miu/2*(int(2*pi*r*(Ri1/r)^2,Ri1,Ro1)+int(2*pi
*r*(Ri2/r)^2,Ri2,Ro2)+int(2*pi*r*(Ri3/r)^2,Ri3,Ro3));
Eng_avg1=miu*Havg1^2/2*pi*Hp*(2*(Ri1^2-Ro2^2)+2*(Ri2^2-Ro3^2)+(Rc^2-
Ro1^2)*Hw/Hp);
Eng_avg2=miu*Havg2^2/2*pi*Hw*((Ri1^2-Ro2^2)+(Ri2^2-Ro3^2)+Ri3^2);
Eng=Eng_itg+Eng_avg1+Eng_avg2;
Q=2*Eng/Pohmloss;
Q_matrix(n)=Q;
n=n+1;
end

 figure
 plot(alpha_p,Q_matrix*10^6,'-
ko','LineWidth',2,'MarkerFaceColor','k','MarkerSize',4)
 % Create labels
 xlabel({'Uniformity factor
\alpha'},'FontWeight','bold','FontSize',14,'FontName','Times New Roman');
 ylabel({'Time constant
(\mus)'},'FontWeight','bold','FontSize',14,'FontName','Times New Roman');
```

References

[1] D. M. Robert W Erickson, *Fundamentals of power electronics*, 2nd.: Springer, 2001, 495-585.

[2] Q. Li, D. Yan, and F. C. Lee, "High density low profile coupled inductor design for integrated Point-of-Load converter," in *Proc. IEEE Applied Power Electron. Conf. Expo*, 2010, pp. 79-85.

[3] E. C. Snelling, *Soft ferrites: properties and applications*, 2nd ed.: Butterworths, 1988, 136-157.

[4] K. D. T. Ngo, R. P. Alley, A. J. Yerman, R. J. Charles, and M. H. Kuo, "Design issues for the transformer in a low-voltage power supply with high efficiency and high power density," *IEEE Trans. Power Electron.*, vol. 7, pp. 592-600, 1992.

[5] K. D. T. Ngo, E. Alpizar, and J. K. Watson, "Modeling of losses in a sandwiched-winding matrix transformer," *IEEE Trans. Power Electron.*, vol. 10, pp. 427-434, 1995.

[6] E. Osegueda, K. D. T. Ngo, W. M. Polivka, and M. M. Walters, "Perforated-plate magnetics. Part I: Mode-1 inductor/transformer," *IEEE Trans. Aerosp. Electron. Syst.*, vol. 31, no. 3, pp. 968-976, 1995.

[7] E. Herbet, “Flat matrix transformers”, US Patent 4,665,357, 12 May 1987.

[8] S. Kirli, K. D. T. Ngo, W. M. Polivka, and M. M. Walters, "Inductance modeling for a mode-2 perforated-plate matrix inductor/transformer," in *Proc. IEEE Power Electronics Specialists Conf.*, 1993, pp. 1130-1136.

[9] R. S. Lai, K. D. T. Ngo, and J. K. Watson, "Steady-state analysis of the symmetrical push-pull power converter employing a matrix transformer," *IEEE Trans. Power Electron.*, vol. 7, pp. 44-53, 1992.

[10] Q. Li and F. C. Lee, "High inductance density low-profile inductor structure for integrated point-of-load converter," in *Proc. IEEE Applied Power Electron. Conf. Expo*, 2009, pp. 1011-1017.

[11] G. Skutt and F. C. Lee, "Visualization of magnetic flux density in ferrite core structures," in *Computers in Power Electronics, 1994, IEEE 4th Workshop on*, pp. 307-312.

[12] Ultra high current inductor MMD-12DZ-2R2M-V1 datasheet. (2007) [online]. Available: http://www.maglayersusa.com/

[13] SUSUMU International U.S.A. [online] Available: http://www.susumu-usa.com/products/pcc.htm

[14] L. Wang, Y. Pei, Y. Xu, Z. Wang, and Y. Liu, "A horizontal-winding multi-permeability distributed air-gap inductor," in *Proc. IEEE Applied Power Electron. Conf. Expo*, 2012, pp. 994-1001.

[15] O. Ziwei, O. C. Thomsen, M. A. E. Andersen, and T. Bjorklund, "Low profile, low cost, new geometry integrated inductors," in *Proc. IEEE Applied Power Electron. Conf. Expo*, 2011, pp. 150-156.

[16] J. K. Seshadri, D. Xu, and K. D. T. Ngo, "Inductor structure with improved space utilisation," *Electronics Letters*, vol. 48, pp. 164-165, 2012.

[17] R. Hahn, S. Krumbholz, and H. Reichl, "Low profile power inductors based on ferromagnetic LTCC technology," in *Proc. IEEE Electron. Compon. and Technol. Conf.*, 2006, pp. 528-533.

[18] J. K. Seshadri, "Uniform field distribution using distributed magnetic structure," M.S. Theis, Virginia Tech 2011.

[19] Ultra high current inductor MMD-12CE-1R5M-V1 datasheet. (2007) [online]. Available: http://www.maglayersusa.com/

[20] L. H. Dixon, "Magnetics design for switching power supplies: section 1 introduction and basic magnetics," Texas Instruments, 2001.

[21] L. H. Dixon, "Magnetics design for switching power supplies: section 2 magnetic core characteristics," Texas Instruments, 2001.

[22] G. G. Orenchak, "Specify saturation properties of ferrites cores to prevent field failure," TSC Ferrite International [online]. Available: http://www.tscinternational.com

[23] High current shielded SMD power inductor SCRH104R datasheet. [online] Available: http://www.signaltransformer.com/sites/all/pdf/smd/ P150_SCRH104R.pdf

[24] Low profile, high current inductors IFSC-1008AB-01 from Vishay. [online] Available: http://www.vishay.com/docs/34294/s108ab01.pdf

[25] Bourns Inc. [online] Available: http://www.bourns.com/

[26] SMD inductors for power line MLP2520S1R0M from TDK corporation. [online] Available: http://www.tdk.com/inductors.php

[27] Micrometals. Available: http://www. micrometals.com/

[28] Datasheets of 40010 LTCC tapes of Electroscience Labs. [online] Available: http://www.electroscience.com

[29] TDK Corporation of America. [online] Available: http://www.tdk.com/inductors.php

[30] Hitachi Metals America, Ltd. [online] Available: http://www.hitachimetals.com/

[31] Pulse Electronics. [online] Available: http://www.pulseelectronics.com

[32] The Electic Materials Co. [online] Available: http://www.elecmat.com

[33] M. H. F. Lim, "Low temperature co-fired ceramics technology for power magnetics integration," Ph.D. Dissertation, Virginia Tech 2008.

[34] Q. Li, "Low profile magnetic integration for high frequency point-of-load converter," Ph.D. Dissertation, Virginia Tech 2011.

[35] M. F. Shafique and I.D. Robertson, "Laser prototyping of multilayer LTCC microwave components for system-in-package applications," Microwaves, Antennas & Propagation, IET, vol. 5, no. 8, pp. 864,869, June 6, 2011.

[36] J. Kita, E. Gollner, and R. Moos, "Laser processing of materials for MCM-C applications," Electronics System-Integration Technology Conference, 2008, pp. 149-154.

[37] M. H. A. H. Feingold, R. L. Wahlers, and M. A. Stein, "Materials for capacitive and inductive components integrated with commercially available LTCC systems," presented at the IMAPS 2003.

[38] M. H. Lim, J. Dong, J. D. van Wyk, T. C. Lee, and K. D. T. Ngo, "Shielded LTCC inductor as substrate for power converter," *Proc. IEEE Power Electronics Specialists Conf.*, 2007, pp. 1605-1611.

[39] L. Wang, Y. Pei, Y. Xu, Z. Wang, and Y. Liu, "Evaluation of LTCC capacitors and inductors in DC/DC converters," in *Proc. IEEE Applied Power Electron. Conf. Expo*, 2010, pp. 2060-2065.

[40] G. S. J. Bielawski, A. H. Feingold, C. Y. D. Huang, M. R. Heinz, R. L. wahlers, "Low profile transformers using low temperature co-fire magnetic tape," presented at IMAPS 2003.

[41] M. S. Rylko, K. J. Hartnett, J. G. Hayes, and M. G. Egan, "Magnetic material selection for high power high frequency inductors in DC-DC converters," in *Proc. IEEE Applied Power Electron. Conf. Expo*, 2009, pp. 2043-2049.

[42] Y. Han, G. Cheung, L. An, C. R. Sullivan, and D. J. Perreault, "Evaluation o f magnetic materials for very high frequency power applications," *Proc. IEEE Power Electronics Specialists Conf.*, 2008, pp. 4270-4276.

[43] DuPont 7740 datasheet. Available: http://www2.dupont.com

[44] J. A. Ferreira, "Improved analytical modeling of conductive losses in magnetic components," *IEEE Trans. Power Electron.*, vol. 9, pp. 127-131, 1994.

[45] K. D. T. Ngo, R. P. Alley, A. J. Yerman, "Fabrication method for a winding assembly with a large number of planar layers," in *Proc. IEEE Applied Power Electron. Conf. Expo*, 1991, pp. 543-549.

[46] M. P. Perry, "Multiple layer series connected winding design for minimum losses," IEEE Tran. Power App. Syst., vol. PAS-98, pp. 116-123, Jan./Feb. 1979.

[47] L. Ye, G. R. Skutt, R. Wolf, and F. C. Lee, "Improved winding design for planar inductors," in *Proc. 28th Annu. IEEE Power Electron. Spec. Conf.*, vol. 2, 1997, pp. 1561-1567.

[48] R. Prieto, J. A. Cobos, O. Garcia, P. Alou, and J. Uceda, "Model of integrated magnetics by means of ‘double 2D’ finite element analysis techniques," in *Proc. 30th Annu. IEEE Power Electron. Spec. Conf.*, vol. 1, 1999, pp. 598-603.

[49] User’s guide—Maxwell 3D: Ansoft Corporation.